

# CANADIAN JOURNAL OF RESEARCH

VOLUME 28

NOVEMBER, 1950

NUMBER 6

## — SECTION A —

## PHYSICAL SCIENCES

### *Contents*

	Page
Ionospheric Reflection of Very Long Radio Waves— <i>J. P. Stanley</i>	549
An Atomic Beam Source and Spectrograph for Hyperfine Structure. Nuclear Moments of Silver— <i>M. F. Crawford, A. L. Schawlow, F. M. Kelly, and W. M. Gray</i> - - - - -	558
Applications of Diffusion Theory to Evaporation from Droplets and Flat Surfaces— <i>G. Luchak and G. O. Langstroth</i> - -	574
The Evaporation of Droplets in Still Air— <i>G. O. Langstroth, C. H. H. Diehl, and E. J. Winhold</i> - - - - -	580
The Thermal Conductivity of Elastomers under Stretch and at Low Temperatures— <i>T. M. Dauphinee, D. G. Ivey, and H. D. Smith</i> - - - - -	596
Emission of $\text{Li}^3_2$ Nuclei in Cosmic Ray Stars— <i>E. Pickup and L. Voyvodic</i> - - - - -	616
Etudes sur les Rayons Cosmiques à l'Aide d'Emulsions Photographiques Spéciales— <i>Pierre Demers</i> - - - - -	628

NATIONAL RESEARCH COUNCIL  
OTTAWA, CANADA

## CANADIAN JOURNAL OF RESEARCH

The *Canadian Journal of Research* is issued in six sections, as follows:

- |                       |                        |
|-----------------------|------------------------|
| A. Physical Sciences  | D. Zoological Sciences |
| B. Chemical Sciences  | E. Medical Sciences    |
| C. Botanical Sciences | F. Technology          |

For the present, Sections A, C, D, and E are to be issued six times annually, and Sections B and F, twelve times annually, each under separate cover, with separate pagination.

The *Canadian Journal of Research* is published by the National Research Council of Canada under authority of the Chairman of the Committee of the Privy Council on Scientific and Industrial Research. The *Canadian Journal of Research* is edited by a joint Editorial Board consisting of members of the National Research Council of Canada, the Royal Society of Canada, and the Chemical Institute of Canada.

Sections B and F of the *Canadian Journal of Research* have been chosen by the Chemical Institute of Canada as its medium of publication for scientific papers.

### EDITORIAL BOARD

*Representing*  
NATIONAL RESEARCH COUNCIL

DR. H. P. ARMES (*Chairman*),  
Dean of the University,  
University of Manitoba,  
Winnipeg, Man.

DR. OTTO MAASS,  
Macdonald Professor of Physical  
Chemistry,  
McGill University,  
Montreal, P.Q.

DR. J. H. L. JOHNSTONE,  
Professor of Physics,  
Dalhousie University,  
Halifax, N.S.

DR. A. BERTRAND,  
Professor of Bacteriology,  
Faculty of Medicine,  
University of Montreal,  
Montreal, P.Q.

*Ex officio*

DR. LÉO MARION, Editor-in-Chief,  
Division of Chemistry,  
National Research Laboratories,  
Ottawa.

DR. H. H. SAUNDERSON,  
Director, Division of  
Information Services,  
National Research Council,  
Ottawa.

*Representing*

ROYAL SOCIETY OF CANADA

DR. G. M. VOLKOFF,  
Professor of Physics,  
University of British Columbia,  
Vancouver, B.C.

DR. J. W. T. SPINKS,  
Dean, College of Graduate Studies,  
University of Saskatchewan,  
Saskatoon.

DR. H. S. JACKSON,  
Head, Department of Botany,  
University of Toronto,  
Toronto.

DR. E. HORNE CRAIGIE,  
Department of Zoology,  
University of Toronto,  
Toronto.

} Section  
III

} Section  
V

*Representing*

THE CHEMICAL INSTITUTE OF CANADA

DR. H. G. THODE,  
Department of Chemistry,  
McMaster University,  
Hamilton.

### EDITORIAL COMMITTEE

Editor-in-Chief, DR. LÉO MARION  
Editor, Section A, DR. G. M. VOLKOFF  
Editor, Section B, DR. J. W. T. SPINKS  
Editor, Section C, DR. H. G. THODE  
DR. H. S. JACKSON

Editor, Section D, DR. E. HORNE CRAIGIE  
Editor, Section E, DR. J. B. COLLIP  
Editor, Section F, DR. J. A. ANDERSON  
DR. G. M. VOLKOFF  
DR. H. G. THODE

Manuscripts should be addressed:

*Editor-in-Chief,  
Canadian Journal of Research,  
National Research Council, Ottawa, Canada.*







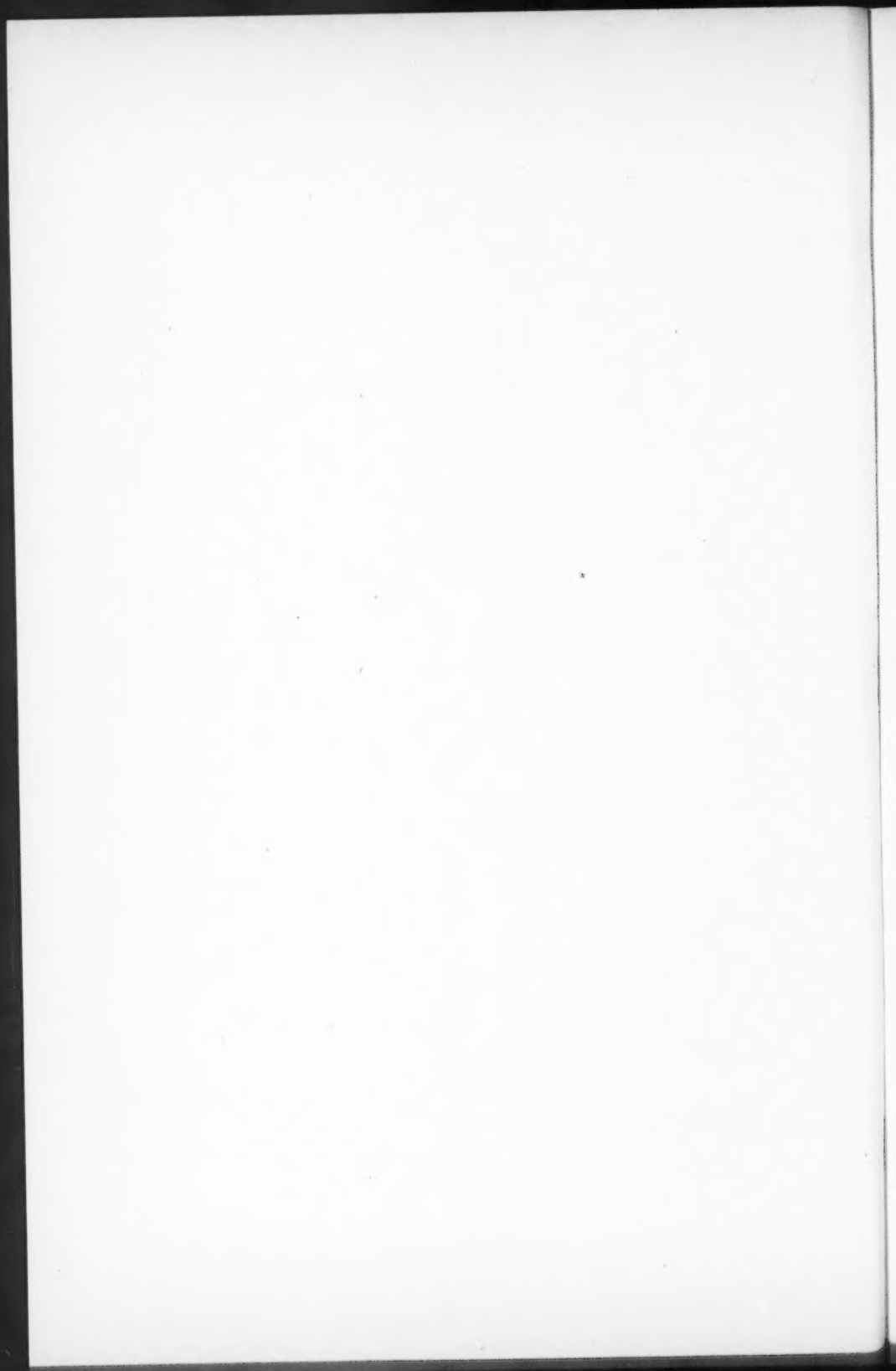
### NOTICE

The Canadian Journal of Research is at present published in six sections, A to F. Starting with January 1, 1951, these sections will be published as separate journals under distinctive names and the designation Canadian Journal of Research will no longer be used. The present names and the corresponding new names are as follows:

<i>Present Name</i>	<i>New Name</i>
Canadian Journal of Research, Section A (Physical Sciences)	Canadian Journal of Physics
Canadian Journal of Research, Section B (Chemical Sciences)	Canadian Journal of Chemistry
Canadian Journal of Research, Section C (Botanical Sciences)	Canadian Journal of Botany
Canadian Journal of Research, Section D (Zoological Sciences)	Canadian Journal of Zoology
Canadian Journal of Research, Section E (Medical Sciences)	Canadian Journal of Medical Sciences
Canadian Journal of Research, Section F (Technological Sciences)	Canadian Journal of Technology

In order to preserve continuity the present sequence of volume numbers will be retained, and in each case the volume for 1951 will be Volume 29.

The subscription rates for the Journals will remain as at present.



# Canadian Journal of Research

Issued by THE NATIONAL RESEARCH COUNCIL OF CANADA

VOL. 28, SEC. A.

NOVEMBER, 1950

NUMBER 6

## IONOSPHERIC REFLECTION OF VERY LONG RADIO WAVES<sup>1</sup>

By J. P. STANLEY

### Abstract

A simplified model of the long-wave-reflecting region of the ionosphere, first considered in a previous paper,<sup>\*</sup> is used to calculate the theoretical variation of sky wave reflection coefficient with angle of incidence and with the angle of dip of the earth's magnetic field. The resulting curves are found to be in good agreement with experiment. They lead to the conclusion that theoretical results based on the assumption of a vertical magnetic field will not lead to errors in vertical incidence sky wave reflection coefficient greater than about 10%, even though the field is inclined at an angle of as much as 23° to the vertical.

### 1. Introduction

An electron density of only 350 electrons per cc. is sufficient to reflect radio waves of wave length greater than 10 km. A study of the propagation phenomena of these 'very long waves' thus provides a method of probing the very bottom of the ionosphere, where the electron density is of this order. In a recent paper (3), certain experimental results obtained by the Cavendish Radio Group at Cambridge (2) were examined with this end in view. These results showed that there is a very sharp decrease in the sky wave reflection coefficient in the neighborhood of 30 kc. per sec. From these results, it was found possible to estimate the mean value of the electronic collision frequency at these levels. Another important factor is the distribution of electron density with height. Three models of the electron density distribution at the bottom of the ionosphere were considered. Two of these, in which the electron density gradient was assumed to be linear and parabolic, were ruled out by the experimental results. The third, assuming a density gradient increasing exponentially with height, was found to be feasible.

In Paper 1, we examined the reason for the failure of the parabolic model of the ionosphere to explain the observed variation of sky wave amplitude with frequency in the case of very long waves. At first sight, it seemed that there was very little real difference between the two models, parabolic and exponential.

The reason for the sharp frequency cutoff produced by an exponential layer and required by experiment appeared to lie in the existence of the long 'tail' of ionization at its lower levels. Now, if the parabolic layer were modified by

<sup>1</sup> Manuscript received May 12, 1950.

Contribution from Computation Centre, McLennan Laboratory, University of Toronto, Toronto, Ont.

\* Hereafter referred to as Paper I.

the addition of a long slab of relatively low electron density below it, then the desired cutoff would be produced. This idea led us to the simplified model of Fig. 1, which in effect considers the ionosphere to act as a 'tarnished mirror' relative to very low frequencies. If the values of the parameters involved are suitably chosen, this model reproduces quite well the sharp decrease of reflection coefficient in the neighborhood of 30 kc. per sec. observed by Straker, Bracewell and Harwood (4). It also gives a downcoming wave which for small angles of incidence is approximately circularly polarized, again agreeing with observation.

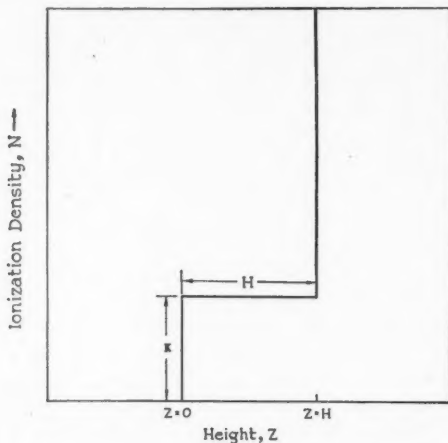


FIG. 1

In the case of the parabolic or exponential layers, the amplitude of the reflected wave decreases steadily as the frequency is increased, if a realistic variation of collision frequency with height is assumed. However, it is known from experiment that this amplitude passes through a minimum somewhere between 20 kc. per sec. and 1 Mc. per sec. Now the tarnished mirror produces just such a phenomenon. It may, in spite of its apparent crudity, be preferable to the exponential model.

It is the purpose of this paper to examine more closely the tarnished mirror model of the long-wave reflecting region of the ionosphere. This model has the considerable advantage that it enables an exact solution of the equations of propagation to be obtained, even in the most general case of oblique-incidence propagation in an oblique magnetic field. We shall consider two particular cases.

(1) Vertical magnetic field; oblique incidence. For this model, no approximations regarding the transition region (6) or the relative values of the parameters involved are necessary. The solution is exact, and on this account will

be of interest. We shall show that the reflecting properties of the model vary with angle of incidence in a manner consistent with observation.

(2) Vertical incidence; magnetic field oblique. This is a case which could not be dealt with previously. We have hitherto assumed that the earth's magnetic field is directed vertically. The effect of varying the obliquity of this field should be of considerable interest. We shall use the model to predict the effect of a magnetic field inclined (as it is at Cambridge) at an angle of  $23^\circ$  to the vertical.

## 2. Solution of the Equations of Propagation

Following the notation of Wilkes (6), let

$c$  = velocity of electromagnetic waves *in vacuo*,

$m$  = mass of an electron,

$e$  = charge of an electron (e.s.u.),

$N$  = electron density,

$\vec{H}_e$  = the earth's magnetic field in gauss,

$P = 2\pi \times$  frequency of waves,

$k = P/c$ ,

$\nu$  = the frequency of electronic collisions,

$X = 4\pi Ne^2/mp^2$ , proportional to the ionization density,

$\vec{Y} = e\vec{H}_e/mcP$ , proportional to the earth's magnetic field,

$Z = \nu/P$ , proportional to the electronic collision frequency,

$Y = |\vec{Y}|$ ,

$\vec{E}$  = electric vector of the wave,

$\vec{H}$  = magnetic vector of the wave.

The equations of propagation given by Wilkes [ref. (6), Equations (2.3, 2.4, 2.5)] may be written in the form

$$(2.1) \quad \vec{E} [(1 - K^2\sigma)^2 - K^2\sigma^2 Y^2] = -\sigma[\vec{E} \cdot \vec{Y}]\vec{Y} + \vec{G}(1 - K^2\sigma) + iK\sigma(\vec{G} \times \vec{Y}),$$

$$K = 1 - iZ$$

$$\sigma = \frac{X}{K(K^2 - Y^2)}$$

$$-k^2 G_x = \frac{d^2 E_x}{dz^2} - ik \sin \theta \frac{dE_z}{dz}$$

$$-k^2 G_y = \frac{d^2 E_y}{dz^2} - k^2 \sin^2 \theta E_y$$

$$-k^2 G_z = -ik \sin \theta \frac{dE_x}{dz} - k^2 \sin^2 \theta E_z.$$

Here it is assumed that we have a plane wave incident at an angle  $\theta$  on a stratified medium. The  $z$ -axis is taken vertically, the  $x$ -axis in the plane of propagation.

Let us now put

$$\begin{aligned}(1 - K^2\sigma) &= k^2 V \\ iK\sigma &= k^2 \rho \\ (1 - K^2\sigma)^2 - K^2\sigma^2 Y^2 &= W = k^4[\rho^2 Y^2 + V^2].\end{aligned}$$

*Case 1.* Vertical magnetic field, oblique incidence.

Putting

$$Y_x = Y_y = 0, Y_z = Y, \text{ we have}$$

$$\begin{aligned}(2.2) \quad E_x[W + VD^2] + E_y[\rho YD^2 - k^2 \rho \sin^2 \theta Y] + E_z[-ikV \sin \theta D] &= 0, \\ E_x[-\rho YD^2] + E_y[W + VD^2 - Vk^2 \sin^2 \theta] + E_z[\rho ik \sin \theta YD] &= 0, \\ E_x[-ikV \sin \theta D] + E_z[W + \sigma Y^2 - Vk^2 \sin^2 \theta] &= 0,\end{aligned}$$

where  $D$  denotes the operator  $\frac{d}{dz}$ .

This set of simultaneous linear differential equations has constant coefficients in the case of the tarnished mirror model. It can readily be solved using the method given by Frazer, Duncan, and Collar, "Elementary Matrices", Chapter V (2).

Let us put  $D = k\Delta$ . Then the determinantal equation is

$$\begin{aligned}(2.3) \quad \Delta^4(W + \sigma Y^2) + \Delta^2[(W + \sigma Y^2)(2k^2 V - \sin^2 \theta) - k^4 V^2 \sin^2 \theta] \\ + [W + \sigma Y^2 - Vk^2 \sin^2 \theta][W - k^2 V \sin^2 \theta] = 0.\end{aligned}$$

The fundamental solutions of (2.2) are

$$\vec{E} = \vec{B} \exp \{k\Delta z\},$$

where  $\Delta$  is a root of (2.3) and where

$$\vec{B} = \begin{bmatrix} ik^4 \sin \theta \Delta [\Delta^2 - \sin^2 \theta + k^2 V], \\ -ik^2 \sin \theta \Delta \rho Y, \\ k^4 [W + \Delta^4 + 2k^2 V \Delta^2 - \Delta^2 \sin^2 \theta - k^2 V \sin^2 \theta] \end{bmatrix}.$$

Now we are not interested in  $E_z$ . Thus we may for convenience consider the fundamental solutions:

$$\begin{aligned}(2.4) \quad E_x &= (\Delta^2 - \sin^2 \theta + k^2 V) \exp \{k\Delta z\}, \\ E_y &= -k^2 \rho Y \exp \{k\Delta z\}.\end{aligned}$$

Suppose the roots of the determinantal equation (2.3) are  $\pm\Delta_1, \pm\Delta_2$ . Then let us consider the solution

$$\begin{aligned}E_x &= (\Delta_1^2 - \sin^2 \theta + k^2 v) (\exp \{k\Delta_1 z\} - \exp \{k\Delta_1(2H - z)\}) \\ &\quad + \gamma(\Delta_2^2 - \sin^2 \theta + k^2 v) (\exp \{k\Delta_2 z\} - \exp \{k\Delta_2(2H - z)\}) \\ E_y &= -k^2 \rho Y[(\exp \{k\Delta_1 z\} - \exp \{k\Delta_1(2H - z)\}) + \gamma(\exp \{k\Delta_2 z\} - \\ &\quad \exp \{k\Delta_2(2H - z)\})]\end{aligned}$$

which is a linear combination such that  $E_x = E_y = 0$  when  $z = H$ . Now at  $z = 0$ , this solution must be proportional to

$$\begin{aligned} E_x &= \exp \{ -ikz \cos \theta \} + {}_{11}R_{11} \exp \{ ikz \cos \theta \}, \\ E_y &= {}_{11}R_{\perp} \exp \{ ikz \cos \theta \}. \end{aligned}$$

where  ${}_{11}R_{11}$ ,  ${}_{11}R_{\perp}$  are the (complex) reflection and conversion coefficients.†

Putting  $z = 0$  and introducing the proportionality factor  $\omega$ , we have

$$\begin{aligned} \omega(E_x)_0 &= 1 + {}_{11}R_{11}, \\ \omega(E_y)_0 &= {}_{11}R_{\perp}, \\ (2.6) \quad \omega(E_x')_0 &= ik \cos \theta ({}_{11}R_{11} - 1), \text{ where } E_x' = \frac{\partial E_x}{\partial z}, \\ \omega(E_y')_0 &= ik \cos \theta {}_{11}R_{\perp}, \quad \text{where } E_y' = \frac{\partial E_y}{\partial z}. \end{aligned}$$

Thus  $(E_y'/E_y)_0 = ik \cos \theta$ , whence

$$(2.7) \quad \gamma = - \left[ \frac{\Delta_1 (1 + \exp \{ 2kH\Delta_1 \}) - i \cos \theta (1 - \exp \{ 2kH\Delta_1 \})}{\Delta_2 (1 + \exp \{ 2kH\Delta_2 \}) - i \cos \theta (1 - \exp \{ 2kH\Delta_2 \})} \right].$$

${}_{11}R_{11}$  and  ${}_{11}R_{\perp}$  are then found from the relations

$$(2.8) \quad (E_x/E_y)_0 - (E_x'/E_y')_0 = 2/{}_{11}R_{\perp},$$

$$(2.9) \quad (E_x/E_y)_0 + (E_x'/E_y')_0 = 2{}_{11}R_{11}/{}_{11}R_{\perp}.$$

We have made use of this analysis in order to construct Figs. 2(a) and 2(b), where we plot in effect log amplitude against log frequency for each of the two components of the downcoming wave. We consider the two cases  $KH = \infty$ ,  $KH = 7$  when  $K$  and  $H$  are defined in Fig. 1. The ratio  $\frac{K}{H}$  may be varied

merely by a lateral shift of the axes of reference; the scale of frequencies shown has been set so that the curves will correspond roughly to summer conditions as observed at Cambridge, with a sharp amplitude drop near 30 kc. per sec. at vertical incidence. Following Paper 1, we have assumed  $Z/Y = 1$ , implying an effective collision frequency of  $8 \times 10^6$  per second.

It will be seen that both components increase in amplitude as the angle of incidence increases. However, the amplitude of the reflection coefficient increases considerably more rapidly than does that of the conversion coefficient, so that the polarization ellipse becomes rather eccentric at very oblique incidence. These observations agree very well with those noted experimentally by Weekes (5), who made use of an aircraft to study the downcoming wave from GBR (16 kc. per sec.) at different distances from the transmitter. They may perhaps give us further confidence in the use of the model.

† Suppose the upgoing wave to be plane polarized, with its electric vector having no component perpendicular to the plane of incidence. The complex reflection coefficient  ${}_{11}R_{11}$  refers to the component of the resulting downcoming wave in the plane of incidence, while the conversion coefficient  ${}_{11}R_{\perp}$  refers to the corresponding component perpendicular to the plane of incidence.

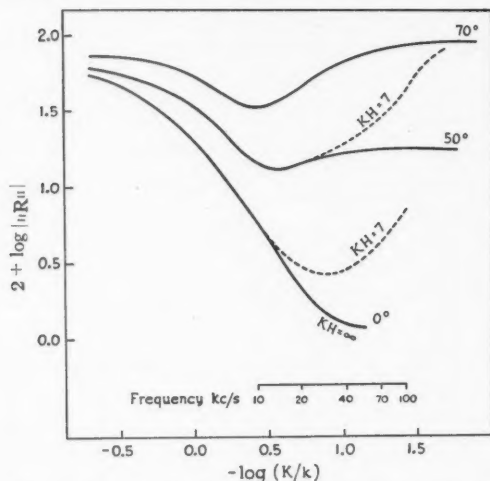


FIG. 2(a). Variation of the reflection coefficient  ${}_{11}R_{11}$  with frequency for angles of incidence  $0^\circ$ ,  $50^\circ$  and  $70^\circ$ .

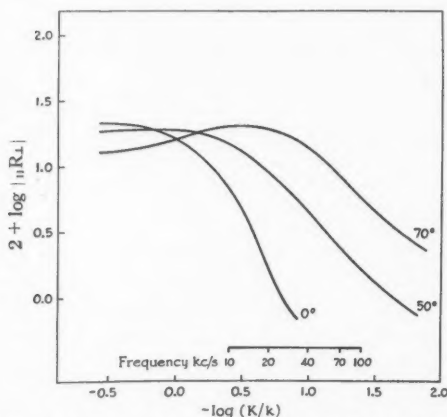


FIG. 2(b). Variation of the conversion coefficient  ${}_{11}R_1$  with frequency for angles of incidence  $0^\circ$ ,  $50^\circ$  and  $70^\circ$ .

The following conclusions seem to be of importance. It should be noted particularly that they are in fact *general* and it can be shown that they do not depend on the particular model chosen.

(1) The reflection coefficient increases with increasing angle of incidence at the ionosphere, and tends to unity at grazing incidence. Of course this is never attained in practice. Firstly, there will always be some nonionospheric ab-



sorption due to dust, water vapor, etc., which will become important at great distances from the transmitter, owing to the long path length. Secondly, an angle of incidence greater than about  $80^\circ$  is not possible because of the curvature of the earth.

(2) The polarization of the downcoming wave will change gradually from circular at vertical incidence to plane at grazing incidence.

Both of these conclusions are based on the assumption that the earth's magnetic field is vertical. In northern latitudes they may be expected to be approximately fulfilled. We also neglect the effect of second reflections. In the case of 16 kc. per sec. waves, these appear to become important beyond a distance of about 500 km. from the transmitter (5).

Thus in the case of GBR Rugby we should expect the measured reflection coefficient to increase and the polarization ellipse to become more eccentric as we move away from the transmitter. This condition will hold out to a distance of several hundred kilometers, beyond which the situation becomes obscure because of the possible influence of nonionospheric absorption and of second reflections.

### 3. Propagation in an Oblique Magnetic Field

Let us now consider Case (2), that of vertical incidence in an oblique magnetic field.

Putting  $\theta = 0$  in (2.1) we have

$$\begin{aligned} E_x[W + \sigma Y_z^2 + VD^2] + E_y[\sigma Y_x Y_y + \rho Y_z D^2] + E_z[\sigma Y_x Y_z] &= 0, \\ (3.1) \quad E_x[\sigma Y_x Y_y - \rho Y_z D^2] + E_y[W + \sigma Y_y^2 + VD^2] + E_z[\sigma Y_y Y_z] &= 0, \\ E_x[\sigma Y_x Y_z + \rho Y_y D^2] + E_y[\sigma Y_y Y_z - \rho Y_x D^2] + E_z[W + \sigma Y_z^2] &= 0. \end{aligned}$$

The determinantal equation is now

$$(3.2) \quad D^4[V^2(W + \sigma Y_z^2) + \rho^2 Y_z^2(W + \sigma Y^2)] + D^2 W V[2W + \sigma Y_z^2 + \sigma Y^2] + W^2[W + \sigma Y^2] = 0,$$

and we may consider the fundamental solutions

$$\begin{aligned} E_x &= [D^2(VW + V\sigma Y_z^2 + \rho\sigma Y_x Y_y Y_z) + W^2 + \sigma W(Y_y^2 + Y_z^2)] \exp D_z, \\ E_y &= [\rho Y_z D^2(\sigma Y_y^2 + W + \sigma Y_z^2) - W\sigma Y_x Y_y] \exp D_z. \end{aligned}$$

We are interested in a solution which vanishes at  $z = H$  and which is such that  $(E_y'/E_y) = ik$  at  $Z = 0$ . If the four solutions of the determinantal equation are  $\pm D_1, \pm D_2$ , then this solution is easily seen to be

$$\begin{aligned} E_x &= [D_1^2(VW + V\sigma Y_z^2 + \rho\sigma Y_x Y_y Y_z) + W^2 + \sigma W(Y_y^2 + Y_z^2)] [\exp D_1 z - \exp D_1(2H - z)] + \gamma [D_2^2(VW + V\sigma Y_z^2 + \rho\sigma Y_x Y_y Y_z) + W^2 + \sigma W(Y_y^2 + Y_z^2)] [\exp D_2 z - \exp D_2(2H - z)], \\ E_y &= [\rho Y_z D_1^2(\sigma Y_y^2 + W + \sigma Y_z^2) - W\sigma Y_x Y_y] [\exp D_1 z - \exp D_1(2H - z)] + \gamma [\rho Y_z D_2^2(\sigma Y_y^2 + W + \sigma Y_z^2) - W\sigma Y_x Y_y] [\exp D_2 z - \exp D_2(2H - z)], \end{aligned}$$

where

$$\gamma = - \left[ \frac{D_1(1 + \exp \{2HD_1\}) - ik(1 - \exp \{2HD_1\})}{D_2(1 + \exp \{2HD_2\}) - ik(1 - \exp \{2HD_2\})} \right].$$

${}_{11}R_{11}$ ,  ${}_{11}R_{\perp}$  are determined from (2.8) and (2.9) as before.

Let us first consider the case of north-south propagation ( $Y_y = 0$ ), where  $\vec{Y}$  is inclined at an angle of  $23^\circ$  to the vertical (this corresponds to conditions in

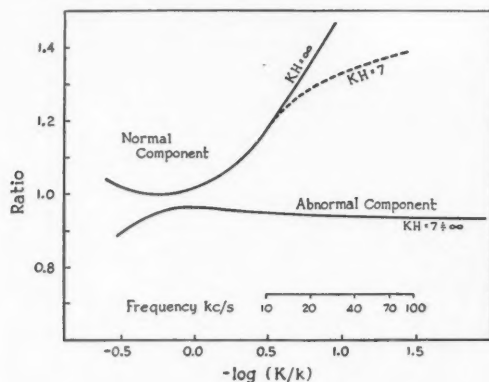


FIG. 3(a)

the south of England). We assume throughout that  $Z/Y = 1$ ,  $X/Y = K\sqrt{2/k}$ . In Fig. 3(a) we compare the values of  $|{}_{11}R_{11}|$  and  $|{}_{11}R_{\perp}|$  calculated for this case, with the corresponding values calculated on the assumption that  $\vec{Y}$  was di-

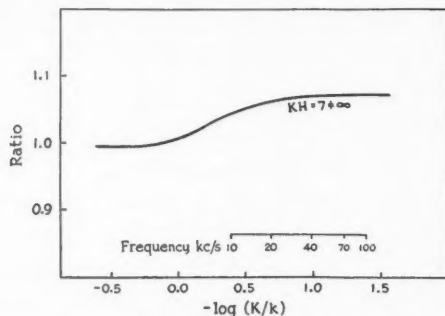


FIG. 3(b)

rected vertically [(note that the frequency scale in this figure corresponds to that of Fig. 2(a)]. We see that the two cases may well differ by as much as 10%.

If we consider the corresponding case of east-west propagation ( $Y_x = 0$ ) we find that the values of  $|{}_{11}R_{11}|$  and  $|{}_{11}R_{\perp}|$  are not greatly different from those obtained in the north-south propagation. In fact, it can be shown that the value of  ${}_{11}R_{\perp}$  is the same in the two cases. The conversion coefficient  ${}_{11}R_{\perp}$  is

not, however, independent of the direction of propagation; but to attempt to measure any variation experimentally, it would be necessary to compare propagation in directions, say, north and north-west of the transmitter. The extent of this variation would in any case be small, and could not likely be detected using present experimental techniques.

In Fig. 3(b) we compare the values of  $|R_{11}|$  corresponding to north-south and to east-west propagation. It will be seen that the variation here is quite small—considerably smaller in fact than the variation pictured in Fig. 3(a).

The chief argument, aside from mathematical convenience, in favor of using vertical-field theory in connection with observations made in northern latitudes has always been that very little dependence on direction from the transmitter has been observed in the downcoming wave (6). It will be seen from the above that this is not really a satisfactory test, particularly if measurements are made of the conversion coefficient alone, as is often the case. Vertical-field predictions might be in error by say 10%, but this test may still indicate only a 1% variation in field strength with direction from the transmitter. On the other hand, even a 10% variation is probably well within the limits of present experimental accuracy.

### Conclusions

The 'tarnished mirror' model of the ionosphere first considered in Paper 1 has been used to examine two important cases occurring in very long wave propagation. In the first case, the variation of reflection and conversion coefficients with angle of incidence, assuming the earth's magnetic field to be vertical, was exhibited. In the second case, the reflection and conversion coefficients at vertical incidence in a field inclined  $23^\circ$  to the vertical were examined. It was found that vertical-incidence theory, when applied in this situation, may result in errors in the calculated reflection and conversion coefficients considerably greater than direction-dependence experiments would indicate, but that in any case, these errors lie within the limits of present experimental accuracy.

### Acknowledgments

The writer wishes to express his thanks to Dr. M. V. Wilkes of the University Mathematical Laboratory, Cambridge, and to Mr. J. A. Ratcliffe of the Cavendish Radio Group for helpful suggestions and advice.

This work was carried out with the help of grants from the National Research Council of Canada and the Defence Research Board of Canada.

### References

1. BUDDEN, K. G., RATCLIFFE, J. A., and WILKES, M. V. Proc. Roy. Soc. (London), A, 171: 188. 1939.
2. FRAZER, R., DUNCAN, H., and COLLAR, J. Elementary matrices. Cambridge University Press, 1938.
3. STANLEY, J. P. J. Terr. Atm. Phys. In press.
4. STRAKER, T. W., BRACEWELL, R. N., and HARWOOD, J. J. Inst. Elec. Engrs., Pt. III. In press.
5. WEEKES, K. J. Inst. Elec. Engrs., Pt. III. 97: 100. 1950.
6. WILKES, M. V. Proc. Roy. Soc. (London), A, 189: 130. 1947.

## AN ATOMIC BEAM SOURCE AND SPECTROGRAPH FOR HYPERFINE STRUCTURE. NUCLEAR MOMENTS OF SILVER<sup>1</sup>

BY M. F. CRAWFORD, A. L. SCHAWLOW,<sup>2</sup> F. M. KELLY,<sup>3</sup> AND W. M. GRAY<sup>4</sup>

### Abstract

An atomic beam source and a fast spectrograph which have been used effectively in hyperfine structure investigations are described. The camera objective of the spectrograph is an off-axis paraboloidal mirror. The procedures used to determine the nuclear moments of the two silver isotopes,  $I = 1/2$  for each isotope,  $\mu(\text{Ag}^{107}) = -0.087$  n.m. and  $\mu(\text{Ag}^{109}) = -0.160$  n.m., are reported.

### Introduction

A major problem in spectroscopic hyperfine structure studies is the production of lines with sufficiently small half-widths. An important cause of line broadening in sources generally used in optical spectroscopy is the Doppler effect (31) which arises from the random thermal motion of the emitting atoms. The Doppler half-widths can be reduced by employing an atomic beam source (19) which confines the atoms to a narrow beam perpendicular to the line of sight. This paper describes an atomic beam source, together with a high speed spectrograph designed for hyperfine structure studies. The spectrograph employs an off-axis paraboloidal mirror as camera objective. The apparatus has been used for hyperfine structure studies of silver (9, 27), zinc (5, 13), and magnesium (7, 16). The determination of the nuclear moments of silver is described in detail.

### The Atomic Beam Source

In general the design of the atomic beam source is similar to those described by Paul (23), and Mundie and Meissner (22) except for the following features. The distance between the oven aperture and the collimating slit has been increased about fourfold so that the slit of the collimator can be enlarged without decreasing the collimation. Increasing the dimensions of the slit prevents clogging, even after many hours of operation, and simplifies the design of the electron gun since electrons from a large plane cathode can be made to traverse the beam without special focusing. As well, the cathode to anode distance has been reduced until the grid-anode separation is only slightly greater than the width of the atomic beam. With this arrangement of electrodes it is possible, by proper choice of potentials, to obtain either a large number of fast electrons traversing the beam or a dense space charge within the beam. The latter mode of operation of the electron gun is very effective in exciting levels that have a high excitation probability for slow electrons.

<sup>1</sup> Manuscript received August 3, 1950.

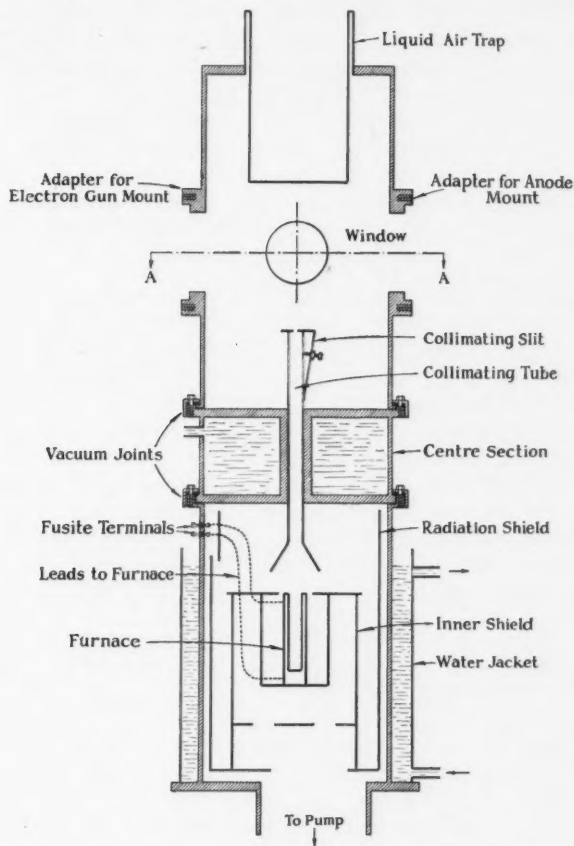
Contribution from the McLennan Laboratory, University of Toronto, Toronto 5, Canada.

<sup>2</sup> Present address: Columbia University, New York, U.S.A.

<sup>3</sup> Holder of a Fellowship from the National Research Council of Canada. Present address: Clarendon Laboratory, Oxford, England.

<sup>4</sup> Holder of a Fellowship from the Research Council of Ontario. Present address: University of Reading, Reading, England.

A vertical section of the atomic beam source is shown in Fig. 1. The outer container is constructed from 6 in. brass tubing and bronze castings. The lower chamber encloses the electrical resistance furnace and is surrounded by a water jacket. The central section is a water jacket which, except for the path



### ATOMIC BEAM LIGHT SOURCE

0 2 4  
Inches

FIG. 1. Atomic beam source, vertical section.

through the collimating tube, isolates the furnace chamber from the upper chamber. The circulating water ensures that the neoprene gaskets are kept cool. The upper, or excitation chamber, contains the electron gun. The liquid air trap built into this section improves the vacuum and condenses the beam.

The lower chamber is pumped directly with a high speed oil diffusion pump while the upper chamber is pumped through a side arm with a diffusion pump of a lower speed, but higher ultimate vacuum. A pressure of about  $10^{-5}$  mm. of mercury can be maintained in the upper section even when the furnace is at a temperature of  $1700^{\circ}\text{C}$ .

The design of the furnace depended on the substance to be evaporated. For silver and zinc the furnace was a crucible of fused alundum, 3 in. long,  $3/4$  in. O.D. at the top, and  $21/32$  in. O.D. at the bottom. A heating coil of 21 mil tungsten wire was wound on the outside of the alundum crucible, clamped at each end by nickel strips and then covered with a paste of levigated alumina to which some aluminum nitrate had been added. The turns were more closely spaced at the ends to maintain a more uniform temperature along the crucible. Before use the crucible was degassed in vacuum by keeping it above operating temperatures for several hours.

The temperature of the furnace for satisfactory evaporation of silver was  $1500$ – $1600^{\circ}\text{C}$ . This temperature was considerably higher than would be expected from vapor pressure data alone. Since the furnace opening was as large as the evaporating surface, the vapor escaped freely and the rate of efflux depended on the rate of evaporation rather than on the vapor pressure. Contamination of the surface of the molten metal reduced the rate of evaporation. The open end of the furnace did not clog because its temperature was above the melting point of silver. Since the vapor pressure of silver at its melting point is low, the silver was easily degassed without appreciable evaporation by keeping it molten for three or four hours. The zinc was degassed by pre-melting it in vacuum in a suitable Pyrex tube. One charge of this furnace lasted six to eight hours.

The open mouth furnace was found to be unsatisfactory for the evaporation of magnesium (16), which has an appreciable vapor pressure below its melting point. A new furnace was made from an iron crucible  $3\frac{1}{2}$  in. long and  $7/8$  in. I.D. A terminal in the form of an iron strip was fastened around each end of the crucible and insulated from it by small pieces of fused alundum. A mixture of levigated alumina and aluminum nitrate was then baked on the outside to form an insulating layer; tungsten wire was wound on it and attached to the terminals. The windings were more closely spaced at the top to ensure that the opening was at a higher temperature than the rest of the furnace. A recessed iron cap,  $3/8$  in. thick with a  $1/8$  in. central hole, was placed in the top of the furnace. With this arrangement the magnesium could be melted, degassed, and evaporated to produce a satisfactory beam. One charge of magnesium lasted 15 hr.

The collimating tube is rectangular in cross section except at the bottom where it is flared to collect most of the metal evaporated from the furnace. This collimating tube was satisfactory for zinc and silver, but tended to clog up at the lower end before the charge of magnesium was completely evaporated

from the furnace. The center section, shown in Fig. 2, was satisfactory for collimating the magnesium beam. The collimating slit shown in Fig. 2 was in the same position relative to the electron gun as the collimating slit shown in Fig. 1.

The collimation could be changed by adjusting the length (dimension in the line of sight) of the upper slit. For the very high collimations required in the silver problem a vertical strip was placed centrally in the collimating tube

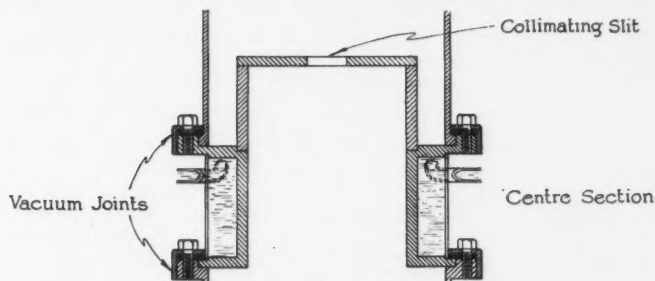


FIG. 2. Center section used to prevent clogging.

shown in Fig. 1, effectively making a double beam. The collimation obtained during an experiment can be measured directly. If  $l$  is the length of the deposit of metal on the liquid air trap,  $s$  the length of the exit slit of the collimating tube measured parallel to the line of sight, and  $d$  the distance from the slit to the deposit, the collimation is given by

$$C = \frac{2d}{l - s}.$$

The measured values agreed closely with those predicted from the geometry of the collimating system (19).

The metal condensed on the collimator could be easily reclaimed. Reclaimed silver was used and found to be less gassy than a fresh charge. Magnesium and zinc, which are inexpensive and readily available, were not reclaimed, since their condensates were porous and gassy.

The electron gun is shown in cross section in Fig. 3. The gun is mounted on a brass disk which fits into the adapter on the left side of the upper chamber. The vacuum seal is made with a neoprene gasket. Ten oxide coated filaments of fine spiral tungsten wire 3/4 in. long are held coplanar and parallel, 1/8 in. apart, by set screws in two brass bars. The filaments are the type used in 40 w. fluorescent lamps stretched and cut in half. The bars are supported on two Fusite terminals\* mounted in a nickel plate. The nickel plate is supported by a rod which slides in a brass tube to permit adjustment of the plane of the

\* Obtained from the Fusite Corporation, Cincinnati, Ohio, U.S.A.



filaments to any desired distance from the plane of the grid. The brass tube is fastened to the mounting disk and can be moved transversely to place the filaments opposite the spaces between the grid wires.

The nine tungsten grid wires are parallel to the filaments, but opposite the spaces between them. They are held at one end by set screws in a nickel bar, but slide freely in holes in the lower bar to prevent buckling when hot. The nickel bars are fastened to a brass support which is soldered into a glass-to-metal seal in the mounting plate.

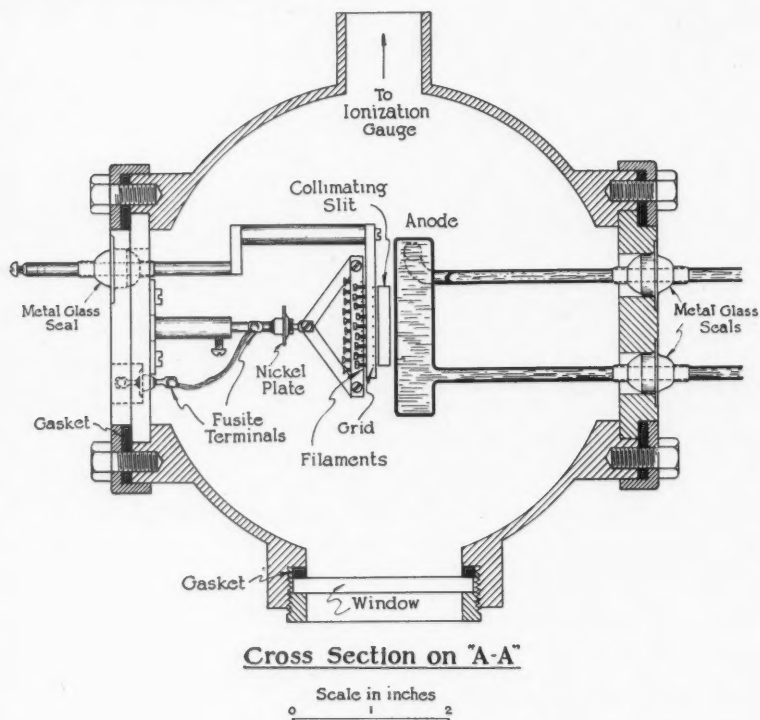


FIG. 3. Cross section of the upper chamber.

The plane of the grid is adjusted to be 7 mm. from the face of the anode and is left fixed. The filaments are correctly positioned relative to the grid by motion of the filament support. The plane of the filament is about 1.5 mm. from the plane of the grid. When the filaments require recoating or replacement the filament unit can be removed. A small variable transformer supplies the heating current for the filaments, which are operated in parallel. Operating temperatures are obtained with a potential of 3 to 4 v. across each filament.



The radiation-cooled grid just described becomes white hot during operation, and is satisfactory only for the analysis of ultraviolet lines. For visible lines a water-cooled grid is used; in it stainless steel tubes 0.042 in. O.D. and 0.029 in. I.D. replace the grid wires. The grid tubes are hard soldered to german silver tubes which support the grid and pass through large glass-to-metal seals in the mounting plate for the gun. Tap water, passed through the grid at 300 cc. per min., supplies adequate cooling.

The water-cooled anode is shown in Fig. 3. It is a hollow box turned from a solid copper cylinder and completed by brazing a copper plate on the back. It is supported by the two tubes which carry the water. The tubes pass through and are soft soldered to large glass-to-metal seals\* soldered to the base plate. This plate fits into the adapter at the right hand side of the upper chamber and is sealed by a neoprene gasket. A separate power supply is used for each of the grid and anode. Each circuit has a 700 ohm series resistor to limit the current in case of gas bursts.

The optimum conditions of operation of the gun for the excitation of each line studied were determined. The procedure was to maintain the grid current at its maximum safe operating value, 500 ma. for the water-cooled grid and and 250 ma. for the radiation-cooled grid, by small adjustments of its potential, and to raise the anode potential in steps from zero to 1000 v. above that of the filaments. The variation of the intensity of the line with the anode potential was observed photographically or visually with the spectrograph to determine the optimum condition.

The silver resonance lines were excited using the radiation-cooled grid and a grid current of 250 ma. They were found to be almost equally intense with the anode at 1000 v. and the anode current 1.2 amp., and with the anode at 70 v. and the anode current 70 ma. The second method of excitation was used because much less gas was produced by the electron bombardment of the anode.

For the excitation of triplet levels in the spectrum of magnesium and zinc it was found to be advantageous to reduce the anode potential to less than 70 v. With these anode potentials a space charge forms in the region between the grid and the anode. The low velocity electrons of the space charge excite triplet levels very effectively, since the probability of excitation (4) has a narrow maximum at potentials of a few volts. Lines originating in singlet levels were found to be most intense with the anode potential between 200 and 300 v. The faster electrons are more efficient in this case since the probability of excitation of a singlet state has a broad maximum at potentials above the ionization potential.

The dependence of the excitation of triplet and singlet levels in the arc spectrum of magnesium on anode potential was quite marked. Visual observations showed that the green triplet lines at 5183, 5172, and 5167 Å were most

\* Type GA 95.2013 supplied by the Stupakoff Ceramic and Manufacturing Company, Latrobe, Pa., U.S.A.

intense with the anode potential less than 25 v. above that of the filaments. As the anode potential was increased, the triplet lines became less intense and disappeared at potentials greater than 100 v. The visible lines of the diffuse singlet series, however, were not observable through the spectrograph with low anode potentials, but appeared with potentials above 75 v., and reached a maximum intensity with the anode potential at 200 to 300 v. This effect was also observed by Mundie (21).

### Spectroscopic Equipment

The brightness, or intrinsic luminosity, of an atomic beam source is low. Therefore, it is advantageous to use a fast spectrograph to provide the primary dispersion for the Fabry-Perot interferometer. Such a spectrograph in which an off-axis paraboloidal mirror is the camera objective has been constructed and has proved to be particularly useful for hyperfine structure investigations.

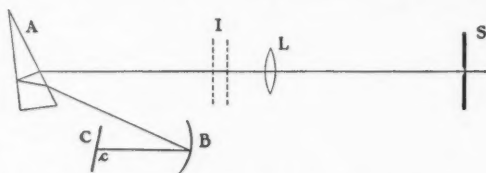


FIG. 4. Schematic diagram of the spectrograph.

A schematic diagram of the spectrograph is shown in Fig. 4. The collimator lens,  $L$ , is a quartz-fluorite achromatic triplet of 5 cm. diameter and 110 cm. focal length. The dispersing element,  $A$ , is a  $30^\circ$  back-reflecting prism. It can be rotated about a vertical axis to center the refracted beam of a desired wave length on the camera objective,  $B$ , which is an off-axis paraboloidal mirror of the type used in the Perkin-Elmer infrared spectrometer. The mirror is  $18^\circ$  off-axis, has a diameter of 7.5 cm., a focal length of 28 cm., and is front surfaced with aluminum. The mirror and the plate holder,  $C$ , are mounted on a common support forming the camera unit. The Fabry-Perot interferometer is placed at  $I$ .

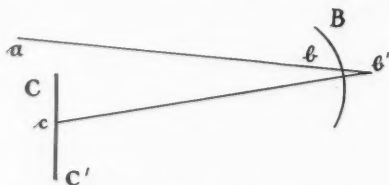


FIG. 5. Schematic diagram of the camera unit.

A schematic diagram of the camera unit is shown in Fig. 5.  $CC'$  represents the plate holder, which can be rotated about a vertical axis through the point  $c$  in the plane of the photographic emulsion.  $B$  is mounted as described by

Martin *et al.* (17), and can be rotated about three mutually perpendicular axes which intersect at a point a short distance behind  $b$ , the center of the reflecting surface. One of these axes is normal to the surface of the mirror, one is in the plane of the diagram, and one is normal to the plane of the diagram.  $B$  can be moved along  $ab$ , the direction of the rays leaving the prism  $A$ . The camera unit can be rotated about a vertical axis through the point  $b'$ . The construction is such that when the spectrograph is in adjustment  $b$  and  $b'$  are practically coincident, and  $ab$  is parallel to the axis of the mirror.

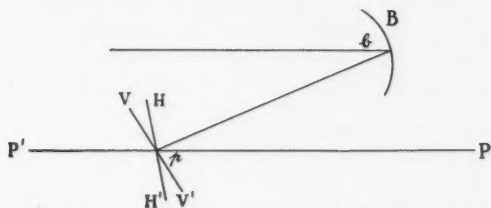


FIG. 6. Schematic diagram of focal curves of the paraboloidal mirror.

The properties of the mirror,  $B$ , may be described briefly by reference to Fig. 6.  $PP'$  represents the axis of the mirror. A parallel beam of light incident on  $B$  in the direction  $PP'$  is brought to a stigmatic focus at the point  $c$  on  $PP'$ . A parallel beam incident in any direction in the plane  $PP'b$  making an angle with  $PP'$  is not brought to a stigmatic focus. Instead, there are two line foci, one parallel to the plane  $PP'b$  and the other normal to it. The former will be called the  $H$  focus since  $PP'b$  is horizontal when the camera is in adjustment, and the latter the  $V$  focus. The line  $HH'$  in Fig. 6 indicates the locus of the  $H$  focus for directions of incidence close to  $PP'$ .  $VV'$  indicates the locus of the  $V$  focus.

The midpoints of the collimator lens, prism, and camera mirror define the horizontal plane. The adjustment of the camera consists in bringing  $p$ , the geometrical focus of the mirror, into coincidence with  $c$ , the point where the axis of rotation of the plate holder cuts the horizontal plane, and in bringing the axis  $PP'$  into this plane.

The following procedure is used to focus the spectrograph. The collimator lens is focused accurately for mercury green radiation by autocollimation. Then, a parallel beam from a small aperture at the center of the slit is thrown onto  $B$  by means of a plane reflector (an interferometer plate) substitute for  $A$ . The mirror,  $B$ , which has been placed in its mounting in approximately the correct orientation is rotated about the two axes perpendicular to the normal to the mirror to bring this beam to a focus at  $c$ . The image is then examined by means of a knife edge mounted in the plane of the plate holder  $CC'$ . The knife edge is moved horizontally with the edge vertical to test the  $V$  focus and vertically with the edge horizontal to test the  $H$  focus. The eye is placed to

view the full aperture. If the shadow crossing the aperture when the knife edge is moved either vertically or horizontally is not parallel to the knife edge,  $PP'$  is not in the horizontal plane defined above, and the mirror must be rotated about the normal to its surface until the shadow is parallel to the knife edge. This adjustment brings  $PP'$  into the horizontal plane.

The next step is to test the  $V$  and the  $H$  foci at  $c$ . If they are not coincident the axis  $PP'$  is not parallel to  $ab$ , the direction of the incident beam, and the camera unit must be rotated about the vertical axis through  $b$ . This rotation causes the image to move from  $c$  and it is brought back to  $c$  by a smaller counter rotation of  $B$  about its vertical axis. By successive approximations in these two rotational adjustments, and the adjustment of  $B$  along the line  $bc$ , the  $H$  and  $V$  foci are made to coincide at  $c$  giving a stigmatic image.

The final step is to determine the setting for which  $CC'$  coincides with  $HH'$  and the setting for which it coincides with  $VV'$ . By rotating the plane reflector,  $A$ , the image is moved to a position to one side of  $p$ . The plate holder is then rotated about the vertical axis through  $c$  into the correct focal position as determined by the knife edge test. The two settings of the plate holder are checked for several positions of the image on both sides of  $c$ .

The plate holder is used in the  $HH'$  position to record the interference pattern. Since the fringes run horizontally across the vertical spectral image this setting gives the best definition. The definition is good over a spectral range extending about 1 cm. to both sides of the geometrical focus. Even at the geometrical focus the mirror is used to the best advantage with this arrangement because the residual errors normally present in off-axis paraboloidal mirrors (29) impair the definition of the vertical focus more than that of the horizontal focus.

In high resolution spectroscopy it is usually necessary to study one line at a time, because the exposure times are dependent on the intensities of the components and the selection of suitable spacers is dependent of the separations of the components. Thus, in this application the fact that the spectrograph gives a good focus only over a short spectral range is not a limitation. Indeed, the use of the paraboloidal mirror as a camera objective has important advantages. The camera, once it has been critically focused for parallel visible light, is in focus for all wave lengths, and a stigmatic image of the fringe system of any spectral line is obtained merely by rotating the prism to bring the line to the geometrical focus of the mirror. Secondly,  $f/4$  mirrors giving excellent definition from 2100Å up can be readily procured and are inexpensive.

The quality and the adjustment of the collimator lens are important only for the primary resolution. An achromat is advantageous since sufficiently good images of the slit are then formed over a wide range of wave lengths without readjustment.

The linear dispersion of this instrument is small when a single back-reflecting prism is used. When greater dispersion is required the single prism is replaced

by a train consisting of a  $60^\circ$  prism and a back-reflecting  $30^\circ$  prism, of glass or quartz depending on the spectral region. The angle between the incident and emergent beams must be kept to a minimum when the train is used, or the aperture will be seriously reduced. The angle is  $5^\circ$  in this spectrograph. There is a small loss for the radiation focused at  $c$  and a slightly greater loss for the radiation focused to either side of  $c$ , but this is not serious for any radiation in good focus on the plate. A wide grating ruled to throw most of the intensity in a high order would give adequate dispersion without leading to aperture difficulties.

The interferometer mount and the invar spacers follow a design developed by K. W. Meissner (20). The interferometer plates are crystalline quartz flats 7 cm. in diameter. Silver films are used for the visible and aluminum films for the ultraviolet region of the spectrum. Aluminum films (6) prepared by rapid evaporation have been found to be quite good in the ultraviolet region and have been used to resolve very small structures at  $2137\text{\AA}$  (5). The plates are coated in a Ritschl-type evaporator (25) with an all-metal vacuum envelope (13). The aluminum was evaporated from a tungsten filament and the silver from a molybdenum strip of the form described by Tolansky (32). Experience has shown that if care is taken to use the same procedure for each evaporation, the charge of aluminum required to produce a given transmission coefficient can be predetermined with reasonable accuracy (13). It was found that the optical density (defined as the logarithm of the reciprocal of the transmission coefficient) is, for complete evaporation, proportional to the mass of aluminum placed on the filaments.

### Nuclear Moments of Silver

The nuclear magnetic moments of the two isotopes of silver,  $\text{Ag}^{107}$  and  $\text{Ag}^{109}$ , as determined by previous spectroscopic investigations are negative and small. Hill (14), using a water-cooled hollow cathode light source, studied the hyperfine structure of the Ag I resonance lines,  $5s^2S_{1/2} - 5p^2P_{1/2, 3/2}$  (3383, 3281 $\text{\AA}$ ). Because of the breadth of the lines emitted by his source, he only partially resolved the magnetic splitting, and did not separate the components belonging to the two isotopes. Jackson and Kuhn (15) investigated the absorption of the resonance lines in an atomic beam, resolved the splitting of the  $^2S_{1/2}$  level and separated the isotopic components. They observed four components, a very close pair of stronger components and a pair of weaker components with longer wave lengths.

In the assignment of components to the isotopes the experimental difficulty is to determine which of the two stronger components, separated by only  $0.013\text{ cm.}^{-1}$ , is the more intense. From photographs made with a 5 cm. etalon, Jackson and Kuhn decided that the component with the higher frequency was somewhat weaker and assigned it to  $\text{Ag}^{109}$ . However, they pointed out that it was not easy to determine which is the stronger on account of the closeness of the components. Their 6 cm. etalon pattern showed these two components

more clearly resolved, but they pointed out that here the intensities are confused owing to the close proximity of a lower frequency components in the adjacent order. It has been shown recently (33) that the abundance ratio of  $\text{Ag}^{107}$  to  $\text{Ag}^{109}$  is 51.35: 48.65, much lower than the ratio 1.3: 1 stated by Jackson and Kuhn. In view of the recently determined abundance ratio and the uncertainty in their intensity measurements, the assignment of components to isotopes made by Jackson and Kuhn is not conclusive, particularly since in the absorption method any overlapping of orders of the emission line would tend to make the apparent absorption of the higher frequency component of the stronger pair less than that of the lower frequency component. The alternative assignment would mean that the nuclear magnetic moments of the two isotopes are nearly equal instead of having a ratio of approximately 2: 1. To obtain further evidence on the assignment of components the hyperfine structure of the resonance lines excited in the atomic beam source were investigated.

With a 2.1 cm. etalon each resonance line showed two components. A comparison of this pattern with the pattern from the 4 cm. etalon showed that the weaker component of each line has the longer wave length. Thus the nuclear magnetic moments of both silver isotopes are negative, in agreement with the results of previous investigations.

With a 4 cm. spacer and aluminum films with 88% reflectivity, the weaker component of the 2.1 cm. pattern was clearly resolved into two. In the best 4 cm. patterns the stronger component was also resolved into two components. These patterns were used to measure the relative intensities of the weaker components because they were well separated from the stronger components. The 5 cm. etalon showed all four components clearly resolved. The patterns obtained with this spacer were used to measure the relative intensities of the stronger components. A reproduction of the 5 cm. etalon pattern enlarged approximately 25 times is shown in Fig. 7.

Exposures made with a 5.5 cm. etalon showed all four components, but one of the weak components was so close to a strong component of the next order that these patterns were not satisfactory for intensity measurements. However, these patterns were used to measure the separation of the two close strong components. Four and five centimeter patterns were used to measure the other separations and gave consistent results.

Fig. 8 shows the four components into which the line ( $^2S_{1/2} - ^2P_{3/2}$ ) was resolved. Designating the components (a), (b), (c), and (d) in increasing order of wave length, (a) and (b) have nearly the same intensity, while (c) and (d) are weaker than the first two, but again nearly equal. Therefore one of (a) and (b), and one of (c) and (d) arise from the same isotope, and the stronger of each pair belongs to the more abundant isotope  $\text{Ag}^{107}$ . Thus the components may be uniquely assigned to isotopes by measuring the intensity ratios  $i_a/i_b$  and  $i_c/i_d$ . To determine the relative intensities of the components the photographic plates were calibrated by exposures obtained with a stepped slit illuminated



PLATE I

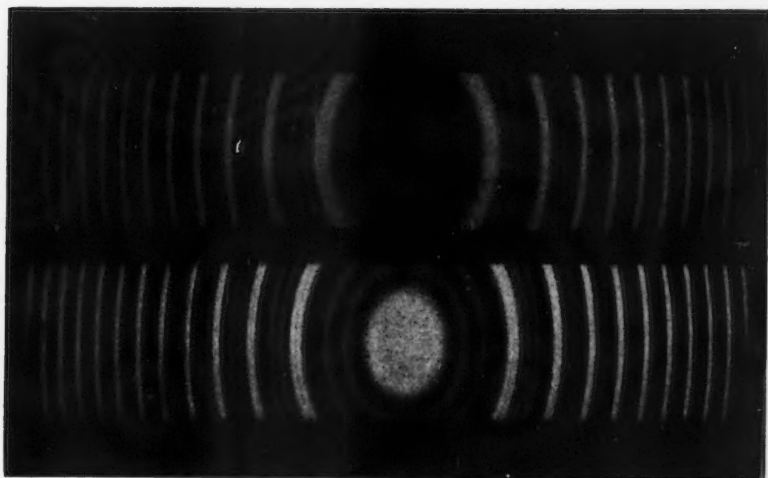
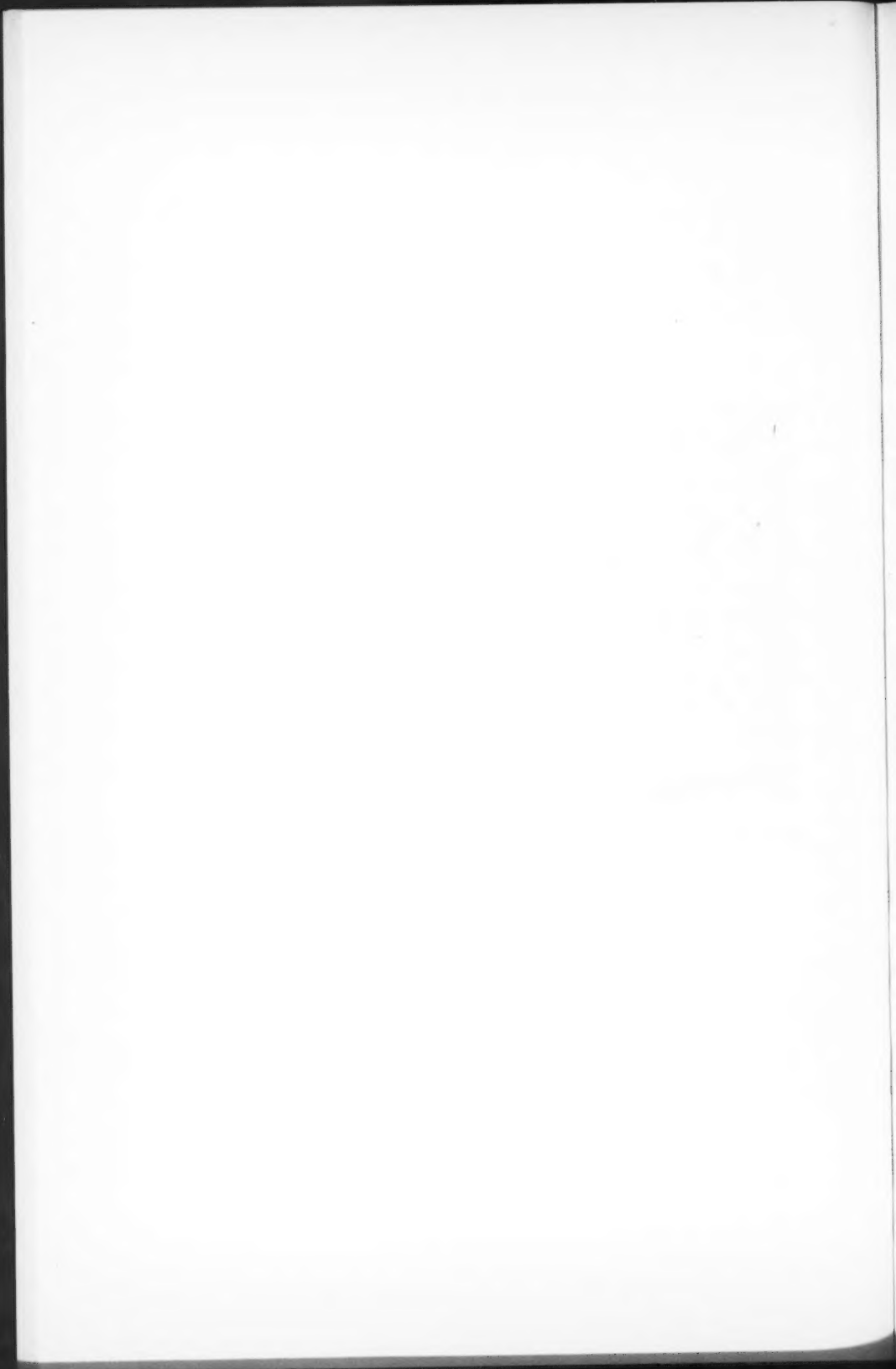


FIG. 7. The patterns obtained with a 5 cm. etalon enlarged 25 times. Upper pattern,  $\lambda 3281$ ; lower,  $\lambda 3383$ .





by the continuous radiation from a hydrogen lamp diffused by a quartz screen. Density contours of the components were obtained with a Leeds and Northrup recording microphotometer.

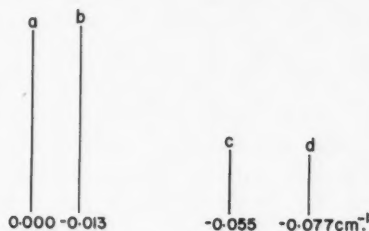


FIG. 8. Separations of the components of  $^2S_{1/2} - ^2P_{3/2}$ . The heights of the lines are proportional to the observed intensities.

#### Assignment of Components to Isotopes

The microphotometer traces of the 5 cm. patterns showed that the component (b) was more intense than (a). The ratio of the peak intensities measured from 22 fringes on three exposures was found to be  $i_b/i_a = 1.03 \pm 0.02$ , where 0.02 is the probable error of an individual reading. Therefore component (a) belongs to  $\text{Ag}^{109}$  and (b) belongs to  $\text{Ag}^{107}$ . From 35 fringes on four exposures with the 4 cm. etalon, the intensity ratio  $i_c/i_d = 1.05 \pm 0.04$ , so that (c) belongs to  $\text{Ag}^{107}$  and (d) belongs to  $\text{Ag}^{109}$ . These measured intensity ratios agree with the abundance ratio (1.05:1) of the two silver isotopes. Our assignment of components to isotopes agrees with that of Jackson and Kuhn (15).

#### Determination of $I$

Since the measured intensity ratio  $i_b/i_a$  and  $i_c/i_d$  are each equal to the isotopic abundance ratio, the  $I$  values of the two isotopes are the same. Then  $I$  can be determined from either of the ratios  $i_a/i_d$  or  $i_b/i_c$ . However, since the separation of (a) and (b) is very small and their intensities are nearly equal it is more accurate to measure the ratio  $(i_a + i_b)/(i_c + i_d)$ . The intensity of each pair of components was determined by plotting several fringes on an intensity scale and graphically integrating the area under each pair of components. For an accurate determination the integration must be over a complete order, since the intensity is not zero at the minimum. In this way, from one of the best 4 cm. patterns,  $(i_a + i_b)/(i_c + i_d) = 2.26 \pm 0.04$ . This ratio shows that  $I < 1$ , but because of the self-absorption of the resonance line in the atomic beam it is not as high as the ratio 3:1 expected for  $I = 1/2$ . An evaluation of the effect of self-absorption is made below and shows that the observed ratio is in excellent agreement with that calculated for  $I = 1/2$ .

The self-absorption reduces the intensity ratio between the two resonance lines. By comparing the experimental value of their intensity ratio with that calculated assuming self-absorption,  $I = 1/2$ , and the theoretical ratios of the

transition probabilities the absorption can be evaluated and used to determine quantitatively, for the conditions of the experiment, the effect of absorption on the ratio  $(i_a + i_b)/(i_c + i_d)$ . This correction is readily made because the two resonance lines are only 100 Å apart in a region where the photographic sensitivity is varying slowly.

In calculating the effect of self-absorption the hyperfine structure splittings of the  $^2P$  levels are neglected, so that each resonance line can be considered as having four components, two due to each isotope. Further it is assumed that the half-widths of each component are small compared to the smallest structure which has been resolved. Consequently the absorptions in the four components can be evaluated independently of one another. This is justifiable in view of the high collimation of the source. The absolute values of the absorption coefficients depend on both the density of the beam and the transition probabilities which in this case are simply related to the statistical weights. Consider one component emitted in a lamina of the beam of depth  $dx$  at a distance  $x$  from the front boundary of the beam. Let its intensity per unit depth be  $i'$  and the absorption coefficient per unit depth be  $k$ . Then the intensity of this component emerging from the beam of total depth  $D$  is

$$i = \int_0^D i' e^{-kx} dx = \frac{i'(1 - e^{-kD})}{k}.$$

The absorption coefficient  $k$  is proportional to  $i'$  and can be set equal to  $Ki'/D$ , where  $K$  is dependent only on frequency and is the same within 10% for all components of both resonance lines.

The four  $\text{Ag}^{109}$  components in the two resonance lines have in the absence of absorption relative intensities  $i'$  and  $3i'$  for the two in ( $^2S_{1/2} - ^2P_{1/2}$ ) and  $2i'$  and  $6i'$  for the two in ( $^2S_{1/2} - ^2P_{3/2}$ ). The intensities of the four components emitted by  $\text{Ag}^{107}$  relative to those of  $\text{Ag}^{109}$  are those listed above, multiplied by 1.05, the relative abundance of the two isotopes. This 5% difference in relative abundance can be neglected for the calculation of the correction for absorption. Thus the expression for the intensity ratio of the two resonance lines is

$$\frac{i(^2S_{1/2} - ^2P_{3/2})}{i(^2S_{1/2} - ^2P_{1/2})} = \frac{(1 - e^{-6Ki'}) + (1 - e^{-2Ki'})}{(1 - e^{-3Ki'}) + (1 - e^{-Ki'})}.$$

The solution of the transcendental equation obtained by equating this expression to 1.64, the intensity ratio measured by integrating over several orders for both resonance lines, is  $Ki' = 0.18$ .

The predicted intensity ratio of the two strong components to the two weak components in the ( $^2S_{1/2} - ^2P_{3/2}$ ) transition, for  $I = 1/2$  and the above value of the absorption coefficient  $Ki'$ , is

$$\frac{i_a + i_b}{i_c + i_d} = \frac{1 - e^{-6Ki'}}{1 - e^{-2Ki'}} = 2.20.$$

The experimental value, 2.26, is within 3% of this calculated value. Thus the intensity measurements establish conclusively that  $I = 1/2$  for both isotopes. The absorption also reduces the ratio  $i_b/i_a$  from 1.05, the relative abundance of the two isotopes, to 1.03, which is the value actually measured. The absorption reduces the intensity ratio of the weaker pair by a negligible amount, 0.7%.

#### *Nuclear Magnetic Moments of the Silver Isotopes*

The separations of the components of the ( $^2S_{1/2} - ^2P_{3/2}$ ) transition were measured from microphotometer traces with a linear magnification of 250. The position of the peak of the component can be located more objectively on the traces than by visual inspection of the plates. The variations of the linear magnifications are negligible over the very short distances measured, and the results are remarkably consistent.

The rectangular array method (31) was used to compute the wave number separations. From 39 orders on eight patterns,  ${}_a\Delta_b = 0.011 \pm 0.001 \text{ cm}^{-1}$ . From 28 orders on six patterns,  ${}_a\Delta_c = 0.0538 \pm 0.0003 \text{ cm}^{-1}$ , and  ${}_a\Delta_d = 0.0757 \pm 0.0003 \text{ cm}^{-1}$ . But components (a) and (b) are partially overlapping, and the measured separation is less than the true separation. Estimates from the shape of the fringes and measurements on two 5.5. cm. etalon patterns show that the components (a) and (b) are  $0.002 \text{ cm}^{-1}$  further apart than the peaks on the interferometer pattern. Then the revised separations are:  ${}_a\Delta_b = 0.013 \text{ cm}^{-1}$ ;  ${}_a\Delta_c = 0.055 \text{ cm}^{-1}$ , and  ${}_a\Delta_d = 0.077 \text{ cm}^{-1}$  with an uncertainty of  $\pm 0.001 \text{ cm}^{-1}$ . These separations agree with those reported by Jackson and Kuhn (15) except that component (c) is  $0.003 \text{ cm}^{-1}$  closer to (d) than found by them.

The isotope shift in this line is very small,  $0.004 \text{ cm}^{-1}$ , with the centroid of the  $\text{Ag}^{109}$  components having the higher frequency. When the normal mass shift is subtracted from the measured shift the residual shift is less than the experimental error.

To obtain an accurate value of the hyperfine structure separations of the  $^2S_{1/2}$  levels from the measured separations of the components of the ( $^2S_{1/2} - ^2P_{3/2}$ ) transition the small unresolved splitting of the  $^2P_{3/2}$  must be taken into account. The formulas of Goudsmit (12) with the addition of the Fermi-Segré correction (11) give  $\Delta\nu(^2S_{1/2}) = 32.4 \Delta\nu(^2P_{3/2})$ . Then the measured  ${}_a\Delta_c = 0.042 \text{ cm}^{-1}$  gives  $\Delta\nu(^2S_{1/2}) = 0.043 \text{ cm}^{-1}$  for  $\text{Ag}^{107}$ , and  ${}_a\Delta_d = 0.077 \text{ cm}^{-1}$  gives  $\Delta\nu(^2S_{1/2}) = 0.079 \text{ cm}^{-1}$  for  $\text{Ag}^{109}$ . The nuclear magnetic moments calculated from the hyperfine structure splitting of the  $^2S_{1/2}$  levels by the Goudsmit formula with a Fermi-Segré correction evaluated by the method of Crawford and Schawlow (8) from Shenstone's (30) term values are (9):

$$\mu^0(\text{Ag}^{107}) = -0.084 \text{ n.m.}$$

$$\mu^0(\text{Ag}^{109}) = -0.155 \text{ n.m.}$$

These values, designated by  $\mu^0$ , are derived assuming a point nucleus. A correction for the finite size of the nucleus must be applied (8, 26). For  $y_0 =$

$0.0127 \div y_1$  (2) and  $\rho = 0.939$ , where the symbols are defined in reference (8), the correction for the finite size of the nucleus is  $\delta = 0.024$ . A further correction for the volume distribution of the magnetic moment, estimated from the approximate formula of Bohr and Weisskopf (3), is  $\epsilon = 0.008$ . The corrected magnetic moment is  $\mu = \mu^0/(1 - \delta)(1 - \epsilon) = 1.03$  (3)  $\mu^0$ .

Thus

$$\mu(\text{Ag}^{107}) = -0.087 \text{ n.m.}$$

$$\mu(\text{Ag}^{109}) = -0.160 \text{ n.m.}$$

These moments agree reasonably well with the predictions of the single particle model for a configuration in which the 47th proton is in the  $2p_{1/2}$  level. The plausibility of such a configuration for the silver isotopes has been discussed by Mayer (18) from the point of view of a large spin-orbital interaction and by Feenberg (10) from a consideration of the distribution of particle density in the nucleus.

The values of the nuclear magnetic moment reported here are appreciably lower than those given by Jackson and Kuhn (15) primarily because they neglected the important Fermi-*Segré* correction which is 23% for the  $5s$  level of silver. Since the Fermi-*Segré* and finite size corrections are well established (8, 28), we consider that the uncertainty in the magnetic moments of the two isotopes is of the order of 2%.

#### Structure of the $^2S_{1/2} - ^2P_{1/2}$ Transition

The hyperfine structure of the  $5p\ ^2P_{1/2}$  level is three times the structure of the  $5p\ ^2P_{3/2}$  level. Thus the transitions to the  $F = 1$  state of the  $^2S_{1/2}$  level give rise to four components, two due to  $\text{Ag}^{109}$  designated ( $a_1$ ) and ( $a_2$ ) and two due to  $\text{Ag}^{107}$  designated ( $b_1$ ) and ( $b_2$ ). Taking the low frequency edge of this group as origin, ( $a_1$ ), ( $a_2$ ), ( $b_1$ ), and ( $b_2$ ) are in the interval 0 to  $-0.018 \text{ cm}^{-1}$ ; ( $c'$ ), the  $F = 1$  ( $^2P_{1/2}$ ) to  $F = 0$  ( $^2S_{1/2}$ ) component of  $\text{Ag}^{107}$  is at  $-0.062 \text{ cm}^{-1}$ ; and ( $d'$ ) the corresponding component of  $\text{Ag}^{109}$  is at  $-0.084 \text{ cm}^{-1}$ . The  $a$ -components were partially, but not clearly, resolved from the  $b$ -components. This separation was  $0.014 \text{ cm}^{-1}$ .

The theoretical pattern expected for this transition can be calculated using the values of the nuclear moments as determined above and the Goudsmit formula. The isotope shift can be determined from the accurately measured positions of ( $c'$ ) and ( $d'$ ), and has the same magnitude and sense as in the  $^2S_{1/2} - ^2P_{3/2}$  transition. The observed pattern agrees with that predicted within experimental error and thus confirms the  $I$  and  $\mu$  values deduced from the  $^2S_{1/2} - ^2P_{3/2}$  transition.

#### Isotope Shift

The isotope shift in each of the resonance lines is  $0.004 \text{ cm}^{-1}$  with the centroid of the  $\text{Ag}^{109}$  components having a higher frequency than the centroid of the  $\text{Ag}^{107}$  components. When the normal mass effect is subtracted from the measured shift the residual shift is  $0.001 \text{ cm}^{-1}$  and is less than the experimental error. Thus, the resultant shifts due to the field effect (26) and the

specific mass effect (1) in the three levels,  $5p\ ^2P_{3/2, 1/2}$  and  $5s\ ^2S_{1/2}$ , are the same within  $0.002\text{ cm}^{-1}$ . The equal shifts observed for the  $^2P$  levels are in agreement with the predictions of both the field effect and specific mass effect theories. The equality of the shifts in the three levels shows that the specific mass shift of the  $4d^{10}5p$  levels has the same magnitude as the combined field effect and specific mass effect shift of the  $4d^{10}5s$  level. Since the field effect theory predicts an observable shift for a single  $s$ -electron (8), and Rasmussen (24) has measured relatively large shifts in other lines of Ag I and Ag II, the very small shift observed in the Ag I resonance lines indicates that the shifts due to the specific mass effect are comparable to those due to the field effect.

### Acknowledgments

The authors are indebted to Prof. K. W. Meissner of Purdue University for the loan of an interferometer mount. His design was copied in detail and was very satisfactory. One of the authors (A.L.S.) expresses his appreciation of the opportunity of discussing atomic beam sources with Professor Meissner. F. M. Kelly is indebted to the National Research Council for a Studentship and a Fellowship; and W. M. Gray to the Research Council of Ontario for two Fellowships.

### References

1. BARTLETT, J. H. and GIBBONS, J. J. *Phys. Rev.* 44: 538. 1933.
2. BETHE, H. A. *Elementary nuclear theory.* John Wiley and Sons, Inc., New York. 1947.
3. BOHR, A. and WEISSKOPF, V. F. *Phys. Rev.* 77: 94. 1950.
4. BRODE, R. B. *Rev. Modern Phys.* 5: 257. 1933.
5. CRAWFORD, M. F., GRAY, W. M., KELLY, F. M., and SCHAWLOW, A. L. *Can. J. Research, A*, 28: 138. 1950.
6. CRAWFORD, M. F., GRAY, W. M., SCHAWLOW, A. L., and KELLY, F. M. *J. Optical Soc. Am.* 39: 888. 1949.
7. CRAWFORD, M. F., KELLY, F. M., SCHAWLOW, A. L., and GRAY, W. M. *Phys. Rev.* 76: 1527. 1949.
8. CRAWFORD, M. F. and SCHAWLOW, A. L. *Phys. Rev.* 76: 1310. 1949.
9. CRAWFORD, M. F., SCHAWLOW, A. L., GRAY, W. M., and KELLY, F. M. *Phys. Rev.* 75: 1112. 1949.
10. FEENBERG, E. *Phys. Rev.* 77: 771. 1950.
11. FERMI, E. and SEGRÉ, E. *Z. Physik*, 82: 729. 1933.
12. GOUDSMIT, S. *Phys. Rev.* 43: 636. 1933.
13. GRAY, W. M. *Ph.D. Thesis*, University of Toronto. 1949.
14. HILL, H. *Phys. Rev.* 48: 233. 1935.
15. JACKSON, D. A. and KUHN, H. *Proc. Roy. Soc. (London)*, A, 158: 372. 1937.
16. KELLY, F. M. *Ph.D. Thesis*, University of Toronto. 1949.
17. MARTIN, E. J., FISHER, A. W., MANDEL, B., and NUSBAUM, R. E. *J. Optical Soc. Am.* 37: 923. 1947.
18. MAYER, M. G. *Phys. Rev.* 78: 16. 1950.
19. MEISSNER, K. W. *Rev. Modern Phys.* 14: 68. 1942.
20. MEISSNER, K. W. *J. Optical Soc. Am.* 31: 405. 1941.
21. MUNDIE, L. G. *Ph.D. Thesis*, Purdue University, Lafayette, Indiana, U.S.A. 1943.
22. MUNDIE, L. G. and MEISSNER, K. W. *Phys. Rev.* 65: 265. 1944.
23. PAUL, W. *Z. Physik*, 117: 774. 1941.
24. RASMUSSEN, E. K. *Kgl. Danske Videnskab. Selskab, Mat. fys. Medd.* 18, No. 5. 1940.
25. RITSCHL, R. *Z. Physik*, 69, 578. 1931.
26. ROSENTHAL, J. E. and BREIT, G. *Phys. Rev.* 41: 459. 1932.
27. SCHAWLOW, A. L. *Ph.D. Thesis*, University of Toronto. 1949.
28. SCHAWLOW, A. L., HUME, J. N. P., and CRAWFORD, M. F. *Phys. Rev.* 76: 1876. 1949.
29. SCHULTZ, L. G. *J. Optical Soc. Am.* 36: 588. 1946.
30. SHENSTONE, A. G. *Phys. Rev.* 57: 894. 1940.
31. TOLANSKY, S. *High resolution spectroscopy.* Methuen and Co. Ltd., London. 1947.
32. TOLANSKY, S. *Multiple beam interferometry of surfaces and films.* Oxford University Press, London. 1948.
33. WHITE, J. R. and CAMERON, A. E. *Phys. Rev.* 74: 991. 1948.

## APPLICATIONS OF DIFFUSION THEORY TO EVAPORATION FROM DROPLETS AND FLAT SURFACES<sup>1</sup>

BY G. LUCHAK AND G. O. LANGSTROTH

### Abstract

It has been customary in applications of diffusion theory to evaporation problems to consider the liquid surface as fixed in solving for the vapor distribution in the adjacent space. A more rigorous treatment, involving solution of the diffusion equation with moving boundaries, has been applied to the problem of evaporation from droplets and flat surfaces. The results indicate that the equations obtained by the method of quasi-stationary states are good to a high degree of approximation under ordinary circumstances.

Previous applications of diffusion theory to the evaporation of droplets in still air (2, 3) have involved the assumption of 'quasi-stationary' states, i.e., it has been assumed that equilibrium conditions appropriate to the size of the droplet exist in the surrounding atmosphere at every instant. The theoretical investigation of this article has been made to ascertain how well equations based on this assumption may be expected to represent fact. It involved solution of the diffusion equation with a time-variable boundary condition descriptive of the continually decreasing size of the drop. The treatment given below is limited to conditions in which the mean free path of vapor molecules in air is negligibly small compared to the drop diameter, and disregards such factors as the dependence of the diffusion coefficient on the temperature distribution.

An exact solution of the diffusion equation satisfying the required boundary conditions was unattainable, and an iteration or successive approximation method of solution was adopted. It was possible however to obtain an exact solution for the corresponding problem of evaporation from a flat surface. This is included in this article (c.f. Zener's treatment of condensation on surfaces from solutions, reference (5)). Since it is the simpler problem in certain respects and provides some guidance in the treatment of droplet evaporation, it is dealt with in Section 1.

### 1. Evaporation from a Flat Surface

#### (a) *Diffusion of Vapor into Infinite Space above a Surface*

Let a large surface of a body of volatile liquid lie at the origin of ordinates ( $x = 0$ ) at time  $t = 0$ , and let the air above the surface be free of vapor initially. As evaporation proceeds, the surface of the liquid drops below the origin, and the vapor concentration  $c$  in moles per cubic centimeter becomes appreciable at any finite distance  $x$  above the origin. The vapor concentration at the surface of the liquid remains always at the saturation value  $c_0$ . If the position of the surface is given by some function  $x_s = a(t)$ , a solution of

<sup>1</sup> Manuscript received July 7, 1950.

Contribution from the Defence Research Board Experimental Station, Ralston, Alberta.



$$D \partial^2 c / \partial x^2 = \partial c / \partial t$$

is required which will satisfy the conditions

$$t = 0, \quad x > 0, \quad c = 0 \quad (1)$$

$$\text{any } t, \quad x = a(t), \quad c = c_0, \quad (2)$$

where  $D$  denotes the diffusion coefficient of the vapor in air. Since the rate of diffusion of vapor away from the surface is equal to the rate of mass loss of liquid per square centimeter of surface

$$-MD(\partial c / \partial x)_{x=a} = -\rho da / dt, \quad (3)$$

where  $M$  and  $\rho$  denote respectively the molecular weight of the vapor and the density of the liquid.

A solution of the diffusion equation

$$c(x, t) = -A \int_{\infty}^{x/\sqrt{\beta t}} e^{-s\lambda^2/2} d\lambda, \quad (4)$$

where  $\beta$  is a parameter,  $A$  a constant, and  $s = \beta/2D$ , satisfies conditions (1) and (2) if  $a(t) = -\sqrt{\beta t}$ ; Equation (3) can be satisfied by a proper choice of  $\beta$ . It follows from application of condition (2) to this equation, that

$$A = c_0 / \int_{-1}^{\infty} e^{-s\lambda^2/2} d\lambda.$$

Application of Equation (3) leads to

$$AMDe^{-s/2} = \rho\beta/2 = \rho Ds.$$

Hence

$$s = \frac{Mc_0}{\rho} \frac{e^{-s/2}}{\int_{-1}^{\infty} e^{-s\lambda^2/2} d\lambda} = \frac{Mc_0}{\rho} \frac{e^{-s/2}}{\sqrt{2/s} \int_{-\sqrt{s}/2}^{\infty} e^{-z^2} dz}$$

or

$$s^{1/2} = \frac{Mc_0}{\sqrt{2\rho}} \frac{e^{-s/2}}{\int_{-\sqrt{s}/2}^{\infty} e^{-z^2} dz}. \quad (5)$$

Even for water with a surface temperature of 20°C., the value of  $Mc_0/\rho$  is small (about  $1.7 \times 10^{-5}$ ) and hence  $s^{1/2}$  is also small. The exponential and integral in Equation (5) may be set equal to 1 and  $\sqrt{\pi}/2$  respectively with an error of about 1 in  $10^5$  in this instance. On this basis, it follows to a high degree of approximation that

$$\beta = \frac{D}{\pi} \cdot \left( \frac{2Mc_0}{\rho} \right)^2.$$

Consequently the lowering of the liquid surface by evaporation is described by

$$x_s = \frac{-2Mc_0}{\rho} \sqrt{Dt/\pi}, \quad (6)$$

and the rate of loss of mass per square centimeter of surface by

$$\frac{dm}{dt} = Mc_0 \sqrt{D/\pi t}. \quad (7)$$

(b) *Diffusion of Vapor into a Space Bounded by an Absorbing Wall Parallel to the Liquid Surface*

The situation is similar to that treated above, with the exception that a horizontal plane boundary a distance  $b$  above the origin maintains zero vapor concentration at its surface, and the initial concentration of vapor in the space is not zero, as will be discussed later. As before, the position of the liquid surface is given by  $x_s = a(t)$ . A solution of the diffusion equation

$$c(x, t) = A \int_0^{\frac{(x-b)}{\sqrt{b^2 + \beta t}}} e^{-s\lambda^2/2} d\lambda \quad (8)$$

satisfies the boundary conditions

$$x = b, c = 0 \quad (9)$$

$$x = b - \sqrt{b^2 + \beta t}, c = c_0 \quad (10)$$

and the flux equation

$$MD(\partial c/\partial x)_{x=a} = \rho da/dt \quad (11)$$

provided the constant  $A$  and the quantity  $s = \beta/2D$  are properly chosen. Since  $c = c_0$  when  $t = 0$ ,  $x = 0$ , Equation (8) gives

$$A = c_0 \int_0^{-1} e^{-s\lambda^2/2} d\lambda.$$

Evaluation of Equation (11) from Equation (8) yields

$$AMDe^{-s/2} = \rho\beta/2 = \rho Ds,$$

so that

$$s = \frac{Mc_0}{\rho} \frac{e^{-s/2}}{\int_0^{-1} e^{-s\lambda^2/2} d\lambda} = \frac{Mc_0}{\rho} \frac{e^{-s/2}}{\sqrt{2/s} \int_0^{-\sqrt{s/2}} e^{-z^2} dz}. \quad (12)$$

As pointed out earlier, the term  $Mc_0/\rho$  has a value of about  $1.7 \times 10^{-5}$  for water with a surface temperature of  $20^\circ\text{C}$ . In this instance  $s/2$  may be seen from Equation (12) to be about  $8 \times 10^{-6}$ . Consequently if terms of higher power than  $s^2$  are dropped in the series expansions of the exponential and integral, the errors introduced are of the order of 1 in  $10^{16}$  and 1 in  $10^{11}$  respectively. To a high degree of approximation, then



$$s \simeq \frac{Mc_0}{\rho} \cdot \frac{1 - s/2 + s^2/8}{1 - s/6} \simeq \frac{Mc_0}{\rho} \left/ \left( 1 + \frac{Mc_0}{2\rho} \right) \right.,$$

whence 
$$\beta \simeq 2D \frac{Mc_0}{\rho} \left/ \left( 1 + \frac{Mc_0}{2\rho} \right) \right.$$

The lowering of the liquid surface by evaporation is therefore described by

$$x_s = b - \sqrt{b^2 + \frac{2MDc_0t}{\rho \left( 1 + \frac{Mc_0}{2\rho} \right)}}, \quad (13)$$

and the rate of loss of mass per square centimeter of surface by

$$\frac{dm}{dt} = \frac{MDc_0}{b \left( 1 + \frac{Mc_0}{2\rho} \right)} \cdot \frac{1}{\sqrt{1 + \frac{2MDc_0t}{\rho b^2 \left( 1 + \frac{Mc_0}{2\rho} \right)}}}. \quad (14)$$

The vapor concentration in the space between the liquid surface and absorbing boundary as given by Equation (8) does not reduce to zero for  $t = 0$ ,  $b > x > 0$ . Hence, strictly speaking, Equations (8) to (14) apply to the process following a special initial vapor distribution.

The initial concentration assumed differs from the quasi-stationary state concentration by 0.03% at most at any point for water at 20°C. Thus effectively an initial concentration which is the quasi-stationary state concentration has been used and the subsequent evaporation with the corresponding movement of the boundary has then been taken into account.

In both the method of the quasi-stationary state and in our more rigorous method it is necessary to realize the following. If one starts with initial concentration in the space above the liquid equal to zero then: (a) If  $b \simeq 1$  meter, the rate of mass loss from the surface will be within 1% of the quasi-stationary state rate loss just short of 10 hr. (b) If  $b \simeq 4$  cm., the corresponding time is about one minute.

Treatment of the problem on the assumption of quasi-stationary states involves finding a solution of  $\partial^2 c / \partial x^2 = 0$  to satisfy the conditions  $c = 0$ ,  $x = b$ , and  $c_0 = c$ , at  $x_s$ . It leads to final equations,

$$x_s = 0$$

$$\frac{dm}{dt} = \frac{Mdc_0}{b}.$$

The latter differs from Equation (14) obtained in a more rigorous way by the factor  $1 / \left( 1 + \frac{Mc_0}{2\rho} \right)$  at  $t = 0$ . This factor differs from unity by only 9 parts

in a million for water with a surface temperature of 20°C. It is interesting to note that the method of quasi-stationary states cannot be applied if the absorbing boundary is at infinity, since it is impossible to obtain a solution of  $\partial^2 c / \partial x^2 = 0$  which satisfies  $c = 0$  at  $x \rightarrow \infty$  and  $c = c_0$  at  $x_s$ .

## 2. Evaporation from a Droplet

Let a droplet of volatile material be situated in a spherical air-filled enclosure of radius  $b$ , whose walls maintain zero vapor concentration at their surface. As evaporation proceeds, the radius of the drop decreases according to  $r_s = a(t)$ . For large drops (diameter of the order of 1 mm.) and air pressures of about 1 atm., little error is introduced by taking the vapor concentration  $c$  at  $r = r_s$  as equal to the saturation value at the temperature of the surface (1, 4). A solution of

$$D \partial^2 v / \partial r^2 = \partial v / \partial t$$

$$v = cr \quad (15)$$

is required to satisfy the conditions

$$r = a(t), v = c_0 a(t) \quad (16)$$

$$r = b, v = 0. \quad (17)$$

The initial distribution of vapor is left unspecified for the moment. The vapor flux equation is

$$MD(\partial c / \partial r)_{r=a(t)} = \rho da/dt. \quad (18)$$

The required solution may be obtained by an iteration process. Since conditions in the space are adjusted quickly to the changing drop size by diffusion, it is sufficient to assume that the solution of Equation (15) to a first approximation is that for a droplet of fixed size. If this solution is denoted by  $v_1$ , a second approximation solution  $v_2$  may be found from  $D \partial^2 v_2 / \partial r^2 = \partial v_1 / \partial t$ , and made to satisfy the boundary conditions. A third approximation  $v_3$  can be obtained from  $D \partial^2 v_3 / \partial r^2 = \partial v_2 / \partial t$  and adjusted to fit the boundary conditions and so on until the desired stage of approximation is reached. An equation describing the variation of droplet radius with time and so the rate of evaporation can then be found by inserting the solution in Equation (18).

The first approximation solution, disregarding changes in drop size as in the quasi-stationary state treatment (cf. ref. (2)), is

$$v_1 = ca(b - r)/(b - a),$$

whence

$$D \partial^2 v_2 / \partial r^2 = \partial v_1 / \partial t = cb(b - r)a'/(b - a)^2,$$

where  $a'$  has been written for  $da/dt$ . On integrating this expression twice, one obtains

$$v_2 = \frac{cba'}{D(b - a)^2} \left[ \frac{(b - r)^3}{3!} + f(t)(r - b) + g(t) \right],$$

where  $f(t)$  and  $g(t)$  are arbitrary functions to be adjusted to satisfy conditions (16) and (17). To do this

$$g(t) = 0$$

$$f(t) = (b - a) \left[ \frac{b - a}{6} - \frac{aD}{ba'} \right]$$

and the second approximation becomes,

$$v_2 = c_0 \frac{(b - r)}{(b - a)} \left[ 1 + \frac{ba'}{3!Da} \cdot \frac{(a - r)(2b - a - r)}{(b - a)} \right] \quad (19)$$

It follows from Equations (18) and (19) that

$$\begin{aligned} \frac{d}{dt}(a^2) &= \frac{-2DMc_0}{\rho} \cdot \frac{1}{(1 - a/b) \left( 1 + \frac{Mc_0}{3\rho} \frac{b}{a} \right)} \\ &= \left[ \frac{d}{dt}(a^2) \right]_s \cdot \frac{1}{\left( 1 + \frac{Mc_0}{3\rho} \frac{b}{a} \right)}, \end{aligned} \quad (20)$$

where the subscript  $s$  marks the value given by the quasi-stationary state treatment. The more rigorous treatment leads to the correction term  $1 / \left( 1 + \frac{Mc_0}{3\rho} \frac{b}{a} \right)$ . For water with a surface temperature of  $20^\circ\text{C}$ .,  $Mc_0/3\rho$  is about  $6 \times 10^{-6}$  so that the term differs from unity by less than 1% when  $b/a \leq 1700$ .

Equation (20) cannot be used when values of  $b/a$  are so large that  $\frac{Mc_0}{3\rho} \frac{b}{a}$  is more than a few per cent of unity, since it is inherent in the iteration method that the second approximation must not differ greatly from the first.

The formula which corresponds to Equation (20) for evaporation from a flat surface contains a factor  $\frac{1}{1 + \frac{Mc_0}{2\rho}}$ . Since it is derived from a rigorous

solution of the evaporation problem of the flat surface and since the correction term in Equation (20) is of similar form, one has increased confidence in the validity of the iteration method leading to Equation (20).

### References

1. BRADLEY, R. S., EVANS, M. G., and WHYTLAW-GRAY, R. Proc. Roy. Soc. (London), A, 186 : 368. 1946.
2. FUCHS, N. Physik Z. Sowjet Union. 6 : 225. 1934.
3. LANGMUIR, I. Phys. Rev. 12 : 368. 1918.
4. LANGSTROTH, G. O., DIEHL, C. H. H., and WINHOLD, E. J. Can. J. Research, A, 28 : 580. 1950.
5. ZENER, C. J. Applied Phys. 20 : 10. 1949.

## THE EVAPORATION OF DROPLETS IN STILL AIR

BY G. O. LANGSTROTH, C. H. H. DIEHL, AND E. J. WINHOLD

### Abstract

The evaporation of droplets of 1 to 2 mm. diameter into still air has been studied with nine liquids forming a series of graded volatility from toluene to aniline and including water. The experimental results agreed with calculations based on diffusion and heat transfer theory. The surface temperature of the more volatile droplets was found to be significantly lower than the bulk temperature, in contrast to Johnson's results for water. Convection effects were found to be present with 43 mm. diameter evaporation vessels in confirmation of Gilliland's suggestion, but were absent in the smaller vessels used in the main investigation.

The process of droplet evaporation is of interest in certain engineering, meteorological, and medical problems. There is reason to believe (8) that an understanding of the phenomenon in still air is basic to the more general problem of evaporation in moving air. This article describes a study of the evaporation of "large" droplets (diameter of the order of 1 mm.) in still air.

The original diffusion theory of droplet evaporation (16) has been elaborated by Fuchs (9) and certain features of importance for "small" droplets (diameter of the order of microns) have been worked out in detail by Bradley *et al.* (4). The theory has been developed on the assumption of quasi-stationary states but a more rigorous treatment involving solution of the diffusion equation with time variable boundary conditions leads to essentially the same final equations (17). A complete theory of evaporation involves consideration of heat as well as of mass transfer, since self-cooling is an important factor with the more volatile liquids.

Several experimental studies of the evaporation of "large" droplets in still air have been reported in the literature. Whytlaw-Gray and Patterson (24) observed a linear relation between the square of the drop diameter and time as required by theory, and Frössling (8) determined the slopes of such curves for three substances. Topley and Whytlaw-Gray (22) found that the diffusion coefficient of iodine vapor in air calculated from evaporation data differed by less than 5.2% from the values determined by another method, but it has been suggested (10) that convection may lead to spurious results in such experiments. Houghton's experiments with water (11) included only rough estimation of the temperature of the droplet and yielded a diffusion coefficient nearly 30% too low. Johnson has reported recently (14) that Fuchs' theory adequately describes the evaporation of water droplets if the droplet temperature is found from appropriate thermocouple measurements, but it seems likely that convection was present in his experiments, and the contribution of radiation exchange was disregarded in his calculations. Experiments with

<sup>1</sup> Manuscript received July 12, 1950.

Contribution from the Defence Research Board Experimental Station, Ralston, Alberta.

droplets in moving air (8) or in air at low pressure (4), and with "small" droplets (23, 25), lie outside the scope of this article.

It is significant that the most satisfactory results have been obtained with substances of relatively low vapor pressure (e.g., iodine). It seemed desirable to study the evaporation of droplets of more volatile liquids, with particular attention to the phenomenon of self-cooling and to the elimination of possible convection effects. To this end, experiments were performed with a graded series of nine liquids ranging in volatility from toluene to aniline and including water. Measurements were made of time changes in the diameter of droplets suspended from a thin glass fiber or fine thermocouple at the center of a spherical flask whose walls were coated with an absorber for the vapor. The data were interpreted with the aid of diffusion and heat transfer theory. Subsidiary experiments were performed to study possible convection effects.

### 1. Apparatus and Procedure

A drop of the liquid under investigation (diameter about 1.5 mm.) was suspended from the tip of a glass fiber (diameter about 100 microns) at the center of a spherical glass flask of 20 mm. internal diameter. The inner walls of the flask were coated with activated charcoal; for experiments with water the charcoal was dusted with phosphorus pentoxide. The coating was reactivated after each two or three experiments. The flask was immersed in a water bath at the desired temperature. Measurements of drop diameter were made at intervals with a microscope fitted with an ocular micrometer and sighted horizontally through small plane windows cemented to the water bath container and flask. The nature of the observations may be seen from Table II.

A parallel series of experiments was performed with the drop suspended from the tip of a #40 B. and S. gauge (diameter 0.080 mm.) copper-constantan thermocouple calibrated at the ice and steam points. The e.m.f. of the couple was read frequently (Table II) with a Leeds and Northrup type K-2 potentiometer. It was possible, with experience, to construct a thermojunction that did not seriously distort the suspended drop.

The evaporation of toluene (distilled over sodium), *n*-propyl alcohol (E. K. Co., White Label), glacial acetic acid (Gen. Chemical Co., Baher and Adamson quality), ethylbenzene (E. K. Co., White Label), *o*-chlorotoluene (E. K. Co., White Label), *n*-amyl alcohol (E. K. Co., Yellow Label), and aniline (E. K. Co., White Label), was studied at a bath temperature of 20°C. That of distilled water and *n*-butyl alcohol (E. K. Co., White Label) was studied in the region of 10°C., 20°C., and 40°C.

Certain details of the apparatus and procedure require special mention. Equalization of pressure in the evaporation flask with that outside was permitted by a small leak formed by cementing a narrow strip of thin paper along one side of the male portion of the ground glass joint supporting the glass

fiber or thermocouple. The usual thermostat controls were incorporated in the water bath but were not used during a run in order to avoid vibration; agitation was accomplished by an occasional gentle stir with a paddle. Because of the large capacity of the bath (13 gal.) the temperature change indicated by a mercury bath thermometer was not greater than  $0.3^{\circ}\text{C}$ . during an experiment, and commonly was undetectable. The optical micrometer was calibrated frequently under the conditions of the experiments by measurements on wires of known diameter inserted in place of the drop. One scale division corresponded to about 0.026 mm.

A careful comparison of evaporation data obtained in successive experiments without reactivation of the absorbing coat gave no indication of a loss of absorbing efficiency. As a further test, experiments with water were performed using a flask built up from brass sheet to have a corrugated surface of about three times the usual area. Since the determined evaporation rates were no larger than those obtained with the usual flask, the assumption that the coating maintained essentially zero vapor concentration at the flask walls appeared to be justified.

Two groups of experiments were performed to investigate the possible effects of convection, since it has been suggested (10) that it may lead to spurious results in this type of experiment. In the first, a comparison was made of evaporation rates obtained with a series of flasks of graded diameter (43 mm. to 15 mm.), on the ground that increased resistance to air motion with the smaller flasks should result in a lower evaporation rate if any convection effect was present. In the second, a comparison was made of the evaporation rates of drops suspended from a fine thermocouple and from a special thermocouple arrangement designed to conduct heat more rapidly to the drop. This was done on the ground that reduction of the temperature gradient in the flask should lessen temperature convection if any were present. The special thermocouple arrangement was made by soldering the #40 copper wire at 2 mm. above the junction to a tapered copper rod having a diameter of about 1 mm. at the lower end and about 6 mm. at the point of entrance to the chamber. With this arrangement, the bulk temperature of a water droplet was about  $5^{\circ}\text{C}$ . higher than with the usual couple (bath temperature  $20^{\circ}\text{C}$ ). The results of these experiments are given in Section 4 for water and *n*-butyl alcohol. They indicate that convection does occur in 43 mm. diameter flasks, but that its effect is negligibly small under the conditions of the main experiments.

## 2. Theoretical Considerations

Equations for the rate of evaporation of a droplet of radius  $a$ , mass  $m$ , and surface temperature  $T_a$ , located in air at  $P$  mm. of mercury pressure at the center of a spherical enclosure of radius  $b$  having walls at a temperature  $T_0$  capable of maintaining zero vapor concentration at their surface, are required for interpretation of the data. It is assumed that transfer of vapor occurs solely by diffusion, and that the method of quasi-stationary states is applicable in obtaining a solution (cf. 17).

## (a) Mass Transfer

Following Fuchs (9) one may write

$$dm/dt = 4\pi \int_{c_a}^0 dc \int_a^b dr/Dr^2, \quad (1)$$

where  $c$  and  $c_a$  denote the vapor concentrations at  $r$  and  $r = a$ , and  $D$  represents the appropriate value of the diffusion coefficient. It is well established (13, p. 62) that

$$1/D = 1/D_b \cdot (T_0/T)^\mu, \quad (2)$$

where  $D_b$  denotes the value of the diffusion coefficient at temperature  $T_0$  and air pressure  $P$ , and  $\mu$  is a constant. Furthermore, for a spherically symmetrical temperature distribution in the enclosure and a quasi-stationary state, it can be shown (9) that

$$dr/r^2 = \frac{b-a}{ab} \frac{dT}{T_0 - T_a}. \quad (3)$$

Integration of Equation (1) after changing the variable from  $r$  to  $T$  with the aid of Equations (2) and (3), and replacing  $c_a$  by  $pM/RT_a$ , leads to

$$-\frac{dm}{dt} = \frac{4\pi MD_b}{RT_0} \frac{ab}{b-a} p \frac{(\mu-1)\delta}{(1+\delta)^{\mu-1} - 1}, \quad (4)$$

where  $M$  denotes the molecular weight of the vapor,  $R$  the gas constant,  $p$  the pressure of vapor at the drop surface, and  $\delta$  has been written for  $(T_0 - T_a)/T_a$ . Equation (4) may be developed further by (a) expressing  $m$  in terms of the density  $\rho$  and the surface area  $S = 4\pi a^2$  of the drop, (b) expanding  $(1 + \delta)^{\mu-1}$  and disregarding terms of higher power than  $\delta^2$ , and (c) inserting Fuchs' multiplicative correction term  $(1 + p/2P)$  on the right hand side to take into account mass gradients in the air. The result is,

$$-\frac{dS}{dt} = \frac{8\pi MD_b}{\rho RT_0} \frac{b}{b-a} p \left(1 - \frac{\mu-2}{2}\delta\right) (1 + p/2P). \quad (5)$$

Neglect of the higher power terms in the expansion cannot introduce serious error under the conditions of our experiments; the error is less than 0.2% for water even if  $(T_0 - T_a) = 20^\circ\text{K}$  at  $T_a = 293^\circ\text{K}$ . The Fuchs correction term is a first order approximation, but this is sufficiently good for present purposes since the term seldom differed from unity by as much as 1%.

Under the conditions of our experiments  $p$  may be taken as equal to the saturated vapor pressure  $p_0$  at the temperature of the drop surface. This introduces little error, since, on kinetic theory reasoning (4),

$$\left. \begin{aligned} p &= p_0/[1 + (a + \lambda)D/a^2\nu a] \\ \nu &= \sqrt{RT_a/2\pi M} \end{aligned} \right\}, \quad (6)$$

where  $a$  denotes the evaporation coefficient and  $\lambda$  the mean free path of vapor molecules in air. Even for 1 mm. droplets of water, which has the remark-



ably low value  $\alpha = 0.04$  (1),  $p$  differs from  $p_0$  by less than 0.7% for the conditions studied.

Integration of Equation (5) yields,

$$\left. \begin{aligned} \sigma &= \sigma_0 - \frac{8\pi MD_b}{\rho RT_0} p \left( 1 - \frac{\mu - 2}{2} \delta \right) (1 + p/2P) \cdot t \\ \sigma &= 4\pi a^2 \left( 1 - \frac{2}{3} \frac{a}{b} \right) \end{aligned} \right\} \quad (7)$$

where  $\sigma_0$  denotes the value of  $\sigma$  at  $t = 0$ . According to this equation a plot of  $\sigma$  vs.  $t$  should be linear, but  $p$  cannot be specified unless the surface temperature of the drop is known.

#### (b) Heat Transfer

Assuming a spherically symmetrical temperature distribution and a quasi-stationary state, the rate of heat influx to the drop by conduction through the air is given by

$$H_c = 4\pi \int_{T_a}^{T_0} \frac{dT}{\int_a^b dr/kr^2}, \quad (8)$$

where  $k$  denotes the appropriate value of the thermal conductivity of air. Accepted data for  $k$  (13, p. 213) are well represented over the range 0°C. to 40°C. by

$$k = k_0(T/273)^n, \quad (9)$$

where  $k_0$  and  $n$  have the values given later. Integration of Equation (8) with the aid of Equations (3) and (9) and retention of first order terms in the expansion of  $(1 + \delta)^{n-1}$  leads to

$$H_c \rightarrow 4\pi k_b \frac{ab}{b-a} \cdot \frac{T_a}{T_0} (T_0 - T_a), \quad (10)$$

where  $k_b$  is the value of  $k$  at temperature  $T_0$ . The rate of heat influx through a 100 micron diameter glass fiber as used in our experiments may be disregarded since it can be shown to be less than 0.5% of that through the air even when a 25°C. temperature difference exists between the ends of the fiber.

The rate of heat influx by radiation exchange cannot be calculated accurately since emission coefficient data are not available. Fortunately this mechanism accounts for less than 1/7 of the total influx, and assumption of black body characteristics for the drop and chamber walls can hardly introduce large errors in calculated results. On this basis the rate of heat influx by radiation exchange is

$$H_r \rightarrow 4\pi a^2 \epsilon (T_0^4 - T_a^4), \quad (11)$$

where  $\epsilon$  denotes the Stefan-Boltzmann radiation constant.



The rate of heat loss is  $L.dm/dt$ , where  $L$  denotes the latent heat of vaporization at the temperature  $T_a$  and  $dm/dt$  may be found from Equation (5). Equating rates of heat influx and loss and rearranging, one obtains,

$$\left. \begin{aligned} (T_0 - T_a) &\rightarrow \frac{MD_b L p}{R k_b T_a} \left( 1 - \frac{\mu - 2}{2} \delta \right) (1 + p/2P)/(1 + \phi) \\ \phi &= \frac{\epsilon}{k_b} \frac{a(b-a)}{b} \frac{T_0}{T_a} \frac{T_0^4 - T_a^4}{T_0 - T_a} \end{aligned} \right\} \quad (12)$$

The surface temperature  $T_a$  may be estimated from this equation if  $T_0$  and the characteristics of the substance are known.

### 3. Notes on the Application of the Theory

#### (a) Characteristics of the Test Substances

Some basic data for the substances studied are given in Table I and the notes that follow. In making estimates, the gas constant  $R$  and the Stefan-Boltzmann constant  $\epsilon$  were taken respectively as  $8.31 \times 10^7$  ergs per mole per  $^\circ\text{K}$ . and  $1.37 \times 10^{-12}$  cal. per  $\text{cm}^2$  per sec. per  $^\circ\text{K}^4$ ;  $k_b$  and  $n$  of Equation (9) had values of  $5.34 \times 10^{-5}$  cal. per cm. per sec. per  $^\circ\text{C}$ . and 0.813 respectively.

**Density.**—The temperature dependence of density as given in Table I was disregarded in making estimates. This procedure could introduce errors of only 0.3% and 0.9% in the extreme cases of water and *n*-butyl alcohol at a bath temperature of  $10^\circ\text{C}$ . Data for ethylbenzene, *o*-chlorotoluene, and *n*-amyl alcohol were taken respectively from references (19), (3), and (2). International Critical Tables values were used for water (12, p. 24) and the other liquids (12, p. 28).

**Diffusion coefficient.**—This quantity, which varies inversely as the air pressure (13, p. 62), is specified by stating its value for air at N.T.P. together with the temperature coefficient, i.e., by stating  $D_0$  and  $\mu$ . These constants were

TABLE I  
CONSTANTS FOR THE SUBSTANCES STUDIED

Substance	<i>M</i> , gm.	$\rho$ , gm./ml.		$D_0$ , cm. <sup>2</sup> /sec.	$\mu$	Vapor pressure at $20^\circ\text{C}$ ., mm. of Hg	$L$ at $20^\circ\text{C}$ ., cal./gm.
		Value used	% change per $^\circ\text{C}$ .				
Toluene	$\text{C}_7\text{H}_8$	92.1	0.875	0.104	0.0709	2.00	102
Water	$\text{H}_2\text{O}$	18.0	0.999	0.020	0.219	1.853	586
<i>n</i> -Propyl alcohol	$\text{C}_3\text{H}_8\text{O}$	60.1	0.819	0.0073	0.085	2.00	175
Acetic acid	$\text{C}_2\text{H}_4\text{O}_2$	60.1	1.052	0.105	0.1064	2.00	158
Ethylbenzene	$\text{C}_8\text{H}_{10}$	106.2	0.872	0.092	0.0658	1.75	89
<i>n</i> -Butyl alcohol	$\text{C}_4\text{H}_{10}\text{O}$	74.1	0.810	0.086	0.0703	2.00	180
<i>o</i> -Chlorotoluene	$\text{C}_7\text{H}_7\text{Cl}$	126.6	1.086	0.065	0.059	2.00	81
<i>n</i> -Amyl alcohol	$\text{C}_5\text{H}_{12}\text{O}$	88.3	0.818	0.073	0.0589	2.00	155
Aniline	$\text{C}_6\text{H}_7\text{N}$	93.1	1.022	0.083	0.0695	2.00	162

taken from the International Critical Tables (13, p. 62) for all vapors except water; correction of a misprint was necessary in the data for aniline. Trautz and Müller's values as given by Dorsey (7) were used for water. These data for water agree well between 0°C. and 40°C. with I.C.T. data (13, p. 62) and with some measurements by Gilliland (10); they are about 4% higher than Brookfield's values (5) and about 2% lower than some results quoted by Montgomery (18). The I.C.T. data for *n*-butyl alcohol and toluene agree with Gilliland's determinations in the range of interest; those for *n*-butyl alcohol and acetic acid agree with some values given in the Smithsonian Physical Tables (20).

*Vapor pressure.*—Data for water and *n*-propyl alcohol were taken from reference (12) (pp. 210, 217), for *n*-butyl alcohol from references (15) and (6), and for the other liquids from Stull's compilation (21). Extrapolation was necessary below 15°C. in the *n*-butyl alcohol curve, and below 34.8°C. in the aniline curve. I.C.T. data for toluene and acetic acid agree closely with Stull's near 20°C.; they are about 2% higher than Stull's for *n*-propyl alcohol, nearly 70% higher for *n*-amyl alcohol, and more than twice as great for ethylbenzene. Use of the I.C.T. data for *n*-amyl alcohol and ethylbenzene led to impossible conclusions. I.C.T. data for aniline do not extend much below 60°C. where they are in agreement with Stull's. The vapor pressure curve used for *n*-butyl alcohol agreed with I.C.T. data but was about 14% lower than Stull's curve at 20°C.

*Latent heat of vaporization.*—I.C.T. data (13, p. 138) were used for water. Values for the other substances were estimated in calories per gram from the modified Clapeyron-Clausius equation

$$L \rightarrow 1.98 T^2 / Mp \cdot dp/dt. \quad (13)$$

Values of  $1/p \cdot dp/dt$  appropriate to the temperatures in the experiments were found from the vapor pressure curves referred to above.

#### (b) Application of the Equations

In order to provide an over-all check of the theory, the slope of experimental  $\sigma$  vs.  $t$  curves was compared with  $d\sigma/dt$  as calculated from Equations (7) and (12). In making the calculation,  $T_a$  was found from Equation (12), and the corresponding value of  $p$  was inserted in the expression constituting the coefficient of  $t$  in Equation (7). The comparison was made only with data for droplets suspended from a glass fiber.

The small correction term  $\left(1 - \frac{\mu - 2}{2} \delta\right) (1 + p/2P)$  presented no difficulty in handling Equations (7) and (12). It differed from unity by less than 1% for the most volatile substance (toluene) at 20°C., and by less than 1.5% in the extreme case of water at 20°C. Solution of Equation (12) for  $T_a$  was made by an indirect procedure. It involved solution for the  $T_0$  values corresponding to various selected  $T_a$  values and construction of  $T_a$  vs.  $T_0$  curves from

which the required  $T_a$  values could be read. Solution for  $T_0$  was made by successive approximations, disregarding the contribution of radiation exchange (i.e.  $\phi = 0$ ) in the first. Although  $\phi$  depends on drop diameter, estimates were made for a mean midpoint diameter of 1.40 mm. As shown from examination of all drop sizes in the experiments, this simplification led to no very serious errors. Taking deviations from 1.40 mm. into account could change estimated  $T_a$  values by less than 0.9°C. for water at  $T_0 = 40^\circ\text{C}$ ., by less than 0.2°C. for water at 10°C. or 20°C. or acetic acid at 20°C., and by less than 0.1°C. for the other substances and conditions.

Since self-cooling is an important factor in the evaporation of volatile droplets, a knowledge of the surface temperatures attained is of special interest. A value for  $T_a$  may be found by equating the coefficient of  $t$  in Equation (7) to the slope of the experimental  $\sigma$  vs.  $t$  curve, solving for  $p$ , and finding the corresponding temperature from vapor pressure data. Another value may be found directly from Equation (12). The first value depends only on diffusion theory and observed data. Although the second depends in part on the diffusion theory it is based primarily on heat transfer considerations. Agreement between the two values is evidence of their reality.

#### 4. Experimental Results

Data for a typical experiment are given in Table II. The linearity of  $\sigma$  vs.  $t$  curves is illustrated by several examples plotted in Fig. 1.

The dependence of the slope of  $\sigma$  vs.  $t$  curves on bath temperature is shown in Figs. 2 (water) and 3 (*n*-butyl alcohol). All  $d\sigma/dt$  values have been corrected to an air pressure of 690 mm. of mercury by application of the multiplicative

TABLE II  
TYPICAL DATA FOR AN EXPERIMENT

Experiment 52B: Water drop on fine thermocouple; internal diam. flask, 20 mm.  
Bath temperature; initial, 22.2°C.; final, 22.2°C.; Mean  $T_0 = 22.2^\circ\text{C}$ .  
Barometric pressure: 681 mm. of mercury.

Time,* sec.	Thermocouple reading, °C.	Time*, sec.	Drop diam., mm.	$\sigma \times 10^5$ , cm <sup>2</sup> .
33	12.8	68	1.62	7.80
108	12.7	160	1.56	7.28
184	12.7	196	1.55	7.13
245	12.9	262	1.50	6.71
324	13.0	337	1.44	6.20
397	13.1	411	1.39	5.79
465	13.1	479	1.34	5.40
526	13.2	541	1.29	5.02
591	13.4	607	1.24	4.65
656	13.5	671	1.18	4.21
715	13.5	731	1.13	3.87
763	13.7	778	1.08	3.55

\*The moment of insertion of the drop into the evaporation vessel was taken as zero time.  
Thermojunction temperature at the midpoint of the experiment =  $T_c = 13.1^\circ\text{C}$ .

factor  $P/690$ . The pressures ranged from 681 to 705 mm. of mercury and the correction never exceeded 2% for water and 1.3% for *n*-butyl alcohol; it was usually less than 1%. The results of experiments with different sized flasks and with the special thermocouple arrangement, performed in the study of convection, are included in the figures.

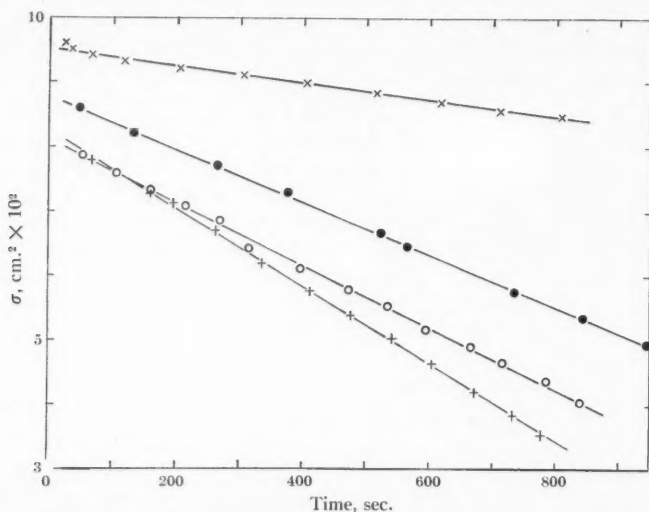


FIG. 1. Typical experimental curves obtained with a flask of 20 mm. diameter. The symbols have the following significance; +, water, fine thermocouple,  $T_0 = 22.2^\circ\text{C}$ .,  $P = 681$  mm. of mercury; ○, water, glass suspension,  $T_0 = 22.6^\circ\text{C}$ .,  $P = 696$  mm. of mercury; ●, *n*-butyl alcohol, glass suspension,  $T_0 = 20.2^\circ\text{C}$ .,  $P = 684$  mm. of mercury; X, aniline, glass suspension,  $T_0 = 19.9^\circ\text{C}$ .,  $P = 689$  mm. of mercury. Abscissas should be multiplied by 3 for the aniline curve. Values of  $d\sigma/dt \times 10^5$  cm<sup>2</sup>. per sec. as found from the slopes of these curves are respectively 6.08, 4.90, 4.05, and 0.37.

Average  $d\sigma/dt$  values for all substances at a bath temperature of  $20^\circ\text{C}$ . are given in Table III (20 mm. diameter flask) along with the theoretical values calculated from Equations (7) and (12). Individual observed values were corrected to a barometric pressure of 690 mm. of mercury as described above. Some of the data required a further correction, found from the theoretical  $d\sigma/dt$  vs.  $T_0$  curves, to bring them to the standard bath temperature of  $20^\circ\text{C}$ . Differences from this temperature were not more than  $0.2^\circ\text{C}$ ., except for one experiment with *o*-chlorotoluene ( $0.3^\circ\text{C}$ .), two with ethylbenzene ( $0.3^\circ\text{C}$ . and  $0.5^\circ\text{C}$ .), and all with acetic acid. Three experiments with acetic acid on a glass fiber were performed at a bath temperature of  $19.2^\circ\text{C}$ ., and three with it between  $22.3^\circ\text{C}$ . and  $22.7^\circ\text{C}$ .; bath temperatures in experiments with the thermocouple suspension were between  $20.8^\circ\text{C}$ . and  $21.0^\circ\text{C}$ . for this substance. The total correction applied to individual values is indicated by the maximum and minimum figures included in the table. It exceeded 3% only for the

acetic acid results, and since half of these were associated with a lower and half with a higher bath temperature than 20°C. there was a partial compensation for any error in the correction factor in averaging the glass fiber data. The deviations of corrected  $d\sigma/dt$  values from the mean for each group are also indicated in the table. Over all experiments, the average deviation of individual values from the mean was 1.9%.

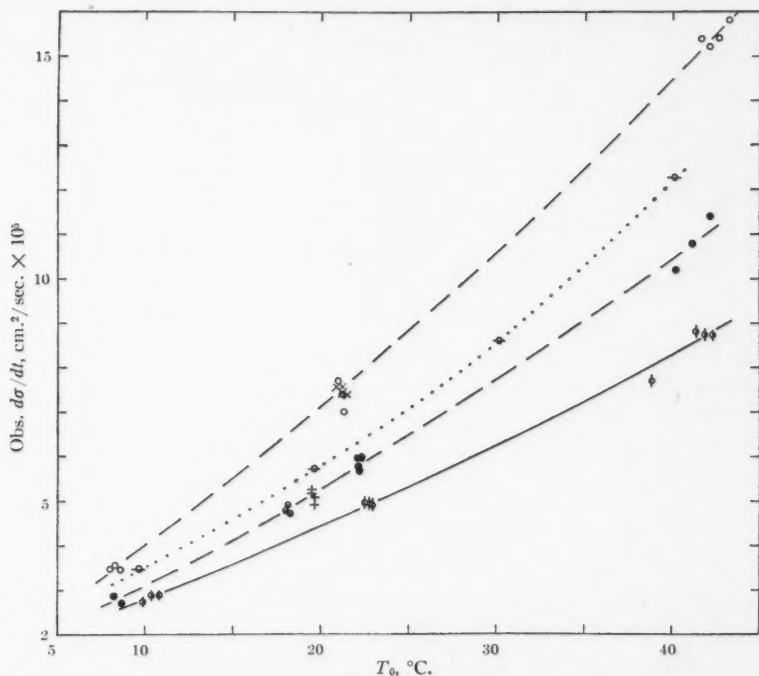


FIG. 2. Observed  $d\sigma/dt$  values for water droplets at various bath temperatures. The symbols are associated with the following experimental conditions;  $\phi$ , glass suspension, 20 mm. flask;  $\ominus$ ,  $\bullet$ ,  $\cdot$ ,  $+$ , fine thermocouple suspension, flasks of 43, 31, 20, and 15 mm. diameter respectively;  $\times$ ,  $\circ$ , special thermocouple suspension, flasks of 43 and 20 mm. diameter respectively. The plotted values were obtained in single experiments except for those represented by  $\ominus$ , which are average values for several experiments.

Table III includes surface temperatures of droplets as estimated from heat transfer equation (12) and from application of diffusion theory equation (7) to observed  $d\sigma/dt$  data. Surface temperatures calculated by the latter method, and the bulk temperature  $T_c$  as indicated by the thermocouple, are also given for experiments in which a thermocouple suspension was used. The  $T_c$  values are averages without any attempt at correction. They may be compared with the surface temperatures, however, since the departures from the standard air pressure and bath temperature were usually small in individual ex-

periments, and occurred in different directions within a group. This statement finds support from a comparison of  $T_c$  with  $T_a$  estimated for the actual conditions of each experiment. For water and *n*-butyl alcohol,  $T_c$  was read directly from  $T_c$  vs.  $T_0$  plots of observed data.

Table IV contains similar data to Table III for water and *n*-butyl alcohol at bath temperatures of 10°C. and 40°C. Observed  $d\sigma/dt$  values for all substances

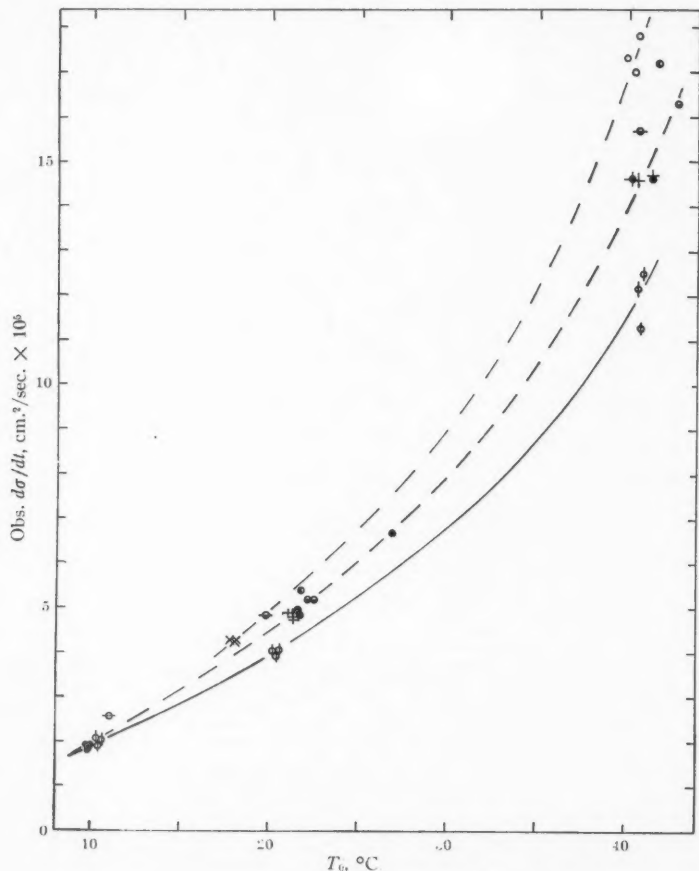


FIG. 3. Observed  $d\sigma/dt$  values for *n*-butyl alcohol droplets at various bath temperatures. The symbols are associated with the following experimental conditions; ●, ◐, glass suspension, flasks of 43 and 20 mm. diameter respectively; ◐, ◐, ◐, +, fine thermocouple suspension, flasks of 43, 26, 20, and 14.5 mm. diameter respectively; ×, ◐, special thermocouple suspension, flasks of 43 and 20 mm. diameter respectively. Plotted values were obtained in single experiments except for those denoted by ◐ and ◐, which are averages for several experiments.

and conditions have been plotted against the theoretical values in Fig. 4 to show in a convenient way the nature of the agreement over a wide range. The relation between the surface and bulk temperatures for all substances and conditions is indicated in Fig. 5.

TABLE III

COMPARISON OF AVERAGE EXPERIMENTAL DATA AT  $T_0 = 20^\circ\text{C}$ . WITH THEORY; SURFACE AND BULK TEMPERATURES

Drop	Av. mid-point diam., mm.	Suspension	No. of expts.	Obs. $d\sigma/dt$ , $\text{cm}^2/\text{sec.} \times 10^5$						Calc. $d\sigma/dt$ , $\text{cm}^2/\text{sec.} \times 10^5$	Est. $T_a$ ( $^{\circ}\text{C}.$ )		Mn. obs., $T_c$ , $^{\circ}\text{C}.$
				% Correction		% Dev. from Mn.		Mean value	Heat†		Evap.‡		
				Min.	Max.	Max.	Av.						
Toluene	1.47	G	3	0.6	1.2	2.4	1.4	17.4	17.2	11.0	11.4	—	
	1.40	TC	4	0.9	1.0	1.9	0.7	21.3	—	—	14.6	14.4	
Water*	1.28	G	—	—	—	—	—	4.4	4.3	4.1	4.9	—	
	1.47	TC	—	—	—	—	—	5.3	—	—	7.4	11.1	
	1.30	STC	—	—	—	—	—	7.1	—	—	11.8	16.2	
<i>n</i> -Propyl alc.	1.43	G	3	2.0	2.1	0.7	0.4	8.4	9.4	12.2	10.9	—	
	1.46	TC	3	1.0	1.0	2.2	2.1	9.2	—	—	12.2	15.2	
Acetic acid	1.18	G	6	2.5	11.4	9.7	4.2	7.8	7.8	12.3	12.4	—	
	1.40	TC	3	5.2	6.7	2.0	1.3	8.7	—	—	14.2	17.5	
Ethylbenzene	1.41	G	4	0.1	2.7	2.4	2.2	7.2	7.9	16.0	14.7	—	
	1.47	TC	3	0.4	0.4	0.9	0.5	7.8	—	—	16.0	18.0	
<i>n</i> -Butyl alc.*	1.45	G	—	—	—	—	—	3.9	3.9	16.8	17.1	—	
	1.58	TC	—	—	—	—	—	4.5	—	—	17.3	18.8	
<i>o</i> -Chlorotoluene	1.44	G	3	0.4	1.1	1.1	0.9	2.7	3.0	18.3	17.3	—	
	1.52	TC	3	0.4	1.9	4.0	2.6	2.7	—	—	17.6	19.3	
<i>n</i> -Amyl alc.	1.52	G	3	1.2	1.8	4.2	3.0	1.63	1.70	18.7	18.2	—	
	1.59	TC	3	0.6	1.3	1.9	1.2	1.60	—	—	18.0	18.5	
Aniline	1.84	G	3	0.5	1.7	2.1	1.5	0.37	0.33	19.7	21.2	—	
	1.95	TC	3	0.6	2.8	4.2	2.9	0.36	—	—	20.5	19.8	

\* $d\sigma/dt$  values read from the curves of Fig. 2 or Fig. 3.

†The average of the drop diameters at the midpoint of each experiment.

‡Equation (12).

§Equation (7) and observed  $d\sigma/dt$  data.

G, T, and STC denote respectively that the drops were suspended from a glass fiber, a fine thermocouple or the special thermocouple arrangement.

TABLE IV

COMPARISON OF AVERAGE EXPERIMENTAL DATA AT  $T_0 = 10^\circ\text{C}$ . AND  $T_0 = 40^\circ\text{C}$ . WITH THEORY SURFACE AND BULK TEMPERATURES

Drop	Av. mid-point diam., mm.	Suspension	$T_0$ , $^\circ\text{C}$ .	$d\sigma/dt$ $\text{cm}^2/\text{sec.} \times 10^5$		Est. $T_a$ $^\circ\text{C}$ .		Mn. obs., $T_c$ , $^\circ\text{C}$ .
				Obs. Mn.	Calc.	Heat	Evap.	
Water	1.21	G	10.0	2.7 <sub>9</sub>	2.8 <sub>5</sub>	-0.9	-1.2	—
	1.63	TC	10.0	3.1 <sub>2</sub>	—	—	0.4	3.9
	1.37	STC	10.0	4.0 <sub>1</sub>	—	—	3.9	7.7
	1.07	G	40.0	8.3	7.9	12.3	13.1	—
	1.50	TC	40.0	10.4	—	—	16.6	24.8
	1.18	STC	40.0	14.5	—	—	21.9	31.0
n-Butyl alc.	1.54	G	10.0	1.9 <sub>0</sub>	1.84	8.2	8.7	—
	1.52	TC	10.0	1.9 <sub>4</sub>	—	—	8.9	9.0
	1.49	G	40.0	11.6	12.3	31.0	30.5	—
	1.49	TC	40.0	14.0	—	—	33.0	32.1
	1.39	STC	40.0	17.0	—	—	35.9	36.1

See footnotes to Table III.



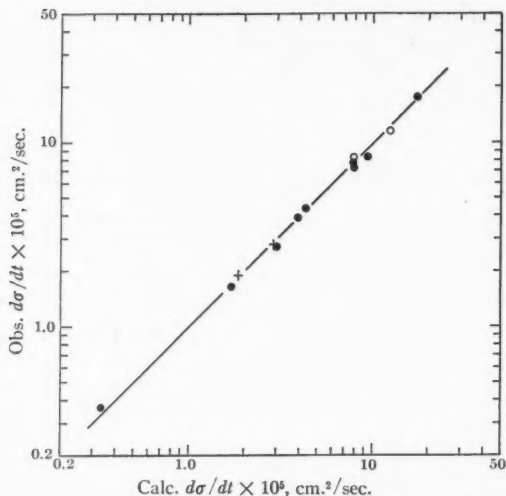


FIG. 4. Comparison of experimental and theoretical  $d\sigma/dt$  values. The straight line is associated with perfect agreement. Data for bath temperatures of  $10^{\circ}\text{C}$ .,  $20^{\circ}\text{C}$ ., and  $40^{\circ}\text{C}$ . are denoted respectively by +,  $\bullet$ , and  $\circ$ . The points in order of increasing abscissa value refer to aniline, *n*-amyl alcohol, *n*-butyl alcohol, water, *o*-chlorotoluene, *n*-butyl alcohol, water, acetic acid, water, ethylbenzene, *n*-propyl alcohol, *n*-butyl alcohol, and toluene.

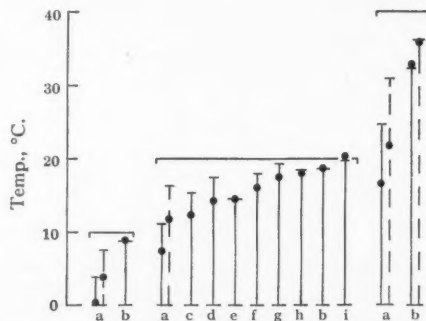


FIG. 5. A comparison of surface and bulk (thermocouple) temperatures. Data obtained with the fine and with the special thermocouple are denoted respectively by solid and dashed lines. The surface and bulk temperatures have ordinates represented respectively by disks and short horizontal lines. The data are grouped according to bath temperature, which is indicated by the long horizontal lines. The letters refer to substances, i.e., a, water; b, *n*-butyl alcohol; c, *n*-propyl alcohol; d, acetic acid; e, toluene; f, ethylbenzene; g, *o*-chlorotoluene; h, *n*-amyl alcohol; and i, aniline.

## 5. Discussion

As illustrated in Fig. 1, plots of  $\sigma$  vs.  $t$  were straight lines in accordance with theory. No difference was detectable in the slope of the lines for water droplets suspended from a fine thermocouple when 15, 20, and 31 mm. diameter

flasks were used, but the slope was from 13% to 22% greater on using a 43 mm. diameter flask (Fig. 2). This circumstance is attributed to the occurrence in the large flask of convective air motion which was prevented in the smaller flasks by increased resistance to convection. This view is supported by the fact that with the large flask (a) the measurements exhibited considerably greater scatter, and (b) the couple registered temperatures from 1.2°C. to 5°C. lower, which would be associated with a smaller rather than a larger evaporation rate in the absence of convection but which is to be expected in its presence. Further support is provided by the fact that results obtained with 20 and 43 mm. flasks were in agreement when the drop was suspended from the special rather than from the fine couple (Fig 2). The special couple reduced the self-cooling (Tables III and IV) and so decreased the tendency toward convection. Similar conclusions are reached from examination of the *n*-butyl alcohol data (Fig. 3). On this basis it was considered that convection was negligible in a flask of 20 mm. diameter, and this size was adopted for the main experiments discussed below.

When observed  $d\sigma/dt$  values for droplets suspended from a glass fiber were plotted against the theoretically expected values as in Fig. 4, the points fell quite closely along the 45° line indicative of agreement, though the range of variation of the plotted quantity was large (1:60). The greatest deviation was about 12% for *n*-propyl alcohol. Such deviations in individual substances are to be expected since the calculated values depend on available diffusion coefficient and vapor pressure data. The difficulty of obtaining high reliability in the former is well known (10), and the latter appear to be somewhat uncertain at pressures of a few millimeters of mercury (Section 3). As may be seen from Tables III and IV, the average deviation of observed from calculated  $d\sigma/dt$  values was 5.6%. The theory as outlined in Section 2 appears to be adequate.

Surface temperatures of droplets as estimated from heat transfer theory agreed on the average to within 0.7°C. with values found by application of diffusion theory to evaporation data. It may be seen from Tables III and IV that the difference never exceeded 1.5°C. The agreement is satisfactory in view of the uncertainties in diffusion coefficient and vapor pressure data, and indicates that the values found are real.

The agreement between theory and experiment for data obtained with droplets on a glass fiber suspension justifies the application of diffusion theory to evaporation data to calculate the surface temperature of droplets suspended from a thermocouple. Differences were found between the temperature so calculated and the reading of the couple (Tables III and IV). For water droplets, they ranged from 3.5°C. to 8.2°C. depending on bath temperature. As may be seen from Fig. 5 the difference became progressively less with decreasing volatility of the liquid, and the two temperatures were indistinguishable for such liquids as *n*-amyl alcohol and aniline. Why they should be indistinguishable for the relatively volatile toluene is not clear. The data suggest

that an evaporating droplet consists of a sphere of liquid in convective motion and nearly uniform in temperature throughout, surrounded by a thin, relatively fixed layer of liquid at a lower temperature (cf. (26)). The internal motions are readily observable on introducing dust particles into a drop. The couple reading corresponded to the internal temperature, and the calculated value to the temperature of the surface layer from which evaporation takes place.

A material difference between the surface and internal temperature of water droplets is contrary to the conclusions of Johnson (14) who considered that the surface temperature was essentially that which would be indicated by a suspending couple of negligible heat conductivity. His experiments were performed in an atmosphere containing water vapor, and although details of his evaporation chamber are not available it was probably large in order to minimize humidity changes caused by vapor from the drop. If so, convection was probably present. As pointed out in the first paragraph of the discussion, the presence of convection is associated with an increased rate of evaporation and a decreased internal temperature of the droplet. Insertion of the former quantity in Fuchs' equation therefore yields an apparent surface temperature higher than normal while the bulk temperature is lower.

It is considered that these studies establish the procedure of estimating droplet evaporation in still air from diffusion and heat transfer theory. In addition, the experimental method may be used to determine diffusion coefficients of various vapors in air. For liquids of low volatility (e.g., aniline), the temperature of a suspending thermocouple may be taken as the temperature of the evaporation surface without introducing serious error.

### References

1. ALTY, T. and MACKAY, C. A. *Proc. Roy. Soc. (London)*, A, 149 : 104. 1935.
2. BEILSTEINS HANDBUCH DER ORGANISCHEN CHEMIE. Vol. 1. Verlag von Julius Springer, Berlin. 1930. p. 383.
3. BEILSTEINS HANDBUCH DER ORGANISCHEN CHEMIE. Vol. 5. Verlag von Julius Springer, Berlin. 1930. p. 291.
4. BRADLEY, R. S., EVANS, M. G., and WHYTE-LAW-GRAY, R. *Proc. Roy. Soc. (London)*, A, 186 : 368. 1946.
5. BROOKFIELD, K. J., FITZPATRICK, H. D. N., JACKSON, J. F., MATTHEWS, J. B., and MOELWYN-HUGHES, E. A. *Proc. Roy. Soc. (London)*, A, 190 : 59. 1947.
6. BUTLER, J. A. V., RAMCHANDANI, C. N., and THOMSON, D. W. *J. Chem. Soc.* 138 : 280. 1935.
7. DORSEY, N. E. *Properties of ordinary water substance*. Reinhold Publishing Corp. New York. 1940. p. 73.
8. FRÖSSLING, N. *Gerlands Beitr. Geophys.* 52 : 170. 1938.
9. FUCHS, N. *Physik. Z. Sowjetunion*, 6 : 225. 1934.
10. GILLILAND, E. R. *Ind. Eng. Chem.* 26 : 681. 1934.
11. HOUGHTON, H. G. *Physics*, 4 : 419. 1933.
12. INTERNATIONAL CRITICAL TABLES. Vol. 3. McGraw-Hill Book Company, Inc., New York. 1928.
13. INTERNATIONAL CRITICAL TABLES. Vol. 5. McGraw-Hill Book Company, Inc., New York. 1929.
14. JOHNSON, J. C. *J. Applied Phys.* 21 : 22. 1950.
15. KAHLBAUM, G. W. A. *Z. physik. Chem.* 26 : 577. 1898.
16. LANGMUIR, I. *Phys. Rev.* 12 : 368. 1918.
17. LUCHAK, G. and LANGSTROTH, G. O. *Can. J. Research*, A, 28 : 574. 1950.
18. MONTGOMERY, R. B. *J. Meteorol.* 4 : 193. 1947.
19. PERKIN, W. H. *J. Chem. Soc.* 69 : 1025. 1896.

20. SMITHSONIAN PHYSICAL TABLES. Smithsonian Institute, Washington. 1934. p. 216.
21. STULL, D. R. *Ind. Eng. Chem.* 39 : 517. 1947.
22. TOPLEY, B. and WHYTLAW-GRAY, R. *Phil. Mag.* 4 : 873. 1927.
23. TWORT, C. C., BAKER, A. H., FINN, S. R., and POWELL, E. O. *J. Hyg.* 40:254. 1940.
24. WHYTLAW-GRAY, R., and PATTERSON, H. S. *Smoke*. Edward Arnold and Co., London. 1932. p. 168 ff.
25. WOODLAND, D. J. and MACK, E. *J. Am. Chem. Soc.* 55 : 3149. 1933.
26. WYLLIE, G. *Proc. Roy. Soc. (London), A*, 197 : 383. 1949.

## THE THERMAL CONDUCTIVITY OF ELASTOMERS UNDER STRETCH AND AT LOW TEMPERATURES<sup>1</sup>

BY T. M. DAUPHINEE, D. G. IVEY,<sup>2</sup> AND H. D. SMITH<sup>3</sup>

### Abstract

Heat conductivity of natural rubber and GR-S was studied in the range from +50°C. to -170°C. and from 0 to 100% stretch. The apparatus used was a greatly modified version of one designed by Schallamach. The conductivity of both types of rubber at 0% stretch lies in the range between  $3.5 \times 10^{-4}$  and  $4.0 \times 10^{-4}$  cal./sec. cm. deg. C. Stretching increases the rate of change of conductivity with temperature of both natural rubber and GR-S, and decreases the conductivity of the latter. On lowering the temperature and raising it again natural rubber exhibits a complicated hysteresis phenomenon, while GR-S shows a hysteresis loop caused by a second order transition near the brittle point. The hysteresis phenomena of both types of rubber near the second order transition temperature shows considerable similarity to the changes in specific heat observed by Bekkedahl and coworkers. Above and below the transition region the heat conductivity decreases approximately linearly with temperature as might be expected from classical theory. The variation through the second order transition does not agree with classical theory, but may be explained qualitatively on the basis of a diffuse lambda type transition.

### Introduction

The variation of thermal conductivity of elastomers with stretch and temperature is a subject that has received surprisingly little theoretical or experimental consideration. This has been due partly to the necessity of concentration on production in quantity and the development of the immediately useful primary characteristics such as stretch, wear resistance, and strength, and partly to the fact that the measurement of conductivity is often a difficult and time consuming process.

The range of temperatures between -160°C. and +40°C. is a particularly interesting one, for within it many of the high polymers exhibit first and second order transitions. Information concerning these transitions has been derived from studies of various physical properties such as specific heat, volume and linear expansions, crystal structure, modulus of elasticity, hardness, compressibility, and dielectric constant. However, the exact nature of the transitions is not yet completely understood. In fact the theory generally of the physics of high polymers is in a state of flux. Practically the only part that has received treatment sufficiently complete to give quantitative results is that dealing with stress-strain relationships.

The retardation in the development of the theory of elastomers is due to a large extent to the dearth of experimental data upon which theory could be based and by which it could be checked. Data of any kind on the variation of

<sup>1</sup> Manuscript received July 5, 1950.

Contribution from the Department of Physics, University of British Columbia, Vancouver, British Columbia.

<sup>2</sup> Present address: University of Toronto, Toronto, Ont.

<sup>3</sup> Now, President, Nova Scotia Research Foundation, Halifax, N.S.

thermal conductivity with temperature have been noticeably lacking. In order to obtain more complete data a series of investigations was carried out on the thermal conductivity of natural rubber and GR-S over a wide range of temperatures for various degrees of stretch.

### The Method of the Experiment

Two sets of apparatus were used during the course of the experiments, both embodying the same fundamental principles of measurement. The work on natural rubber was done in a sandwich type apparatus with measurable heat source in the center and with the heat flowing outward through two identical samples of rubber to heat sinks on the outside. The apparatus is similar in principle to that of Schallamach (7) but with considerable revision to permit the study of stretched as well as unstretched rubber. This type of apparatus has an advantage in that it automatically provides some radiation shielding, but has the disadvantage that it is necessary to have both samples in the same state when a measurement is being made, a condition not always obtainable with some elastomers. Consequently, the measurements on GR-S were made using an apparatus with two measurable heat sources on the outside and with the heat flow inwards through two different samples to a heat sink in the center. With this apparatus it was possible to study two samples simultaneously and to eliminate the danger of faulty readings caused by different transition temperatures, unequal time lag, unequal aging, etc. In both cases a guard is placed on each side of the measuring unit to prevent conduction along the sample. The method of determining the conductivity is the same for both, namely, by means of a measurement of the electrical energy required to maintain a given temperature gradient across a known area of the sample.

The conductivity may be determined from this type of apparatus from the formula

$$K_T = \frac{Q}{J} \cdot \frac{d}{A} \cdot \frac{1}{T_2 - T_1}, \quad (1)$$

where

$K_T$  = thermal conductivity at temperature  $T$ ,

$Q$  = heat input in watts,

$J$  = electrical equivalent of heat,

$d$  = average thickness of samples,

$A$  = effective area of measuring unit,

$T_2 - T_1$  = temperature difference across the samples,

$T = \frac{T_2 + T_1}{2}$  = average temperature.

### Description of Apparatus

The second apparatus only will be described in detail, mention being made of the points of difference between it and the first.

Schematic diagrams of the second apparatus used are shown in Figs. 1 and 2. The main measuring blocks (*a*), which were made of copper, were heated by manganin elements threaded through equally spaced holes (*b*), in such a way that heating would be uniform throughout. The main heating blocks were held in place by fiber pins, (*c*) and (*d*), inserted into holes in the guard block (*e*). The guard blocks consisted of two sections (*f*) and (*g*), similar to the main block, joined by a reinforced brass plate (*h*). This plate served the triple purpose of a radiation shield for the main block, a thermal connection between the two outer sections, and a rigid support by means of which the blocks were

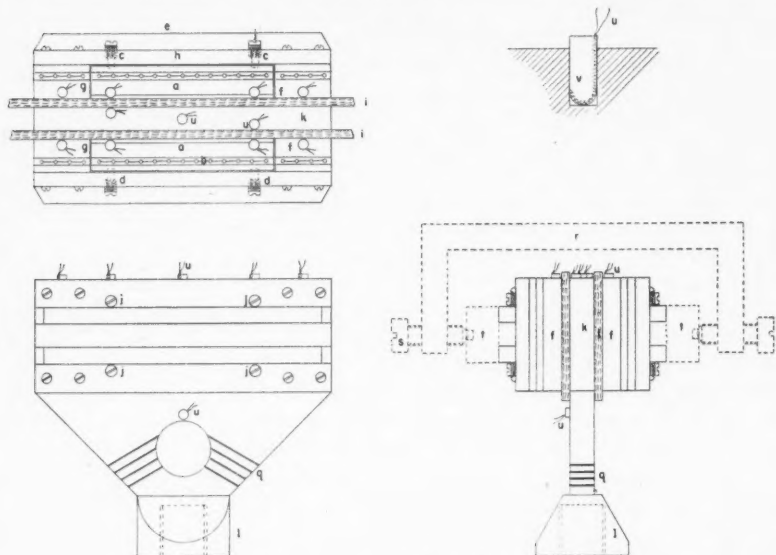


FIG. 1. Measuring unit of second apparatus.

kept in position and were pressed against the sample (*i*). Screws, (*j*), provided adjustment to ensure that the contact surfaces of the main and guard blocks were in the same plane. The heat generated in the blocks passed through the rubber samples to the copper heat sink (*k*). This heat sink extended downwards to a heavy copper collar (*l*), into which was screwed a cylindrical copper block (*m*), about which was wound copper tubing (*n*). Liquid air was drawn through this coil for cooling purposes. A fiber rod (*o*), passing through an opening in the heat sink, supported the apparatus and at the same time insulated it from the outer shell (*p*). A heating coil mounted in grooves (*q*), in the heat sink was employed to prevent variations in temperature arising from fluctuations in the liquid air supply. The thickness of the sample was determined by measuring, before and after the sample was in place, the separation of fine lines scribed on the heat sink and heating blocks. The whole unit was



held firmly together by a large clamp (*r*), equipped with screws, (*s*), which were tightened against the bakelite blocks (*t*).

Eleven thermocouples (*u*) were mounted at various points on the measuring unit, as follows: two on each of the two main blocks (*a*), one on each of the four guard sections (*f*, *g*), and three on the heat sink (*k*). An additional thermocouple placed at the bottom of the heat sink indicated its variation in temperature. In order that the thermocouples might be calibrated without dismantling the apparatus completely they were mounted on small copper plugs (*v*) that fitted tightly into holes in the various blocks. The thermocouple was soldered

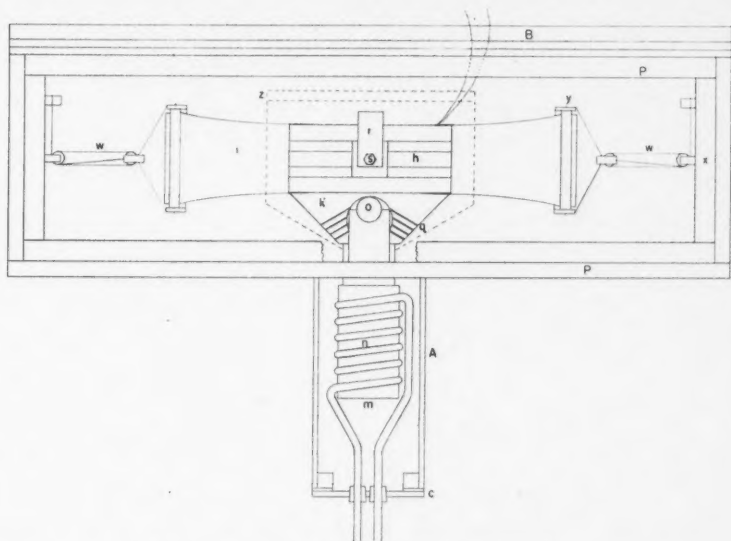


FIG. 2. Side view of second apparatus and cryostat.

to the base of the plug and cemented into a groove along the side, as shown in detail in Fig. 1, thus ensuring that the junction would be deep in the copper and reducing the possibility of errors caused by the conduction of heat along the leads.

Stretching was accomplished by a pulley system (*w*), attached to each end of the sample and to the ends of the cryostat (*x*). The clamps (*y*) gripping the sample (*i*) were of the eccentric roller type, giving a tighter grip as tension was increased. The degree of stretch was measured by the increase in separation of fine lines on the samples.

The measuring unit was enclosed by a radiation shield (*z*) having openings for the rubber samples and the leads. The whole was mounted in a vacuum cryostat (*x*), which was made of brass. The cooling coil (*n*) was enclosed by

the cylindrical tube (*A*) which extended downwards from the base of the cryostat. The top and bottom plates, (*B*) and (*C*), were removable and fitted against rubber gaskets which served as vacuum seals. The cryostat was evacuated by means of a mechanical vacuum pump. A small pump was used to draw the liquid air into the cooling coil where it evaporated and passed in gaseous form through a series of warming coils and the control valves.

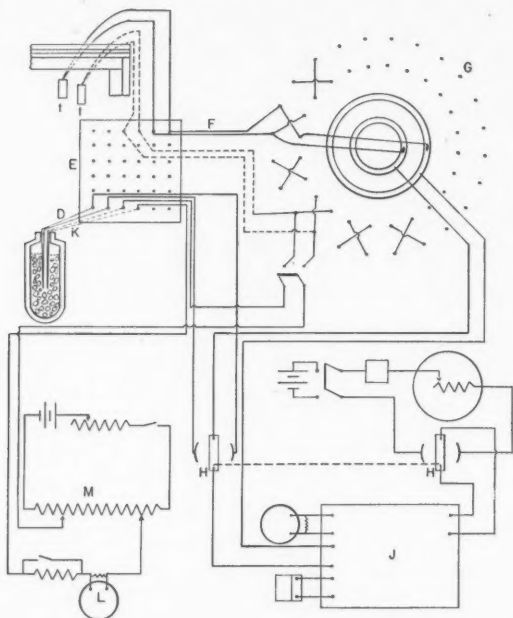


FIG. 3. Thermocouple circuit of second apparatus.

Power for the heating elements was supplied by storage batteries connected to give 12 v., with accurate control of current being provided by suitable rheostats. The voltage and current input to the main heating blocks were read on Weston Model 1 meters, calibrated before use.

As shown in Fig. 3, the circuit ends of all thermocouples (*t*) and of the cold junction (*D*) were taken to a metal-lined, felt-insulated zone box (*E*) where they were joined to heavier copper lead wires (*F*) which in turn were connected to the 24-contact, selector switch (*G*) constructed entirely of copper. Ganged reversing switches (*H*) made it possible to reverse the cold junction and the potentiometer current simultaneously. These reversal provisions were used to prevent errors due to thermal e.m.f.'s in the potentiometer and galvanometer circuit.

Readings were taken by means of a Weston Slidewire potentiometer (*J*) having three ranges with smallest steps of 10, 1.0, and 0.1  $\mu$ v. respectively. Since the calibration of the thermocouples was accurate only to the nearest microvolt the middle range was used throughout. The thermocouple attached to the heat sink could also be connected in series with a separate cold junction (*K*), a sensitive galvanometer (*L*), and an adjustable bucking e.m.f. supplied by student type potentiometer (*M*). This enabled the operator to observe any temperature drift of the heat sink while reading the other thermocouples.

Three thermocouples were calibrated at the steam point, the ice point, the freezing point of mercury, the sublimation point of solid carbon dioxide, and the boiling point of liquid oxygen. Deviation graphs were then plotted against standard copper-constantan tables. The remainder of the thermocouples were calibrated by comparing them with the standard ones.

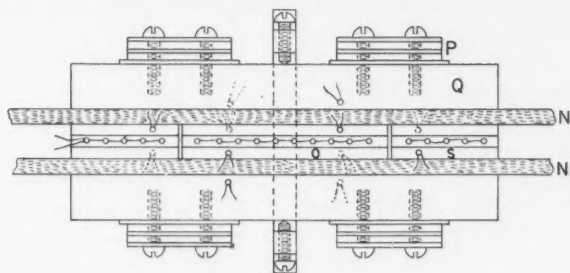


FIG. 4. *Measuring unit of first apparatus.*

A diagram of the measuring unit used for natural rubber is shown in Fig. 4. The two identical rubber samples (*N*), are shown on either side of the copper block (*O*) which acts as the heat source. Thermocouples were attached to the copper blocks by peening, instead of by the plug method of the later version, and flexible connections (*P*) made of double strips of thin copper served as thermal contacts between the outside heat sink blocks (*Q*) and the cooling coil which was situated above the measuring unit. The temperature was regulated by means of gas control valves and the heater elements in block (*O*) and in the guard blocks (*S*). The sides of the cryostat were removable, the thermocouples being taken out through a double gasket at the rear.

This earlier apparatus had the advantage that considerable shielding was supplied by the guard blocks at either end of the main heater, by the heat sink blocks, and by the heat sink itself. This advantage was neutralized, however, by the fact that the rubber samples did not behave identically, with the result that many readings were wasted. The subsequent apparatus did not suffer from this cause, but considerably more care in shielding was found necessary because of the exposed side of each measuring unit. Placing the cooling coil on the under side resulted in smoother operation and gave the added advantage that the apparatus could be assembled from the top, rather than from the side.

### Procedure

The method of taking readings with the second apparatus was as follows. The heaters and air valves were manipulated to bring the heat sink to the desired temperature as quickly as possible. The main and guard heaters were then adjusted to approximately the right power input, and the nitrogen flow and heat sink heater adjusted until the heat sink temperature was relatively constant. The heat sink thermocouple was then switched over to the secondary potentiometer circuit, and thereafter its temperature was maintained constant by adjusting the heater. When the heat sink was stabilized the main and guard heater elements were adjusted until the desired temperature interval, usually between 6°C. and 12°C., was secured and until the guard and main blocks were satisfactorily matched. These conditions were maintained for some time to ensure that equilibrium had been fully reached, and several successive sets of readings of all thermocouples and the meters were taken. When e.m.f.'s of the thermocouples, the current, and the potential drop across the coil had been measured, the conductivity could be determined from Equation (1).

### Experimental Error

The object of the investigation was the measurement of the variation of conductivity with temperature, and it was felt undesirable to attempt to attain a high degree of absolute accuracy because of complications that would be introduced in the relative measurements. It would have been necessary to make dimensions sufficiently large to make possible accurate measurements, to eliminate edge effects, and to simplify determination of the power input. Such an apparatus would be slow to reach equilibrium and very difficult to mount in a vacuum container or to shield from radiation. Moreover, a calibrating determination at room temperature could quite simply be made on the same material at each degree of stretch if so desired. The factors entering into the absolute value of  $K$  are the dimensions, the lead corrections, the calibration errors of the meters, and the degree of stretch. There was an uncertainty in the dimension factor ( $d/A$ ) of approximately 3% and in the correction for lead resistance of 0.5%. The meter calibration error was less than 0.2%. A further error was introduced by an uncertainty of about 5% in the measurement of the degree of stretch, which corresponds to a possible error in  $K$  of 1.3% for GR-S (at room temperature) and somewhat less for natural rubber. The total of these errors is 4%.

The relative calibration of the thermocouples was correct to  $\pm 2 \mu\text{v}$ . which would give an error at the lowest temperatures of about 2%. The total uncertainty of meter readings was 0.5% and variation of lead correction with temperature introduced a further possible error of about 0.5%. Errors due to temperature drift were kept below 0.5% by rejecting all readings where the drift in temperature could have introduced a power error of that magnitude. Radiation and conduction to exposed surfaces and lead conduction were reduced by shielding, and in most cases contributed an error less than 1%. These

errors total 4.5% under the most unfavorable conditions. For larger temperature intervals and higher temperatures where the sensitivity of the thermocouples is greater the error was approximately 3%.

### The Samples

All samples tested were prepared under carefully controlled conditions in the Polymer Physics Laboratory of the University of Notre Dame. Their composition and cure is given in Table I, and the results of some physical tests are given in Table II. These samples differed from ordinary tread stock in that there was no hardening filler, such as carbon black, present.

TABLE I  
COMPOSITION AND CURE OF SAMPLES

	Natural rubber	GR-S
Pure latex	100 parts	—
GR-S	—	100 parts
Carbon black	—	—
Zinc oxide	3.0	5.0
Sulphur	2.7	2.0
Captax	0.9	1.5
Bardol B	—	5.0
Stearic acid	4.0	—
Pine tar	2.0	—
Antioxidant	1.5	—
Cure	120 min. at 274°F.	Optimum cure 60 min. at 298°F. Overcure 120 min. at 298°F.

TABLE II  
SOME PHYSICAL PROPERTIES OF SAMPLES

Sample	Natural rubber	GR-S Optimum cure	GR-S Overcure
300% Stretch modulus, p.s.i.	198	60	68
Tensile strength, p.s.i.	3365	175	105
% elongation possible	760	900	550
% set	14	50	18
Durometer hardness	40	23	24
Specific gravity	0.99	0.99	0.99

In the case of natural rubber the same samples were used throughout. An old sample of GR-S (overcure) was used in both sides during the first tests of the second apparatus, and more or less random readings were taken in the range  $-140^{\circ}\text{C.}$  to  $+50^{\circ}\text{C.}$  New samples were then procured and all subsequent readings taken with them.

### Experimental Results

The thermal conductivity of natural rubber at 0%, 50%, and 100% stretch, and of optimum and overcured GR-S at 0% and 100% stretch is plotted against temperature in Figs. 5 to 10. In these figures solid lines have been used in those cases where the plotted points are believed to represent true conductivity-temperature relationships, while dotted lines are employed in cases where doubt arises concerning the validity of the curve. In addition, some transitions from curve to curve are shown. As an aid to the study of time effects and transitions, the various determinations for natural rubber have been plotted by runs in the order in which they were made and are exhibited in Figs. 11-1 to 11-11. For comparison purposes the results at 0°C. have been summarized in Table III.

#### 1. Natural Rubber

The outstanding feature of the thermal conductivity of natural rubber is its double nature. For almost the entire temperature range covered by the experiments and for all degrees of stretch, the conductivity-temperature graph exhibits two distinct curves. The upper line appears to be continuous throughout the whole range, but the lower part consists of two sections, one for temperatures below and one for temperatures above  $-60^{\circ}\text{C}$ . It will also be noted that, for all degrees of stretch, points occur about half way between the upper and lower curves in the region below  $-70^{\circ}\text{C}$ . It seems probable that these points represent the average conductivity when one of the paired samples is in the state corresponding to the upper curve and the other sample in the state corresponding to the lower curve.

One interesting feature of this double value of the conductivity was the unpredictable manner in which transitions from one state to the other occurred. No consistent pattern was found by which the state the rubber would be in could be predetermined. This caused considerable inconvenience, since it frequently meant getting far more readings than necessary on the upper curve before the lower curve was filled in, and in some cases the complete curve was not obtained. This characteristic of the transition is well shown in Figs. 11-1 to 11-11, where the different runs are plotted separately.

Time effects were a further complicating factor, affecting the zero stretch results particularly, although influencing all to some extent. There were occasions when a balance could not be achieved for some time because a change was apparently in progress. At other times, a balance was achieved but before the readings could be taken a complete change occurred and the final result was far different from the initial conditions. On the only occasion when it was possible to follow the change as it took place, the power input had to be increased by 20% over a period of approximately 10 min. to maintain a constant temperature interval between the main heater block and the heat sink.

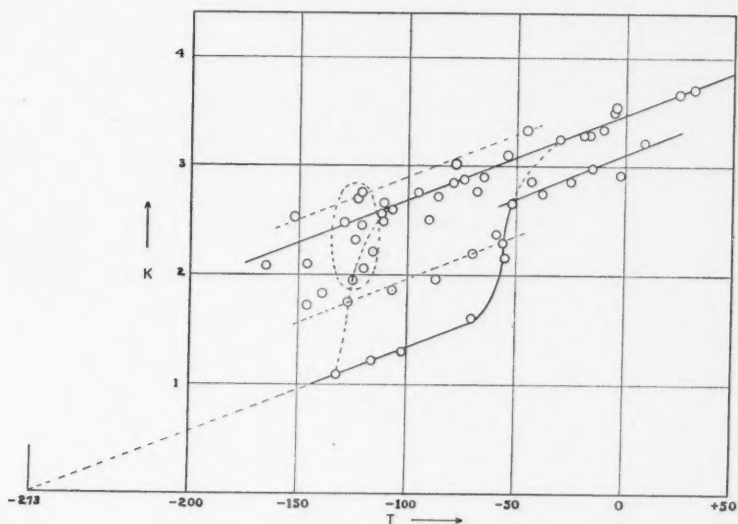


FIG. 5. Natural rubber—unstretched.

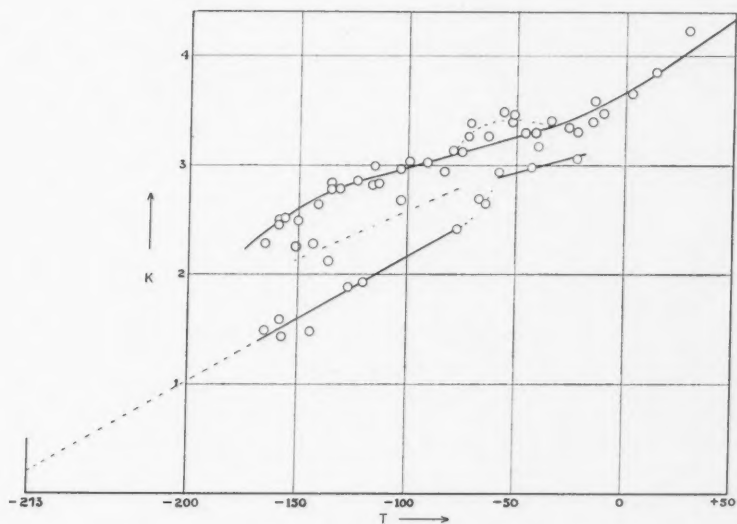


FIG. 6. Natural rubber—50% stretch.



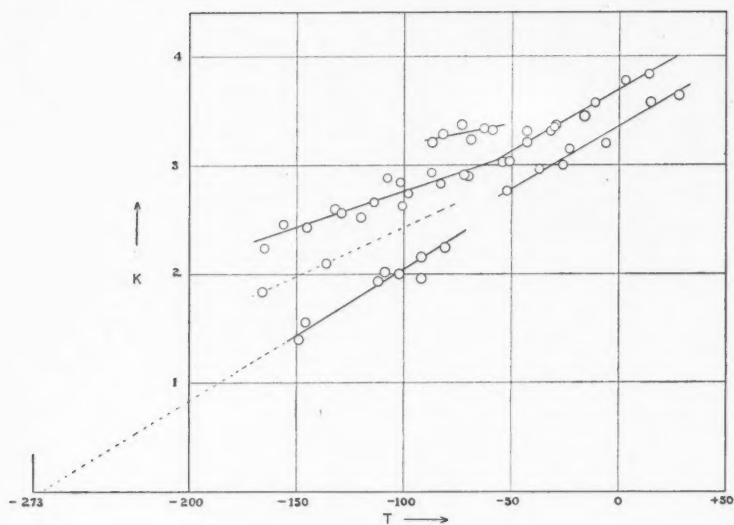


FIG. 7. Natural rubber—100% stretch.

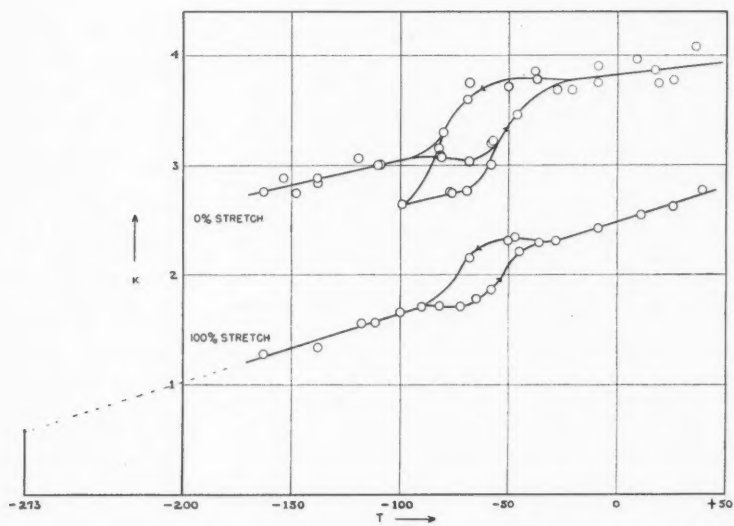


FIG. 8. GR-S. Optimum cure. 0 and 100% stretch.

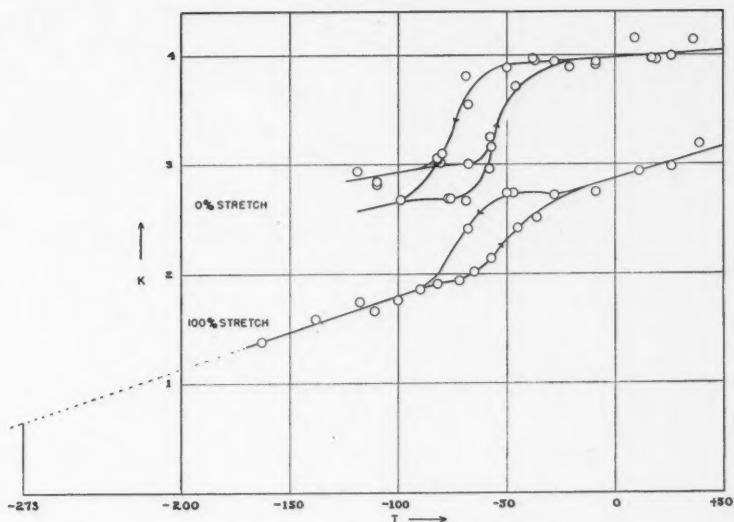


FIG. 9. GR-S. Overcure. 0 and 100% stretch.

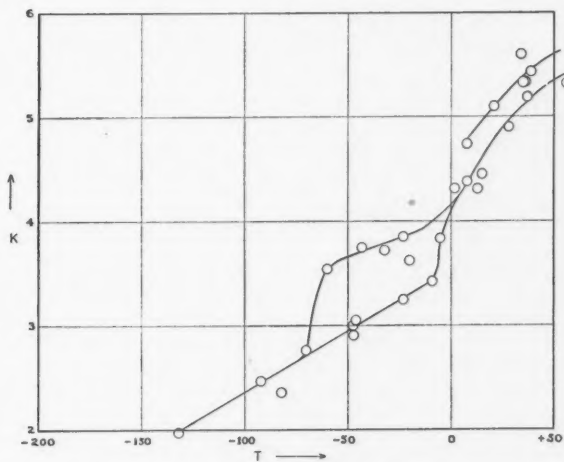


FIG. 10. GR-S. Old sample. Unstretched.

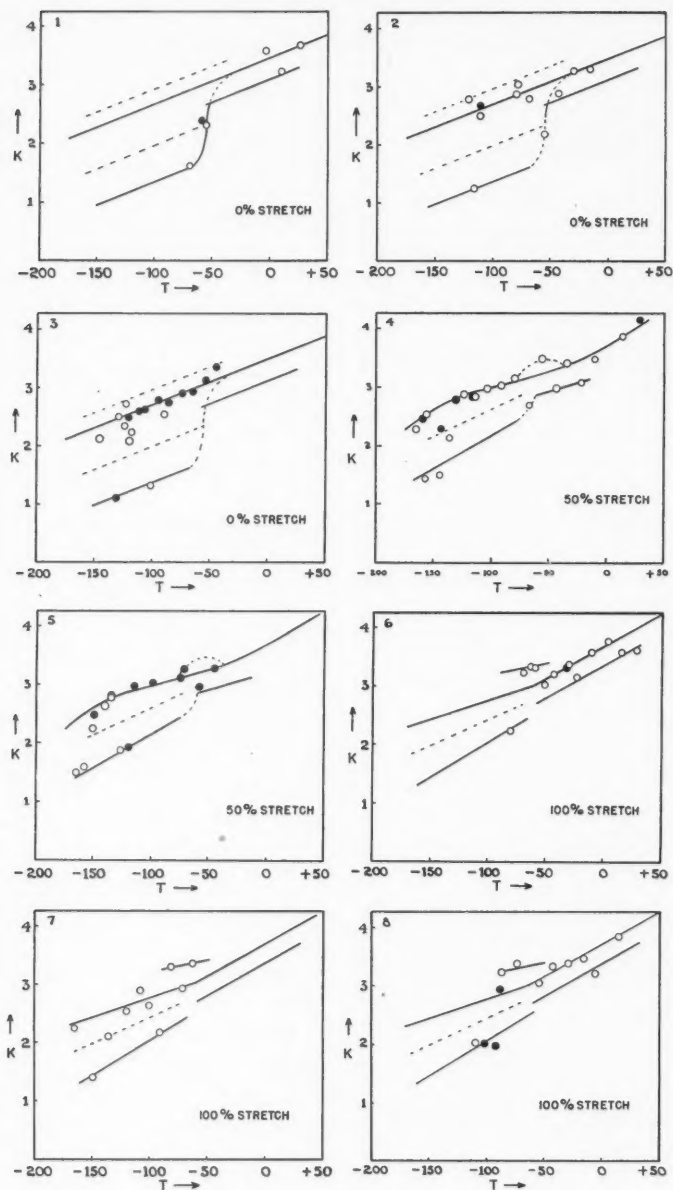


FIG. 11, 1-8. Natural rubber, by runs.

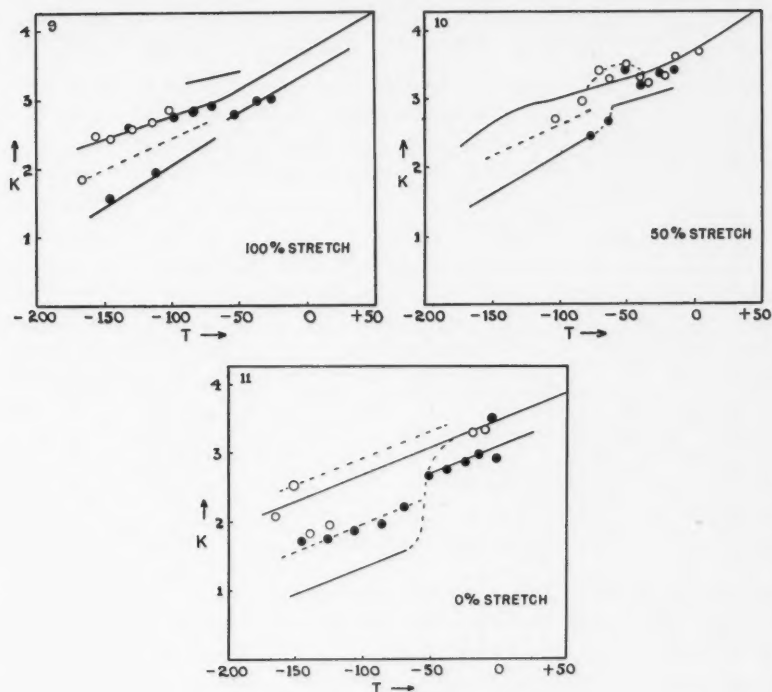


FIG. 11, 9-11. Natural rubber, by runs.

TABLE III  
THERMAL CONDUCTIVITY OF NATURAL RUBBER AND GR-S AT 0°C.

Stretch	0%	50%	100%
	$K \times 10^4$ **	$K \times 10^4$	$K \times 10^4$
GR-S { optimum cure	3.8		2.5
GR-S { overcure	4.0		2.9
Natural rubber { upper line	3.5	3.7	3.7
Natural rubber { lower line	3.1	3.2*	3.3

\* By extrapolation.

\*\*  $K$  in cal./cm. sec. °C.

The results obtained with natural rubber for various degrees of stretch may be summarized as follows:—

(i) 0% Stretch

With the exception of the transition region,  $-80^\circ\text{C.}$  to  $-50^\circ\text{C.}$ , the upper and lower curves of conductivity against temperature are almost linear and

parallel with one another. It may be noted in passing that if the lower curve is extended by linear extrapolation,  $K = 0$  almost exactly at  $T = -273^{\circ}\text{C}$ .

There is a considerable dispersion of points in the neighborhood of  $-120^{\circ}\text{C}$ . which seems to be due to an increased tendency for changes to occur. Fig. 11-3 shows a series of consecutive determinations that were made in this region at a time when considerable variation in the conductivity appeared to be taking place.

(ii) 50% Stretch

The two main differences in these conductivity curves from the results at 0% stretch are a definite bend introduced in the upper curve, and an increase in conductivity, accompanied by a pronounced change in slope, of the lower curve below  $-60^{\circ}\text{C}$ . The slope of the upper curve is increased in the higher temperature range, while staying the same, or possibly decreasing, at lower temperatures. A hump occurs in the  $-50^{\circ}\text{C}$ . to  $-80^{\circ}\text{C}$ . region which will be discussed later. There is also a slight increase in the conductivity throughout, but the magnitude of this change is small and may not be significant. The change in the lower curve on the other hand is quite significant, representing an increase of conductivity of almost 50%. The slope of this part of the curve is difficult to determine, as it was impossible to fill it in completely. A rough linear extrapolation indicates a value for  $K = 0$  slightly below  $-273^{\circ}\text{C}$ . It was not possible to draw in the lower curve above  $-60^{\circ}\text{C}$ . but the three points obtained indicate that its separation from the upper curve is approximately the same as in the case of zero stretch.

(iii) 100% Stretch

The comments made on the differences between the conductivity curves for 0% stretch and 50% stretch apply equally well to the differences between the curves for 0% stretch and 100% stretch. There is, however, a more abrupt change in slope which is shown more clearly because of a smaller degree of scattering of the points. The change is not sufficiently great, however, to indicate whether or not there is a continuous curvature or whether the points represent two straight lines intersecting in the neighborhood of  $-70^{\circ}\text{C}$ . It will be noted that linear extrapolation of the lower part of the graph again indicates that  $K = 0$  at  $T = -273^{\circ}\text{C}$ . The lower curve now extends up to at least  $+30^{\circ}\text{C}$ . If the lower curve may be interpreted as due to crystallization of the elastomer, such an extension would be expected, as it is known that stretching does cause crystallization effects to take place at higher temperatures. It may be significant that this part of the curve does not appear above  $10^{\circ}\text{C}$ . for unstretched rubber, since crystallization normally does not take place above this temperature.

No mention has been made as yet of the anomalous condition found in the region from  $-80^{\circ}\text{C}$ . to  $-40^{\circ}\text{C}$ . and possibly below. It will be noticed that on the graph for 0% stretch a straight line could be drawn from  $-160^{\circ}\text{C}$ . to  $-40^{\circ}\text{C}$ . cutting five points well above the main line. No comment would be justified on the basis of this graph alone, but on the graph for 50% stretch

there is a very definite high region in the curve for the  $-80^{\circ}\text{C.}$  to  $-40^{\circ}\text{C.}$  range, and at 100% stretch this high region has become a completely separate group of points well above the main line. These readings were not all obtained at one time during a single run. It seems unlikely that any heat evolved or absorbed during a transition could cause an error of this magnitude without being detected while the determination was being made. However, the authors are not aware of any experimental or theoretical information confirming or explaining this effect.

## 2. GR-S

The outstanding feature observed in the case of GR-S is the hysteresis loop that appears in the region of the second order transition. The change in conductivity follows the same general pattern for increasing or decreasing temperatures in this region, but the temperature at which the change occurs is  $20^{\circ}$  to  $25^{\circ}\text{C.}$  lower in the latter case. There is some indication that the width of the hysteresis loop may be affected slightly by the rate of heating and cooling, but there is no evidence that the higher conductivity value extends down to temperatures below  $-80^{\circ}\text{C.}$  under any circumstances. A further marked difference between the curves for GR-S and for natural rubber is the continuous nature of the change from upper to lower curves.

There does not appear to be more than one possible value of the conductivity above the transition region. However, there is an indication that more than one value may occur below that region. It seems probable that the double line below  $-80^{\circ}\text{C.}$  is the result of an incomplete transition caused by cooling the sample too rapidly.

No important differences are shown in the results for the conductivities of optimum cure and overcured GR-S. These two specimens had exactly the same history aside from the curing, for they were in the apparatus together at all times. Thus for each determination on the optimum-cured sample there is a corresponding one at the same temperature on the overcured sample. Time effects did not cause the same difficulties in the work on GR-S as were experienced in the case of natural rubber, there being no inexplicable jumps from state to state and no points at which a balance could not be obtained. In general the behavior of GR-S seems to be somewhat less complex than that of natural rubber. This simplicity was offset, however, by the fact that GR-S tears easily and is therefore more difficult to handle.

### (i) 0% Stretch

The values for the thermal conductivity of both the optimum and overcured samples of GR-S at zero stretch are in rather close agreement with the natural rubber results at room temperatures. The change in conductivity that occurs in passing through the transition region is  $0.6 \times 10^{-4}$  to  $0.9 \times 10^{-4}$  cal./sec. cm. deg. C. for the optimum cured sample and slightly greater for the overcured sample; much less than the corresponding change for unstretched natural rubber. The rate of change of conductivity with temperature is also much less

for GR-S than for natural rubber, and extrapolation of the low temperature curve does not indicate that  $K = 0$  at absolute zero.

The points below  $-120^{\circ}\text{C}$ . for the overcured sample have been omitted because at these temperatures shielding difficulties made it impossible to match the guards to the sample. This resulted in a shift of the apparent conductivity to lower values. It was felt that sufficient indication of the trend had been obtained at temperatures above  $-120^{\circ}\text{C}$ . to make further readings at lower temperatures unnecessary.

(ii) *100% Stretch*

Three major changes occur in the conductivity of the samples of GR-S as a result of stretching. In the first place there is a pronounced increase in slope of the curve of conductivity against temperature; secondly, a definite decrease in the value of the conductivity; and thirdly, a decrease in the change of conductivity that occurs when passing through the transition region.

The decrease in conductivity as a result of stretching amounted to approximately  $1.2 \times 10^{-4}$  cal./sec. cm. deg. C. at  $0^{\circ}\text{C}$ ., a change of over 30%. There did not appear to be any significant difference between the two samples in the way in which they behaved when stretched, but the overcured sample became appreciably higher in conductivity than the sample of optimum cure, whereas previously the difference was small. As in the case of unstretched GR-S, extrapolation did not indicate that  $K = 0$  at absolute zero.

The hysteresis loop noted in the results for zero stretch was still very much in evidence at 100% stretch, with almost the same breadth but somewhat reduced height. The possibility of more than one curve in the low temperature region is not seen here because all readings were taken in one continuous run extending over a period of some 30 hr.

3. *GR-S Overcure. Old Sample*

After the second apparatus was completed and before the new samples of GR-S had been received, several test runs at zero stretch were made on a two-year-old, overcured sample of GR-S of the same composition. This sample had been kept at room temperature most of the time, exposed to the air continuously and exposed to light frequently, although not to direct sunlight. Since the measurements provide some indication of the effect of aging they are included here.

The chief effect of aging on this sample appeared to be a considerable broadening of the hysteresis loop to almost  $0^{\circ}\text{C}$ . The conductivity above  $0^{\circ}\text{C}$ . was markedly higher than in the newer samples, reaching almost  $5.5 \times 10^{-4}$  cal./sec. cm. deg. C. at  $+40^{\circ}\text{C}$ . On the other hand, the conductivity below the transition region was slightly lower, the difference being accounted for by a much greater slope throughout the whole range.



### General Considerations

For GR-S, the change in slope of the thermal conductivity-temperature curve with stretch is in agreement with the results on natural rubber for the equivalent sections of the curve. This is also true of the decrease in the change of conductivity in the transition region. However, the downward shift of all parts of the conductivity curve is in marked contrast to natural rubber where the conductivity at lower temperatures actually increased with stretch, at some temperatures by as much as 50%. It should be pointed out that GR-S at 100% stretch probably can not be considered equivalent to natural rubber at 100% stretch and further stretching of natural rubber might reverse the trend.

In general, it would appear that GR-S exhibits a somewhat simpler behavior in the variation of thermal conductivity with temperature than does natural rubber, although this feature may be somewhat exaggerated by the differences in apparatus used in the two cases. It is very interesting to note, also, that for both GR-S and natural rubber the scattering of points is far less at 100% stretch than at 0% stretch, practically all points being well within the calculated experimental error. In view of this fact it would appear that the deviations observed for 0% and 50% stretch should be attributed to variation in the conductivity of the rubber rather than to experimental errors.

The values of the conductivity of unstretched natural rubber and GR-S at 0°C. obtained by us lie between  $3.0$  and  $4.0 \times 10^{-4}$  cal./sec. cm. deg. C. These determinations agree well with previous work by Schallamach (7) and Frumkin and Dubinker (3, 4) who got  $3.1 \times 10^{-4}$  cal./sec. cm. deg. C. and  $4.9 \times 10^{-4}$  cal./sec. cm. deg. C. respectively for natural rubbers of different types. Actually, it is very hard to compare the values, since conductivity varies considerably with composition and porosity and these properties vary considerably in different rubbers.

Double curves such as those shown here have been obtained for rubber by several other experimenters, notably in linear and volume expansion (1) and specific heat (2) studies. Schallamach (7), in conductivity measurements made on North British cycle tubing, got a double portion on his curve below the transition region, but the upper line appeared only during cooling, and when the lower line had been reached by a rather sharp transition the return was always along the same path. The authors are not aware of any experimental work on rubber giving results comparable to the reversible jump from state to state observed by them. However, this may be due to differences in techniques of measurement, many high polymers being particularly sensitive to past history of the sample.

Although some of the apparent scattering in the determinations of the conductivity can certainly be attributed to time effects in the sample, where equilibrium had not yet been reached, it is probable that some of the scattering

is due to variation in properties within the individual samples. These samples were made in a close approximation to commercial methods, and with no particular effort to get uniformity over the entire sample. It would therefore be quite reasonable to expect that there would be sufficient internal variation to cause the most probable transition temperatures to vary appreciably over any large area. In addition, for any determination there was a 6°C. to 16°C. difference in temperature across the sample. It would be possible for one or both of these factors to create differences in the experimental results. Since stretching of the material would be expected to increase the interrelationship between molecular segments, this variation between different parts of the same sample should be considerably decreased, thus explaining the greater consistency obtained in the results for 100% stretch.

At the present time there is no theory of the variation of conductivity of rubber that yields quantitative results. However, it may be instructive to look briefly at the expression given by classical theory for a simple mechanism of conduction, namely,—

$$K = (1/3)dlvc_v,$$

where

$K$  = conductivity,

$l$  = mean free path,

$c_v$  = specific heat at constant volume,

$d$  = density of medium,

$v$  = velocity of sound in medium.

Calculation of  $l$  for natural rubber from this formula, using our experimental values for  $K$ , recent sound velocity (5) data to obtain  $v$ , Bekkedahl and Mathe-son's (2)  $c_p$  data along with Scott's (8) compressibility and Bekkedahl's (1) expansion data for  $c_v$ , gives a value of the order of 2 Angstrom units. This mean free path is less than the length of the isoprene unit which is 8 Å., but very close to the bond lengths, and is a reasonable value. If  $l$  may be considered constant, a positive slope of  $+0.5 \times 10^{-6} K$  units/deg. C. is obtained for the conductivity-temperature curve. This is in reasonable agreement with  $\frac{dK}{dT} =$

$0.8 \times 10^{-6} K$  units/deg. C. obtained experimentally. On the other hand,  $v$  could be expected to increase (5) below the transition, while the compressibility, expansion, and  $c_p$  data suggest that  $c_v$  does not undergo any change, or at best a rather small one. Hence this equation would indicate a larger value for  $K$  below the transition unless some major change occurs in  $l$ . This does not agree with experiment. The equation also indicates that the conductivity should go to zero at  $-273^\circ\text{C.}$  since the specific heat does so. This is indicated by the results of our experiments in the case of natural rubber only.

It has been suggested (6) that the second order transition in elastomers may actually be the result of a series of lambda points spread over a considerable temperature range by the great diversity in size of the molecular segments. The increase in  $c_p$  where these transitions begin would be maintained

afterwards by the continuous absorption of energy as successive afterwards lengths reached their lambda points. This suggestion permits a fairly satisfactory explanation of the fact that the change in thermal conductivity takes place over a much wider range than does the change in specific heat, although commencing at approximately the same temperature. The variation of the specific heat would be a function of the number of segments undergoing transitions, while the variation of the conductivity is much more likely to be a function of the total number of segments that have undergone transitions, and for this reason would spread upwards to higher temperatures.

The data on the effect of stretch on the properties of elastomers are so few that it is almost useless to attempt any explanation of its influence on conductivity. The problem is further complicated by the fact that there are significant differences between the elastomers studied in these experiments. It is obvious that a great deal more experimental work must be done before any clear picture of the mechanisms involved can be drawn.\*

### Acknowledgments

The authors wish to express their appreciation to the Polymer Physics Laboratory of the University of Notre Dame for valuable information and for all rubber samples used. In particular, they would like to thank Prof. E. Guth and Prof. R. L. Anthony of the Department of Physics of that institution for their very considerable assistance during the course of the work. Financial support by the National Research Council of Canada is gratefully acknowledged.

### References

1. BEKKEDAHL, N. J. *Research Natl. Bur. Standards*, 13: 411. 1934.
2. BEKKEDAHL, N. and MATHESON, H. J. *Research Natl. Bur. Standards*, 15: 503. 1935.
3. FRUMKIN, L. and DUBINKER, YU. *Rubber Chem. Technol.* 11: 359. 1938.
4. FRUMKIN, L. and DUBINKER, YU. *Rubber Chem. Technol.* 13: 361. 1940.
5. IVEY, D. G., MROWCA, B. A., and GUTH, E. J. *Applied Phys.* 20: 486. 1949.
6. KRAEMER, E. O. *Advances in colloid science*, Vol. 2, p. 10. Interscience Publishers, Inc., New York. 1946.
7. SCHALLAMACH, A. V. *Proc. Phys. Soc. (London)*, 53: 214. 1941.
8. SCOTT, A. H. J. *Research Natl. Bur. Standards*, 14: 99. 1935.

\* One of the authors (D.G.I.) is at present performing experiments in which the time is treated as a more important variable than in the work discussed here. This is being done in an effort to establish more clearly the nature of the second order transition.

EMISSION OF  $\text{Li}_3^8$  NUCLEI IN COSMIC RAY STARS<sup>1</sup>

BY E. PICKUP AND L. VOJVODIC

## Abstract

One of the more interesting features of cosmic ray stars is that  $\text{Li}_3^8$  nuclei are ejected occasionally in the nuclear disintegrations. Such nuclei are characterized by the fact that, at the end of their range, they suffer radioactive decay ( $\tau = 0.9$  sec.) into  $\text{Be}_4^8$ , which immediately splits up into two oppositely directed  $\alpha$ -particles, giving what is usually referred to as a hammer track. In this investigation numerous examples have been observed of the emission of such nuclei in stars in photographic emulsions, the stars having from 2 to 60 prongs. In particular, it has been shown that the energy spectrum of the  $\alpha$ -particles forming the hammer tracks is in good agreement with that observed by other workers, and also with experiments made, using the cloud chamber technique, indicating that the  $\text{Be}_4^8$  in this disintegration is formed in the excited state. When an electron sensitive emulsion is used it is shown that the hammer track is accompanied by the  $\text{Li}_3^8$  disintegration electron. The energy spectrum of the  $\text{Li}_3^8$  nuclei is plotted, and the mechanism of the formation is discussed for both large and small stars.

## Introduction

Examples of hammer tracks associated with cosmic ray stars in photographic emulsions were first observed by Occhialini and Powell (12), who ascribed these phenomena to the emission of  $\text{Li}_3^8$  nuclei. Similar stars were observed subsequently by other cosmic ray workers. Franzinetti and Payne (6) reported in detail on 28 such events, and showed that the energy spectrum of the  $\alpha$ -particles from the spontaneous disintegration of  $\text{Be}_4^8$ , formed after  $\beta$ -disintegration of  $\text{Li}_3^8$ , agrees satisfactorily with the energy spectrum of the  $\alpha$ -particles observed by Christy *et al.* (4). The latter observed the break-up of  $\text{Li}_3^8$  in a cloud chamber experiment,  $\text{Li}_3^8$  being produced in the nuclear reaction  $\text{Li}_3^8(d, p)\text{Li}_3^8$ .

Hammer tracks were found to be produced in stars formed after negative  $\pi$ -meson nuclear capture (6). They have also been produced in several types of nuclear reactions in photographic emulsions (13, 16). The present work is an account of hammer tracks observed in the examination of some 9000 cosmic ray stars produced in photographic emulsions of various types at an average height of 12,000 ft. The actual height was not very definite, since the plates were exposed in a commercial airplane on transatlantic flights. Reference is also made to a few events we obtained recently in emulsions exposed in a high altitude balloon flight.

Energy Spectrum of the  $\text{Be}_4^8$   $\alpha$ -Particles

The energy spectrum of the  $\alpha$ -particles of the hammer tracks is shown in the full line block curve of Fig. 1, which includes 45 pairs of  $\alpha$ -particles. Five of these events were formed in a laboratory experiment in the nuclear reaction,  $\text{B}_5^{11}(n, \alpha)\text{Li}_3^8$ , one was from a  $\pi$ -meson star and the remainder were from ordinary

<sup>1</sup> Manuscript received July 12, 1950.

Contribution from the Division of Physics, National Research Laboratories, Ottawa, Canada. Issued as N.R.C. No. 2245.

cosmic ray stars. The stars were recorded in C2 (loaded and unloaded), NTB and G5 emulsions.\* The mean range of the pair of  $\alpha$ -particles in each event was measured, and the corresponding energy obtained from the range-energy curve shown in Fig. 2. The  $\alpha$ -particle range-energy curve is that given by Lattes, Fowler, and Cier (9), except for the two points shown at the low energy end of the curve, which were measured by Farragi (5). It is assumed to be the same for all the emulsions.

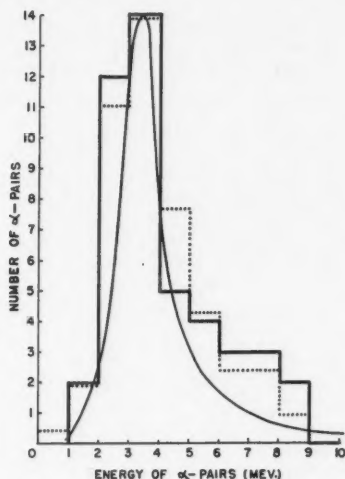


FIG. 1.

A correction has to be applied to the range of the  $\alpha$ -particles as measured in the microscope, because the emulsions, supported on glass, shrink in the vertical plane, after processing, to less than their original size. A shrinkage factor of 2.5 was used, which corresponds to our conditions of processing. Since the most frequent range of a hammer  $\alpha$ -particle is about 6 microns, and there is no preferred orientation in space for the pair, this correction is sometimes appreciable.

The dotted line block curve in Fig. 1 is made up of the present results together with those of Franzinetti and Payne (28 events), and of Titterton (16), who obtained 21 examples of hammer tracks from  $\text{Be}_4^9(\gamma, p)\text{Li}_3^8$  reactions, using synchrotron irradiation of Be loaded emulsions. This gives 94 events, all found in photographic emulsions. The two block curves are normalized to the same total number of events. A further nine events found in balloon-borne emulsions have not been included, but they would not change appreciably the distribution shown. The dotted curve may be compared with the smooth curve in Fig. 1 which is a curve drawn through the experimental results of Bonner

\* Minimum ionization tracks are recorded in Ilford G5 plates but not in the C2 or NTB plates. About half the events were in G5 plates.

*et al.* (3), and normalized to agree with the block curve at the maximum. They employed the  $\text{Li}_3^7(d, p)\text{Li}_3^8$  reaction, using a cloud chamber technique.  $\text{Li}_3^8$  ions were pulled electrostatically into a cloud chamber volume, and thus the  $\alpha$ -particles were formed independently of any supporting film, such as was used in the experiments of Chrjsty *et al.* It will be seen that the agreement between the curves obtained by the different techniques is quite good, especially near the maximum of the spectrum, i.e., 3.3. Mev.

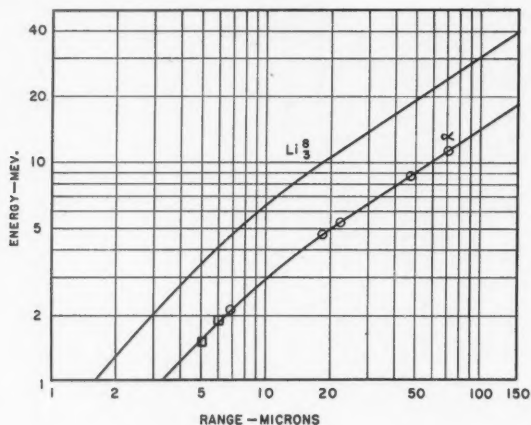


FIG. 2.

Very short range  $\alpha$ -particle pairs, which would be observed if the  $\text{Li}_3^8$  disintegration went directly to the ground state (unstable against decay into two  $\alpha$ -particles by 125 kev.) rather than via the 3 Mev. excited state of  $\text{Be}_4^8$ , are not expected since, theoretically, the direct ground state transition is doubly forbidden by selection rules (4). Bonner *et al.* (3) state that they observed no very short range  $\alpha$ -particles in a cloud chamber experiment. None have been reported in the photographic emulsion work, although, because of the very short range ( $\sim 1$  or 2 microns), we cannot be certain that a few were not missed.

It is also interesting to note that no  $\alpha$ -particle pairs of energy above 9 Mev. were found in the 94 events of the dotted block curve. This confirms that the number of disintegrations concerned above 9 Mev. is  $\leq 1\%$ . Recently, from an analysis of the  $\beta$ -spectrum of  $\text{Li}_3^8$ , Hornyak and Lauritsen (8) have suggested a level scheme for the  $\text{Li}_3^8$  disintegration, which would require about 90% of the  $\beta$ -transitions to occur via the 3 Mev. state and 10% via 10 and 13 Mev. states. Since there are very few  $\alpha$ -particle pairs with energies in the 10–13 Mev. region, presumably gamma ray transitions would be involved, although there is little definite experimental information about this, at present. In this case a final transition to the ground state of  $\text{Be}_4^8$  would lead to very short  $\alpha$ -



particle pairs, which would probably have been detected in photographic emulsions. A possibility might be transition via an excited  $\alpha$ -emitting state.

### Relative Directions of Emission and Ranges of $\alpha$ -Particles

$\text{Li}_3^8$  may be considered to disintegrate into an electron and a neutrino followed by spontaneous disintegration of the residual nucleus,  $\text{Be}_3^8$  within a time of the order of  $10^{-21}$  sec. (given by the width of the 3.3. Mev. peak of the  $\alpha$ -particle spectrum). Allowing for the recoil effect on the  $\alpha$ -particle pair in the break-up, the  $\alpha$ -particles will be collinear within a few degrees and of approximately the same range. Experimentally, the  $\alpha$ -particles usually appeared to be almost exactly in line, although occasionally small angular differences were observed. Similarly there were, occasionally, small differences in range such as might be expected according to the neutrino-electron recoil hypothesis. However, these observations cannot be considered very significant in view of the limitations of the photographic emulsion method for measurements on such short range  $\alpha$ -particles, e.g., the experimental straggling,  $S^1 = 14\%$  for Sm  $\alpha$ -particles (range 6.95 microns) as measured by Lattes, Fowler, and Cuer (9).

### The $\text{Li}_3^8$ Disintegration Electrons

A more final proof that hammer tracks are to be identified with  $\text{Li}_3^8$  nuclei would be given if one observed the  $\text{Li}_3^8$  disintegration electron. We have previously reported cases in which the tracks of  $\text{Li}_3^8$  electrons were visible in the more sensitive emulsions recording singly charged particles of all energies (14). Lord and Schein (11) have also reported a few cases of this. The  $\beta$ -spectrum of  $\text{Li}_3^8$  has an end point at about 13 Mev., and a maximum at about 6 Mev. For 6 Mev. electrons the average angular deviation due to multiple Coulomb scattering in the emulsion is about  $6^\circ$  per 100 microns. Thus most of the decay electron tracks will be fairly straight, and their ionization or grain density will not have much above the minimum value.

We have found, in the past, considerable variations in sensitivity between the different electron sensitive emulsions under the conditions of our experiments and processing, and the situation is further complicated by the fact that the emulsions rapidly acquire a slow electron background. Our criterion for a satisfactory emulsion is that  $\mu$ -meson decay electrons can be seen clearly. For unsatisfactory emulsions of this type, we are usually unable to distinguish a  $\text{Li}_3^8$  decay electron, but, in 21 cases of hammer tracks found in emulsions recording  $\mu$ -meson decay electrons quite well, we found 19 definite examples of  $\text{Li}_3^8$  electrons. The two cases where it was impossible to assign an electron associated with the hammer track may have been due to very unsuitable directions of emission of the electrons. A  $\text{Li}_3^8$  nucleus in a  $\pi$ -meson star also showed an electron. Thus, it appears safe to conclude that all the hammer tracks may be ascribed to  $\text{Li}_3^8$  nuclei.

The electron track was of sufficient length in the emulsion in only a few cases to make possible accurate scattering measurements. Fig. 5 (*a, b, c, d*) gives four



examples of mosaics of photomicrographs showing cosmic ray stars in which  $\text{Li}_3^8$  disintegration electrons can be seen starting from the origin of the  $\text{Be}_4^8$   $\alpha$ -particles. Fig. 6(c) shows a small cosmic star in which the length of the electron track was about 750 microns before leaving the emulsion, and the energy, as measured by small angle scattering, was 7 Mev. It was found in an Ilford G5 emulsion, developed in elon. This developer gives a somewhat bigger grain size than the usual D19 developer, so that minimum ionization tracks are more clearly visible.

### Frequency of Emission of $\text{Li}_3^8$ Nuclei

Franzinetti and Payne (6) have given 0.185% as the relative frequency of  $\text{Li}_3^8$  nuclei compared with fission fragments, protons, and  $\alpha$ -particles in the stars in emulsions exposed at mountain top altitudes. In the present results,

TABLE I  
ENERGIES OF  $\text{Li}_3^8$  FRAGMENTS IN STARS OF DIFFERENT SIZES

N	2	3	4	5	8	10	11	12	13	17	18	20
E	16.5*	23.5*	18.5	30.5	26.5*	37	21*	25.5†	17†	22†	10*	27
	8.0*	8.2	18*	19			16.5†		16			
	5.0*	8.0	11	6.4								
	3.0*	4.8	10	5.0								
	2.3	3.9	9.4	4.8								
		3.5*	5.4*									
			5.0									
			3.0									
			~1*									

N	22	23	24	26	34	47	60
E	16†	41	26	25†	60†	32†	75†
		21*	16				

N = No. of prongs in star  
E = Energy of  $\text{Li}_3^8$ , Mev.

\* Recorded in C2 and NTB plates; others in G5 plates.

† Balloon flight; G5 plates.

40 events were found in about 9000 stars in emulsions exposed at airplane altitudes, giving a percentage of 0.10 of  $\text{Li}_3^8$  nuclei compared to the total number of tracks, if we take an average of 5.0 tracks per star.\* We have observed a further nine events of this type in 1000 stars, which were found in G5 emulsions exposed at high altitude in a free balloon flight. Seven of these were in medium-large stars and two in stars with extensive meson showers. This gives a somewhat higher percentage than the airplane results, but the number of events is too small to be very significant statistically. Adelman and Jones (1) have observed 11  $\text{Li}_3^8$  events in about 3000 stars produced by the nuclear capture of negative  $\pi$ -mesons.

The  $\text{Li}_3^8$  nuclei have been observed in both small and large stars as Table I shows. If we group the stars into two classes on this basis, there does not

\* The measured average for C2 plates was 4.5, and for G5 plates, 5.3, the latter being greater because minimum ionization tracks are also recorded here. Since about 50% of these events were recorded in G5 plates, a mean average of 5 tracks per star is used.

appear to be any major variation in the probability of formation of  $\text{Li}_3^8$  between the two classes.

### Energy Spectrum of the $\text{Li}_3^8$ Nuclei

The energy distribution is shown in Fig. 3 for 40 stars giving  $\text{Li}_3^8$  fragments. The results are separated into two classes, i.e.,  $\text{Li}_3^8$  nuclei emitted in those stars having not more than five prongs, and those with eight prongs or more. No cases were found for stars with between five and eight prongs. This separation has been made since the smaller stars can usually be explained in terms of simple nuclear reactions induced in the lighter elements in the emulsion, carbon, nitrogen, oxygen, and any light element introduced as loading material. The larger stars represent disintegrations produced in the silver and bromine of the emulsion.

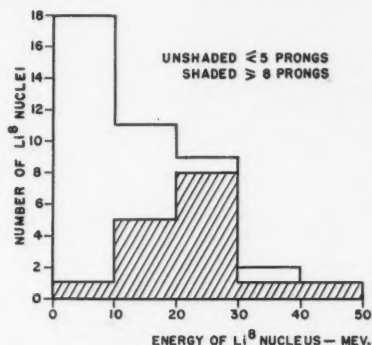


FIG. 3.

Some of the stars were found in the older emulsions (C2, loaded and unloaded, and NTB) recording electrons up to about 50 kev. only, and some in electron sensitive emulsions, which will record all particles having unit charge. Whilst some tracks of the stars were, undoubtedly, not recorded in the less sensitive emulsions the energy distributions given in Fig. 3 should not be changed radically on this account.

The energies of the  $\text{Li}_3^8$  fragments were obtained from their measured ranges by using the range-energy curve for  $\text{Li}_3^8$  given in Fig. 2. This was calculated from the range-energy curve for  $\alpha$ -particles, also shown in Fig. 2, assuming the relation  $R = (\text{constant}) \cdot M/Z^2 \cdot f(v)$ , to hold for  $\text{Li}_3^8$ , where  $R$  = range,  $v$  = velocity, and  $M$  and  $Z$  are the mass and charge respectively. Thus, for the same  $E/M$ , where  $E$  = energy,  $R(\text{Li}_3^8)/R(\alpha) = M(\text{Li}_3^8)/M(\alpha) \cdot [Z(\alpha)/Z(\text{Li}_3^8)]^2$  i.e.,  $R(\text{Li}_3^8) = 8/9 \cdot R(\alpha)$ . Below 3 Mev., measurements of Farragi (5) on  $\text{Li}_3^8$  ranges indicate that the predicted energy values for  $\text{Li}_3^8$  may be too great.

A correction should be made also, since a certain fraction of events will not be recognized, because the  $\text{Li}_3^8$  leaves the emulsion before ending its range. This correction becomes important for long range tracks. Thus Fig. 4 shows

the energy distribution curve obtained after making this correction, and assuming that the  $\text{Li}_3^8$  nuclei have an equal probability of being emitted in all directions. We have noticed no marked anisotropy in the directions of emission. It will be seen, however, that the main features of the curve are unchanged by this correction.

In general it appears that the more energetic fragments are emitted in the larger stars, and for these there is a maximum of the energy distribution between 15 and 30 Mev. In the small stars the  $\text{Li}_3^8$  will be the main residual nucleus, and its short range, in general, is consistent with such stars being formed by fairly low energy incident neutrons. It is interesting to note, however, that occasionally the  $\text{Li}_3^8$  in a small star is quite energetic, as shown in Table I.

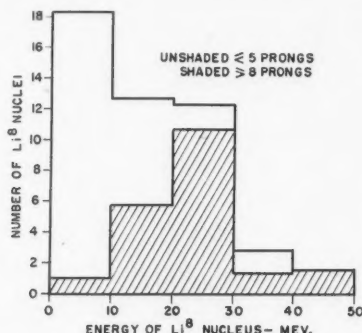


FIG. 4.

The energy spectrum of Fig. 4 may be compared with that of Harding, Lattimore, and Perkins (7) for  $\alpha$ -particles emitted in stars with from 10 to 22 prongs. The mean energy of emission of the  $\text{Li}_3^8$  nuclei is seen to be greater than that of the  $\alpha$ -particles. The statistical evaporation theory with considerations of thermodynamic equilibrium cannot be expected to hold for many of the energetic stars involved here, and so the question of the mean energy and the relative probabilities of emission will not be discussed further. Le Couteur (10) has recently given a description of highly excited nuclei using the evaporation theory, and Weisskopf's method of detailed balance, which explains some features of larger stars with up to 14 prongs.

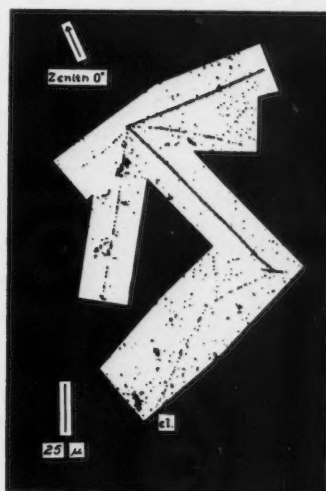
## Discussion

### (I) Ejection of $\text{Li}_3^8$ in Small Stars

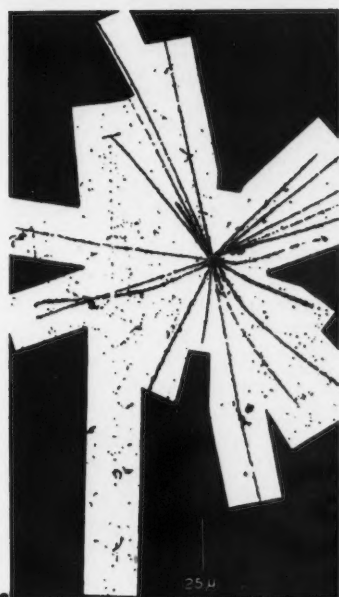
It appears certain that most of the smaller stars ( $\leq 5$  prongs) can be identified with fairly simple light element reactions, and there are several possibilities for  $\gamma$ -ray, neutron, and proton induced reactions for the carbon, nitrogen, and oxygen in the emulsion. Thus Franzinetti and Payne (6) identify many of their events with the reaction  $\text{C}_6^{12}(n; \alpha, p)\text{Li}_3^8$ , giving a 3-pronged star, and some of



(a)



(b)



(c)



(d)

FIG. 5 a, b, c, d.

our 3-pronged stars can be identified according to this reaction. A possible interpretation of the 4-pronged star in Fig. 6(c) would be the reaction  $O_8^{16}(n; 2\alpha, p)Li_3^8$ . Table I shows that we get approximately equal numbers of 3-, 4-, and 5-pronged stars, and also a few 2-pronged stars.

Some of these stars were found in electron sensitive emulsions. Three 5-pronged stars are shown in Fig. 5 (a), (b), and (d). Two of them contained particles of unit charge which would not have been recorded in the C2 or NTB emulsions. They were either mesons, protons, or deuterons, but were of too short range before leaving the emulsion to identify definitely by grain counting and small angle scattering measurements.

Many small cosmic ray stars show a light track together with a few low energy fragments, a likely explanation being that the light track is a proton or deuteron of energy, several hundred Mev., which initiates a small disintegration, being itself a secondary particle from a more energetic star generated outside the emulsion. Attempts to explain the 5-pronged stars on simple lines like this, however, often lead to difficulties in accounting for the momentum balance and in postulating suitable light element reactions. Furthermore, the light tracks in Fig. 5 (b) and (d) are all in the lower hemisphere away from the zenith, and one of the light tracks, if incident, would be coming from below. This is not impossible, but unlikely, especially at the lower altitudes. Neutron initiated reactions may, perhaps, be postulated such as

$$N_7^{14} + n_0^1 = Li_3^8 + 2d_1^2 + 2p_1^1 + n_0^1$$

or

$$N_7^{14} + n_0^1 = Li_3^8 + T_1^3 + 2p_1^1 + 2n_0^1 + (\text{meson})_0^0.$$

There is the alternative possibility of these stars being induced in the silver or bromine of the emulsion. The star in Fig. 5(a) has two very short recoils in addition to a short  $Li_3^8$  fragment and two more energetic tracks, and the short recoils may have been heavy residual nuclear fragments. One difficulty in identifying reactions is the poor discrimination between low energy tracks of protons, deuterons, tritons, and  $\alpha$ -particles in the electron sensitive emulsions.

There were some examples of 2-pronged stars, consisting of an identified  $\alpha$ -particle and a  $Li_3^8$  nucleus. Since these were found in C2, boron-loaded emulsions only, it is reasonable to identify them as being due to the  $B_6^{11}(n, \alpha)Li_3^8$  reaction, caused by cosmic neutrons in the low energy range, presumably secondary neutrons from local stars. There were 4 definite cases in 1200 stars found in Ilford C2, boron-loaded emulsions. Similar events have been reported by Yagoda and Kaplan (17). An example is shown in the photomicrograph in Fig. 6(a). Fig. 6(b) shows, for comparison, two examples of similar, lower energy events, produced by neutrons from a  $Li_3^7(d, n)2\alpha$  source in the laboratory by Pickup (13). A 2-pronged star found in an unloaded C2 emulsion showed only a low energy proton, (or particle of unit charge) and a  $Li_3^8$  nucleus, but this has not been classified, unless we postulate a reaction in silver or bromine.

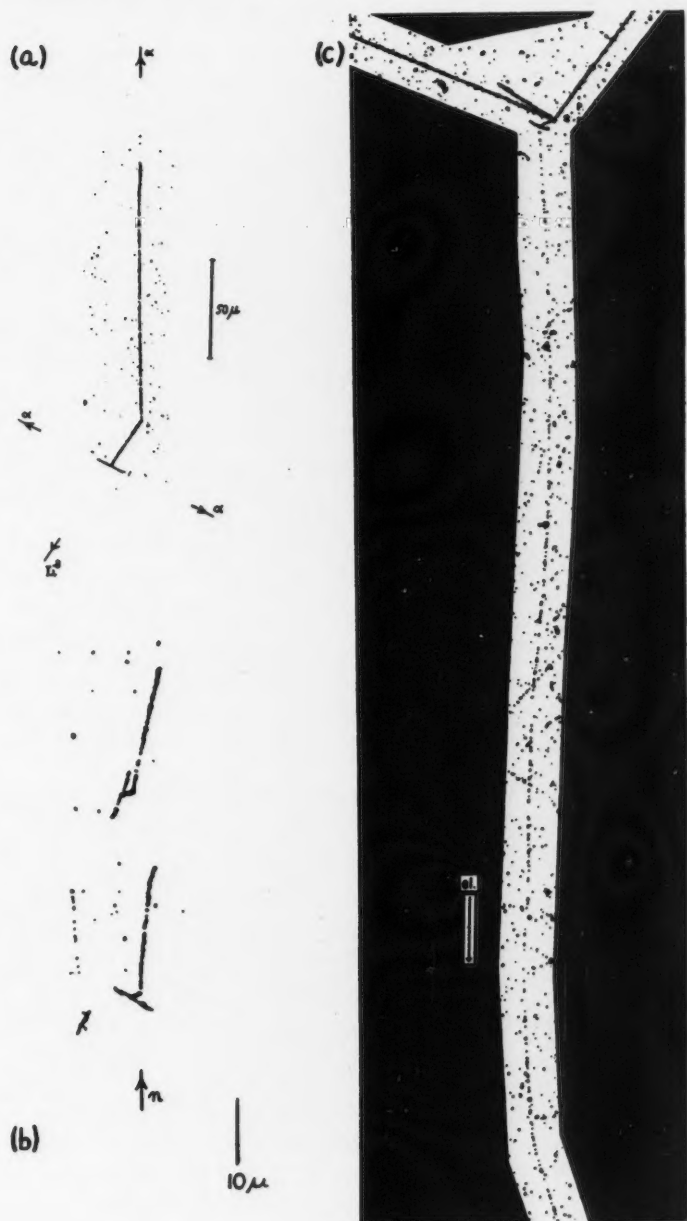


FIG. 6 a, b, c.

### (II) Ejection of $\text{Li}_3^8$ in Large Stars

About 40% of the  $\text{Li}_3^8$  fragments were emitted in stars having 8 or more prongs, and these will be stars produced in the silver and bromine in the emulsion by the more energetic cosmic rays. As was pointed out earlier, the energy of most of these  $\text{Li}_3^8$  nuclei lies between 15 and 30 Mev. The stars in question should probably be classified as medium energy stars since, in general, they contain mainly low energy fragments in contrast to the more energetic stars which have, in addition, a downward shower of relativistic, singly charged particles consisting mainly of mesons. Recently we found  $\text{Li}_3^8$  fragments in 10-, 11-, 13-, 16-, 24-, 26-, 34-, 47-, and 60-pronged stars in G5 emulsions flown at high altitude in a free balloon flight. Except for the two largest stars, which contained extensive meson showers, these were also medium energy stars according to the above classification. They have all been included in Table I.

In a few cases an incoming primary track was visible in electron sensitive emulsions. It appears likely, however, that many of the medium energy stars discussed above were initiated by energetic secondary neutrons. The 60-pronged star appeared to be caused by an incoming heavy primary nucleus.

Occasionally, other nuclei are ejected in cosmic ray stars. They are usually of short range, and classified as fission fragments. Thus, in the case of the 24-pronged star shown in Fig. 5(c) there were two heavy fragments besides the  $\text{Li}_3^8$ , and of somewhat shorter range. Sometimes, also, unstable nuclei other than  $\text{Li}_3^8$  are emitted. We have observed three such cases, showing a disintegration electron originating at the end of the fragment. Unlike the case of  $\text{Li}_3^8$ , however, it is usually impossible to identify such nuclei in the emulsion, unless their energy and range are sufficiently great so that identification can be made by means of the delta-ray method, or considerations of the thinning-down length.

The probability of occurrence of such energetic nuclei is extremely small. Sorensen (15) has observed very energetic boron, beryllium, and lithium fragments, one  $\text{Li}_7^7$  nucleus having an estimated energy of 500 Mev. A  $\text{Li}_2^8$  nucleus with an energy of about 90 Mev. was recorded by Bonetti and Dilworth (2) in a star. The continued use of very thick or multi-layer emulsions, increasing the chance of detecting and following long tracks, should lead to more information on the types and numbers of energetic  $\text{Li}_3^8$  and other heavy and light nuclei ejected in cosmic ray stars.

### (III) Formation of $\text{Li}_3^8$ in the Disintegration

The statistical evaporation theory will give a certain probability for the emission of  $\text{Li}_3^8$ , but since this theory cannot be applied to the light element stars or to the more energetic of the large stars, it is interesting to attempt to explain the appearance of  $\text{Li}_3^8$  in a somewhat different way. The occurrence of heavy fragments, sometimes of considerable energy, in stars may, perhaps, be regarded as evidence for the temporary existence of heavy sub-units as part of



an internal nuclear structure. It is natural to attempt to interpret the formation of  $\text{Li}^8$  in terms of  $\text{Be}_4^8$  as a temporary sub-unit. In the case of a neutron induced reaction in a light element we might suppose that the incident neutron interacts directly with  $\text{Be}_4^8$  according to the reaction,  $\text{Be}_4^8(n, p)\text{Li}_3^8$  thus giving  $\text{Li}_3^8$  and a proton with the subsequent emission of the remaining nuclear components, e.g., the reaction,  $\text{C}_6^{12}(n, p, \alpha)\text{Li}_3^8$  may possibly be explained in this way.

For the heavier elements, disintegrated in general by more energetic incident particles, the  $\text{Li}_3^8$  may be produced by the interaction of a secondary neutron, formed within the nucleus, with a  $\text{Be}_4^8$  sub-unit. It is, of course, by no means certain that the internal construction of the nucleus can be considered in such a simple way. Further work on some of these more complicated reactions, and on the relative frequency of occurrence of different kinds of heavy fragments, might give useful information on the general question of nuclear structure.

### Acknowledgments

We have great pleasure in thanking Trans-Canada Airlines for carrying emulsions for us on transatlantic flights. The emulsions exposed at balloon altitudes were carried aloft through a collaborative program of cosmic ray investigations by the Bartol Research Foundation and the National Research Council, with the co-operation of the Office of Naval Research Project, "Skyhook". The systematic scanning of emulsions was done by Misses Shirley Young, Beverley Mear, and Barbara Woodruff, and Mr. D. Rushton was responsible for the photomicrographs which illustrate this paper. We are indebted to Dr. J. Spence of the Eastman Kodak research laboratory for pointing out to us the possibility of using elon as a developer.

### References

1. ADELMAN, F. L. and JONES, S. B. *Bull. Am. Phys. Soc.* 24: 18. 1949.
2. BONETTI, A. and DILWORTH, C. *Phil. Mag.* 40: 585. 1949.
3. BONNER, T. W., EVANS, J. E., MALICH, C. W., and RISSER, J. R. *Phys. Rev.* 73: 885. 1948.
4. CHRISTY, R. F., COHEN, E. R., FOWLER, W. A., LAURITSEN, C. C., and LAURITSEN, T. *Phys. Rev.* 72: 698. 1947.
5. FARRAGI, H. *Compt. rend.* 229: 1223. 1949.
6. FRANZINETTI, C. and PAYNE, R. N. *Nature*, 61: 735. 1948.
7. HARDING, J. B., LATTIMORE, S., and PERKINS, D. H. *Proc. Roy. Soc. (London)*, A, 196: 325. 1949.
8. HORNYAK, W. F. and LAURITSEN, T. *Phys. Rev.* 77: 160. 1950.
9. LATTES, C. M. G., FOWLER, P. H., and CUER, P. *Proc. Phys. Soc. (London)*, 59: 883. 1947.
10. LE COUTEUR, K. J. *Proc. Phys. Soc. (London)*, 63: 259. 1950.
11. LORD, J. J. and SCHEIN, M. *Phys. Rev.* 77: 19. 1950.
12. OCCHIALINI, G. and POWELL, C. F. *Nature*, 159: 93. 1947.
13. PICKUP, E. *Phys. Rev.* 74: 495. 1948.
14. PICKUP, E. and VOJVODIC, L. *Phys. Rev.* 76: 1535. 1949.
15. SORENSEN, S. O. C. *Phil. Mag.* 40: 947. 1949.
16. TITTERTON, E. W. *Nature*, 165: 721. 1950.
17. YAGODA, H. and KAPLAN, N. *Phys. Rev.* 75: 1328. 1949.

## ETUDES SUR LES RAYONS COSMIQUES A L'AIDE D'EMULSIONS PHOTOGRAPHIQUES SPECIALES<sup>1</sup>

PAR PIERRE DEMERS

### Sommaire

Les émulsions photographiques à grains fins préparées par l'auteur ont été appliquées à l'étude des rayons cosmiques, surtout sous la forme de *feuilles d'émulsion sans support* épaisses de  $150\ \mu$  empilées pour former un milieu sensible continûment dans une épaisseur de l'ordre de quelques millimètres d'émulsion, équivalente de quelques mètres d'air. Ces empilements ont été irradiés dans des ascensions de ballons-sondes à 25-35 km. d'altitude. La préparation et la manipulation des feuilles sans support sont décrites. Leur examen a permis de trouver un grand nombre de trajectoires se continuant d'une feuille d'émulsion dans la suivante, et de reconstituer ainsi les traces complètes d'étoiles occupant plusieurs feuilles de l'empilement. *L'efficacité de la méthode* de superposition, évaluée comme étant la probabilité qu'une trajectoire soit visible dans la feuille suivante où elle se dirige, est de 86% dans un cas particulier examiné.

Deux grands événements occupant respectivement six et quatre feuilles, sont analysés à titre d'exemples. L'un d'eux est une étoile double avec un proton de 200MV de parcours  $1630\ \mu$  comme particule intermédiaire. L'énergie apportée par la particule incidente est environ 1315MV dans ce cas, et 400MV dans l'autre.

On a observé la désintégration presque symétrique  $C12 \rightarrow 3\alpha$  avec une faible énergie. On a aussi observé des *étoiles simples* n'ayant qu'une branche longue (méson, proton, triton,  $\alpha$ ), et un noyau de recul très court dont l'observation serait difficile sans l'émulsion à grain fin employé. Des étoiles aussi simples paraissent avoir échappé jusqu'ici aux études faites à l'aide d'autres émulsions. Elles paraissent être assez fréquentes cependant puisqu'on en a observé 4 sur un total de 31.

Deux appareils nouveaux sont décrits. Le premier est un *pantographe optique* qui a grandement facilité l'établissement de cartes d'exploration complètes des feuilles d'émulsions. Le second est un *appareil continu de photomicrographie*, qui a permis d'obtenir commodément des reproductions photographiques de trajectoires très longues ou très obliques sans la nécessité de prendre des séries de négatifs distincts.

Une étude actuellement en cours sur *l'anisotropie des rayons cosmiques* à l'aide de ballons-sondes est décrite. On utilise une boussole formée d'un aimant type Alnico suffisamment gros, portant l'empilement d'émulsions sans support, qui reste ainsi orienté de façon exacte par rapport aux points cardinaux pendant toute l'ascension.

### I. Introduction

Les premiers travaux sur les rayons cosmiques utilisant les émulsions photographiques sont ceux de Blau et Wambacher (7, 8, 9), et de Wilkins (43). De nombreux travaux ont paru depuis ce temps sur ce sujet, et selon des renseignements personnels, il occupe à l'heure actuelle au moins une trentaine de groupes de chercheurs, dont la moitié aux États-Unis.

L'auteur a pu préparer dès 1945 (13, 15) des émulsions photographiques sensibles aux trajectoires individuelles des particules ionisantes, possédant un grain extrêmement fin et une sensibilité élevée puisqu'elles manifestaient même des électrons de 50 kv. environ (13, 15), et un pouvoir discriminatoire excellent, qui a été mis à profit dans l'étude des fragments de fission (14, 16).

<sup>1</sup> Manuscrit reçu le 25 avril 1950.

Contribution de l'Institut de Physique, Université de Montréal, Montréal, P.Q.

Il a paru intéressant de chercher ce qu'elles révéleraient dans une étude des rayons cosmiques.

Après divers essais plus ou moins fructueux d'irradiation de ces émulsions portées sur un support de verre (17, 22, 24), des résultats ont été obtenus avec ces émulsions sous forme de feuilles sans support empilées de façon à former un milieu sensible continu épais de plusieurs millimètres.

## II. Premières conditions d'irradiation

De telles plaques sensibles avec support de verre ont été exposées aux rayons cosmiques en 1945 et 1947 au Mont Evans, altitude 4200 m., dans deux ascensions de fusées V-2 au Nouveau Mexique, altitudes 96 et 177 km., et dans des voyages transatlantiques de la B.O.A.C., altitude 10 km. grâce respectivement à la courtoisie de M. Mario Iona Jr. à l'Université de Denver, Colorado, de M. Krause, de l'O.N.R. des États-Unis et de M. Adair Morrison, du Conseil National des Recherches, Ottawa. Cependant ces irradiations n'ont pas donné tous les résultats espérés pour diverses raisons: dans le cas d'une fusée V-2, les plaques s'étaient cassées en mille miettes à l'atterrissage, dans d'autres cas les plaques s'étaient voilées, ce qui leur arrive habituellement si on les garde plus de trois semaines une fois sensibilisées à la température de la pièce; ou encore l'émulsion s'était écaillée et avait quitté son support de verre, sous l'effet d'une atmosphère trop sèche. Nos émulsions présentent de plus une régression relativement rapide de l'image latente (28, 29), qui est sensible déjà après un jour à la température de la pièce.

Pour toutes ces raisons, il est avantageux de conserver ces émulsions à la glacière jusqu'au moment de l'irradiation, de réaliser l'irradiation à une température voisine de 25°C., en moins d'un jour, et de les développer immédiatement, ou encore, de les conserver à très basse température jusqu'au moment du développement.

Ces conditions de manipulation ne sont pas faciles à remplir si l'on doit recourir à des transports à grande distance. De plus une irradiation d'un jour à 3,800 m. ou à 10 km. n'inscrit pas un nombre très grand de phénomènes par unité de surface des plaques sensibles. Il est au contraire recommandable de recourir à des irradiations dans la stratosphère: des ballons-sondes peuvent y séjourner quelques heures, la densité des trajectoires est alors suffisante, et si on les retrouve rapidement après l'ascension, on peut développer les plaques avant que l'image latente ait pu s'affaiblir notablement.

Signalons un avantage d'une régression rapide de l'image latente: les trajectoires inscrites depuis longtemps sont disparues au moment du développement, de sorte qu'une trajectoire qui apparaît nettement sous le microscope est certainement due à un phénomène récent: le nombre d'étoiles et de trajectoires inscrites au sol, où l'intensité du rayonnement cosmique est faible, est toujours négligeable vis à vis du nombre de celles qui s'inscrivent en quelques heures à une altitude où le rayonnement est 50 ou 100 fois plus intense.

### III. Ascensions de ballons-sondes

Nous avons donc entrepris à l'Institut de Physique de l'Université de Montréal, de lancer des ballons-sondes, utilisant pour cela les ballons de néoprène de Dewey et Almy J350, J800 et J2000, pesant respectivement environ 350, 800 et 2000 g., gonflés à l'hydrogène. Nous avons employé de trois à six ballons attachés à une nacelle portant les émulsions sensibles, et d'ordinaire, une radio-sonde. Les premières ascensions ont été faites en 1947.

Pour obtenir des résultats, il faut réunir les trois conditions suivantes. 1°) l'émulsion doit être de bonne qualité, c'est à dire, sensible et sans voile. 2°) l'ascension doit faire séjourner les émulsions à haute altitude, soit au dessus de 25 km. pendant quelques heures. 3°) le ballon-sonde doit être récupéré au plus tard quelques heures après son retour au sol.

Dans le but de contribuer à la récupération des ballons-sondes, des radio-sondes réparables par goniométrie ont été réalisées et essayées, elles seront décrites ailleurs (18).

Une ascension faite le 14 juillet 1949 a donné d'excellents résultats. L'émulsion était de bonne qualité, une altitude de 25-35 km. a été maintenue pendant deux heures environ, les émulsions sensibles étaient dans une glacière à 0-5°C. vingt minutes après leur retour au sol, et dans la neige carbonique soit à -85°C., douze heures après le début de l'ascension; les émulsions n'ont ensuite été réchauffées qu'au moment du développement, de sorte que la régression de l'image latente a été entièrement évitée. Ces émulsions étaient des feuilles sans support empilées.

Quelques résultats de leur examen ont été décrits brièvement (19, 21).

### IV. Empilements de feuilles d'émulsions sans support

L'émulsion a été préparée avec un appareil nouveau, suivant la formule 2 modifiée en suivant exactement les indications données ailleurs (20). Des additions ont été faites à l'émulsion liquide; en utilisant les quantités suivantes:

- 900 cm.<sup>3</sup> émulsion refondue
- 5 à 8 cm.<sup>3</sup> triéthanolamine
- 0.8 g. éosine jaunâtre
- 50 cm.<sup>3</sup> alcool.

L'émulsion a ensuite été coulée en une couche épaisse de 3 mm. sur une glace d'environ 45 × 60 cm., munie de règles de verre sur les côtés pour empêcher l'écoulement. Une fois prise, elle a été séchée en 5 - 10 h. à l'aide d'un éventail, avec une humidité relative maintenue à 60 ± 2%. L'émulsion séchée forme une couche épaisse de 150μ, qui se sépare de son support de verre si on gratte un coin et si on la soulève. Elle est flexible, plane des deux côtés, tend à rester à plat, et adhère légèrement à elle-même sous une faible pression. Il est facile de la tailler en carrés de 5 × 5 cm. et d'empiler ceux-ci, pour former des blocs épais de 30 à 80 feuilles. Sous une pression estimée à 2 kgm. sur leur surface entière,

ces blocs ne présentent pas d'intervalles d'air occlus entre les feuilles, de plus de 5 à 10 $\mu$ , d'après les observations sur les trajectoires rapportées plus loin.

Après l'irradiation les feuilles sont séparées pour le développement. Celui-ci a lieu en les plongeant individuellement sans aucun support dans un b cher de 400 cm.<sup>3</sup> par exemple rempli   moiti  de r v lateur Eastman D8 dilu    deux volumes dans un volume d'eau maintenu   15 C.  $\pm$  1. Si l'on a soin d'agiter   mesure qu'on introduit les feuilles une   une au d but, puis d'agiter occasionnellement ensuite, les feuilles ne collent pas l'une   l'autre. On laisse agir le r v lateur pendant un temps compris entre 10 et 25 min., puis on arr te son action en le rempla ant par un bain d'arr t d'acide ac tique   3% qu'on laisse agir avec agitation pendant une minute; on fixe dans un b cher de 1000 cm.<sup>3</sup> rempli   moiti  de fixateur frais au thiosulfate de sodium avec un agitateur   palettes tournant   environ 100 tours par minute. Le fixage prend de 20   25 min., toute la surface d'une lame devient transparente   la fois, ce qui indique la double uniformit  de l' paisseur et de l'action du fixateur. On lave au moins 10   20 min.   l'eau courante en  vitant de perdre les feuilles dans le courant.

Si on laisse agir le r v lateur mentionn  jusqu'  production d'un voile donn , les trajectoires sont plus denses pour un traitement   15 C. qu'  25 C. La dur e normale de d veloppement est cinq minutes   25 C. et 12 min.   15 C. A 25 C. une feuille de 150 $\mu$  est d velopp e in galement, le centre l'est plus faiblement que la surface;   15 C., le d veloppement est uniforme dans toute l' paisseur d'une feuille de 150 $\mu$ , mais non d'une feuille de 250 $\mu$ .

Il faut  viter les fixateurs rapides au thiosulfate d'ammonium, qui d forment les feuilles, les font coller l'une   l'autre, et enl vent les marques   l'encre de Chine qui autrement r sistent parfaitement au d veloppement complet.

Quand on a s par  les feuilles l'une de l'autre avant le d veloppement, on a marqu  sur la face sup rieure de chacune deux rep res et un num ro d'ordre   l'encre de Chine, pour savoir comment elles s'ajustent l'une par rapport aux autres. Les feuilles  tant lav es   la fin du d veloppement on les impr gne quatre minutes d'une solution de glyc rine   10-20%, on les pose chacune face en l'air sur une vitre mince de 1 mm.  $\times$  75  $\times$  75 mm. par exemple, on chasse les bulles d'air et l'exc dent de liquide, et on fait s cher   60% d'humidit  relative devant un  ventail en 10   30 min. On peut aussi superposer sur une m me vitre deux feuilles successives qu'on ajuste comme elles se trouvaient plac es pendant l'irradiation.

Le probl me de la mise en co cidence apr s le d veloppement paraissait difficile, mais l'exp rience a montr  qu'il est tr s simple de superposer tr s exactement deux feuilles qui se touchaient au cours de l'irradiation. En effet, les faces rest es longtemps press es l'une contre l'autre portent, une fois d velopp es, de petits d fauts superficiels, taches de formes vari es visibles   l' il nu, dont certains se r p tent sur l'une et l'autre, par suite de quelques ph nom nes pseudophotographiques d s   la pression ou   d'autres causes.

En faisant coïncider ces petits défauts, on peut superposer les feuilles à mieux d'un millimètre près sur toute leur étendue. L'analyse interne des cartes d'exploration, pourvu qu'elles montrent quelques exemples nets de trajectoires ou de groupes de trajectoires passant d'une feuille à l'autre, permet de corriger l'écart résiduel de cette superposition.

Si l'humidité baisse excessivement, comme il arrive en hiver, la feuille d'émulsion peut se décoller, surtout si elle est voilée, si elle contient beaucoup d'argent réduit et si elle contient encore du thiosulfate de sodium à la suite d'un lavage incomplet. On peut la recoller en la laissant séjourner pendant une demi-heure dans une atmosphère saturée d'eau, par exemple à l'intérieur d'une cuvette de photographie garnie d'eau et couverte d'une vitre, où on supporte les plaques de verre au dessus du liquide. La feuille ainsi chargée d'humidité adhère au verre après tamponnement. Si le traitement est insuffisant, il faut tamponner la feuille avec une solution glycinée à 20-30% environ et reprendre le traitement en atmosphère saturée.

On constate que la feuille est plus étendue après qu'avant le développement. Une feuille épaisse de  $150\ \mu$  subit une dilatation linéaire de  $10 = 1\%$  selon toutes les directions comprises dans son plan, et par suite une dilatation en surface, de  $21\%$ . L'épaisseur se trouve de ce chef réduite de  $17.3\%$ ; le fixage réduit le volume à peu près à moitié, de sorte que l'épaisseur finale est environ  $41.4\%$  de l'épaisseur originale; mais l'épaisseur dépend aussi de l'humidité retenue, et peut par conséquent varier dans d'assez larges limites.

Des feuilles d'émulsion plus minces se distendent davantage; des feuilles de  $20\ \mu$  se déforment, se gondolent et se rident. Ces distorsions sont réduites par un traitement à l'alcool 40% à 90% après le lavage. Des feuilles plus épaisses se distendent moins.

On peut supposer pour expliquer ces phénomènes qu'il y a deux types de structures dans la feuille d'émulsion: de part et d'autre du centre, des régions superficielles très facilement déformables, dont l'épaisseur est approximativement la même quelle que soit l'épaisseur totale, et au centre une région plus résistante, qui compense l'effet des régions externes. Ces régions n'apparaissent peut-être que sous l'effet du développement, plus énergique en surface, mais il paraît probable que les régions superficielles sont d'avance différenciées par le séchage de la feuille d'un côté, par l'action du support de l'autre côté et par des phénomènes de tension superficielle. Ces feuilles et leur empilement sont illustrés Fig. 1.

## V. Intérêt de ces empilements

Une particule ionisant suffisamment qui traverse successivement plusieurs feuilles superposées, laisse une portion de trajectoire développable dans chacune. A l'examen, on pourra reconnaître ces portions de trajectoires qui s'ajustent bout à bout et reconstituer la trajectoire complète. Il est donc possible en principe d'examiner du début jusqu'à la fin chaque trajectoire dont on rencontre une portion dans la région centrale d'un empilement assez



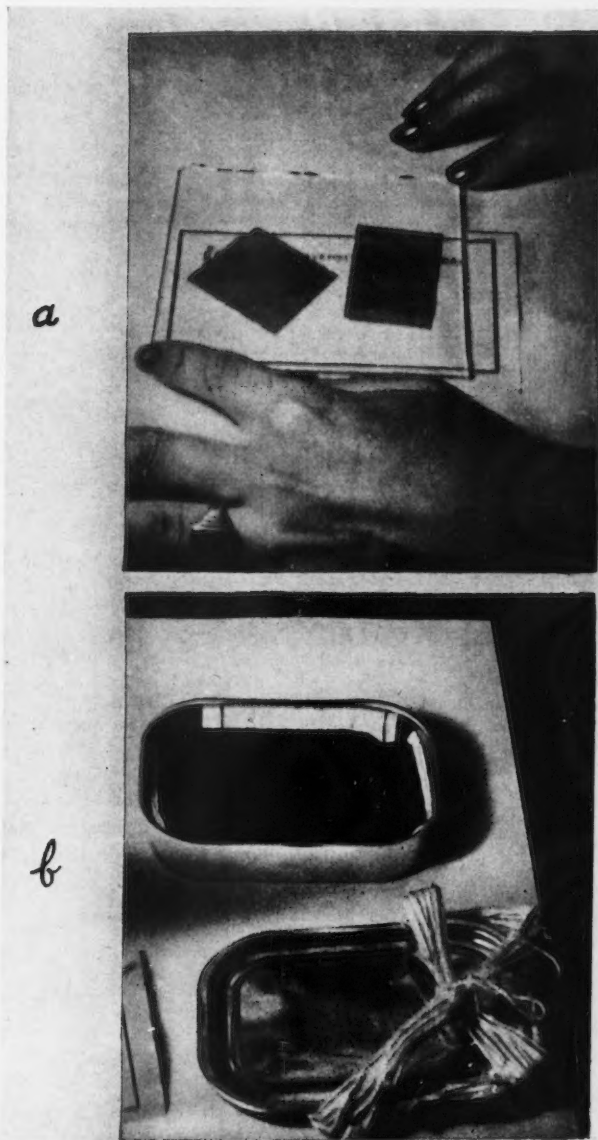


FIG. 1. (a) Feuilles d'émulsion sans support épaisses de  $150\ \mu$  environ, appliquées par une glace sur une étiquette. La transparence de l'émulsion permet de voir à travers. (b) Empilement de 80 feuilles d'émulsion sans support épaisses de  $150\ \mu$  chacune, enveloppé de papier noir et placé dans une boîte de fer-blanc. Le couvercle de la boîte et les ficelles qui la tiennent fermée sont visibles au premier plan.



volumineux, de sorte qu'on peut établir la nature, l'origine, l'énergie et les effets de cette particule; si on y aperçoit le centre d'une étoile de désintégration, il est possible de suivre chaque trajectoire jusqu'à la fin, et de mieux définir la réaction de désintégration et son énergie.

Sauf les petits intervalles d'air qui peuvent subsister entre les feuilles, les empilements constituent un milieu sensible ininterrompu dans tout leur volume, qui peut être en principe aussi épais et aussi étendu latéralement qu'on le veut. Les intervalles d'air paraissent être épais de 5 à 15  $\mu$  dans nos expériences, ce qui est l'équivalent, avec un pouvoir d'arrêt de 1600, d'une couche d'émulsion épaisse de 0.003 à 0.01  $\mu$ ; une particule même sous incidence rasante y perd très peu de son énergie, surtout si la pression atmosphérique est réduite.

Freier, Lofgren, Ney, Oppenheimer, Bradt et, Peters (27) utilisant des empilements de plaques sensibles, ont pu suivre d'une plaque à l'autre les trajectoires fortement ionisantes des particules lourdes de la radiation primaire. L'enregistrement des trajectoires dans leur cas était interrompu par le verre. Comme le verre mesure 1 mm. et l'émulsion 200  $\mu$  environ, on perd environ les 5/6 de la longueur des trajectoires dans le verre, où les particules dépensent une grande partie de leur énergie sans laisser de trace.

Yagoda (45, 46) en accolant deux plaques émulsion contre émulsion, a pu repérer dans une plaque la continuation des trajectoires commençant dans l'autre, et formant par exemple des étoiles radioactives. Barbour (5) a installé entre deux émulsions portées par un film d'éther cellulosique une feuille d'or de 50  $\mu$ , et il a pu observer des étoiles de désintégration cosmiques centrées dans l'or, par les branches inscrites de part et d'autre dans les émulsions avoisinantes. L'auteur (14, 16) a utilisé des méthodes de superposition avec deux couches sensibles et une couche uranifère interposée, pour enregistrer les paires de fragments de fission émis de part et d'autre par celle-ci, mais dans ce cas les trois couches restaient en contact permanent. Dans la méthode actuelle au contraire les feuilles d'émulsion sont séparées pour le développement.

On pourrait songer à employer des feuilles extrêmement épaisses, Fowler (25) a employé des plaques de 400  $\mu$ , et selon des renseignements personnels, Occhialini et Yagoda expérimentent avec des épaisseurs de 750 et de 1000  $\mu$  respectivement. Il paraît attrayant de n'avoir par exemple qu'une feuille de 1000  $\mu$  à manipuler et à examiner, au lieu de sept feuilles de 150  $\mu$  empilées. Cependant la durée du fixage augmente à peu près comme le carré de l'épaisseur, le développement doit être très lent si on veut que le centre d'une feuille très épaisse soit développé sans que la surface ne soit voilée complètement; le lavage et le séchage posent des problèmes analogues, de telle sorte que si une de nos feuilles de 150  $\mu$  peut être développée et prête à examiner en à peu près une heure, une feuille de 1000  $\mu$  selon Yagoda (47, 48), exige près d'une semaine. De plus la distance frontale des objectifs à immersion d'ouverture numérique 1.3 qu'on peut se procurer actuellement ne dépasse pas 500  $\mu$ , de sorte qu'on ne peut espérer examiner complètement dans les meilleures conditions optiques,

des feuilles d'émulsion mesurant plus de  $500\ \mu$  après soit plus de  $1000\ \mu$  avant développement.

Signalons aussi que le voile intervient pour former un milieu trouble de plus en plus épais à travers lequel on observe les trajectoires. Celles situées au fond de la feuille qu'on examine risquent de paraître floues si la feuille est très épaisse. Pour toutes ces raisons, l'empilement de feuilles d'épaisseur moyenne, de  $150$  à  $250\ \mu$  par exemple, développées et examinées séparément, paraît préférable et permet d'atteindre une épaisseur sensible aussi grande qu'on le désire.

## VI. Examen microscopique

Les feuilles étant sèches et posées individuellement ou superposées deux ensemble sur la même plaque de verre, ces plaques ont été examinées à l'aide d'une microscope 5LXK Spencer binoculaire, d'un objectif apochromat  $\times 90$  d'ouverture numérique 1.3 et d'oculaires compensés  $\times 5$  ou  $\times 12.5$ . L'éclairage est en lumière parallèle de type Köhler, avec une lampe Bausch & Lomb dite de recherche. L'immersion d'huile a été employée de part et d'autre de la plaque. Certaines régions des plaques ont été examinées avec un objectif sec d'ouverture 0.95 apochromat  $\times 47.5$ , qui a l'inconvénient d'être corrigé pour l'usage d'une lamelle couvre-objet, que nous n'employons pas.

L'examen avec cet objectif permet d'observer à la fois un champ quatre fois plus étendu en surface qu'avec l'objectif à immersion, et d'examiner une surface donnée quatre fois plus vite; mais l'objectif à immersion est nécessaire si on veut manquer le moins possible des trajectoires courtes et faibles. L'objectif sec semble révéler à coup sûr toutes les étoiles rencontrées sinon toutes les portions de trajectoires individuelles.

Après quelque temps, il est apparu, qu'il est nécessaire de noter toutes les trajectoires observées et de cartographier complètement les événements à mesure qu'ils sont rencontrés. Par exemple une portion de trajectoire rencontrée dans une feuille peut être la suite d'une branche d'une étoile intéressante dont le centre sera trouvé dans une feuille voisine. L'établissement d'une carte agrandie de la plaque peut se faire en notant les coordonnées sur les échelles divisées portées par la platine, et en les reportant sur un papier quadrillé, mais ce procédé n'est pas commode. Barbour (3, 4) a proposé et réalisé un pantographe mécanique agrandissant et traçant à volonté sur une feuille de papier les mouvements de la plaque sous l'objectif.

Une cartographie complète des trajectoires à l'intérieur d'une surface donnée d'une plaque est utile dans certaines études quantitatives. Elle peut permettre de reconnaître commodément des relations de proximité ou d'orientation entre des trajectoires ou des étoiles. Elle peut aider à retrouver un événement intéressant repéré sur la plaque. Champion, Powell et Occhialini (11, 38) ont employé de telles cartes pour l'étude des protons de recul dûs aux neutrons rapides, Barbour (2, 3, 4) et Franzinetti (26), pour des mesures de déviations dans un champ magnétique.

## VII. Pantographe optique (Fig. 2)

Dans les pantographes mécaniques les déplacements de l'objet sont répétés à l'échelle avec agrandissement ou réduction par un crayon ou une plume qui laissent une trace continue ou intermittente à volonté sur une feuille de papier. Dans notre appareil l'objet est la plaque observée sous le microscope, ses déplacements sont amplifiés 20 fois, la pointe traçante est remplacée par un faisceau lumineux qui projette sur le papier une tache lumineuse circulaire. Pour y laisser une marque permanente, on place soi-même un point à l'encre ou au crayon au centre de ce cercle. L'appareil ne comporte pas de tringles mobiles.

La seule pièce mobile est une lentille solidaire grâce à un bras léger en aluminium, du porte-objet du microscope. La lentille d'agrandissement marque illex de distance focale 51 mm., d'ouverture numérique  $f$  4.5, projette l'image d'une mire éclairée, placée en dessous. Cette mire est obtenue par un procédé photographique, elle est formée de cercles noirs concentriques sur un fond transparent. L'éclairage est assuré par une petite lampe de microscope Spencer. L'image agrandie 19 fois de cette mire se forme non loin de la lentille, sur un papier quadrillé au millimètres placé sur la table, grâce à une glace argentée de fond parallèle à la table, qui renvoie vers le bas les rayons lumineux sortant de la lentille. La lentille est à peu près au niveau de la platine du microscope ou légèrement plus haut, et sur le côté de celle-ci; la mire et son éclairage reposent sur la table et sur le papier quadrillé; le miroir est monté grâce à un bâti de fer d'angle, à des étriers et à des cales, à environ 45 cm. de la table. Comme les plans du miroir, de la table et du déplacement de la lentille, sont tous parallèles, les déplacements de la lentille sont reproduits à une échelle constante, qu'on utilise des rayons paraxiaux ou très obliques traversant la lentille.

Une reproduction à l'échelle  $\times 20$  est assurée en réglant la hauteur du miroir et en ajustant la mise au point de la mire chaque fois, jusqu'à ce qu'un déplacement de quelques millimètres lu sur la platine donne un déplacement vingt fois plus grand de la tache lumineuse sur le papier quadrillé. Il est possible de déplacer la platine et de revenir en plaçant la tache lumineuse au même point, à la même région de la plaque examinée, avec une précision de  $20 \mu$ . Les déplacements de la platine peuvent être mesurés sur le papier quadrillé avec une précision de  $1/200$  à  $1/500$ . Il n'est guère utile de chercher mieux parce que les quadrillages présentent des erreurs de cet ordre. Ce dispositif exige une platine de très bonne qualité puisque l'objet et la lentille au bout de son bras doivent exécuter des mouvements de pure translation sans rotation, il ne doit y avoir aucun ballotement perceptible des mouvements  $x$  et  $y$ . Le microscope employé s'est révélé excellent à ce point de vue. La tache lumineuse se déplace sur le papier grâce au jeu des symétries, de la même façon que le champ examiné paraît se déplacer sur la plaque. Si le cercle de la mire est de diamètre approprié, son image représente à l'échelle  $\times 20$  le champ examiné sous le microscope, en position relative et en grandeur aussi.

On peut tracer dans cette petite tache circulaire, par un agrandissement au carreau, les trajectoires et les autres détails visibles dans l'oculaire; en déplaçant la plaque examinée on peut au besoin continuer le dessin dans le cercle lumineux déplacé sur le papier, à l'aide des nouveaux détails visibles dans l'oculaire, et ainsi de proche en proche, jusqu'à ce qu'on ait figuré tous les détails intéressants que présente la plaque, trajectoires, repères, etc. Pour représenter une longue trajectoire rectiligne, on ajuste le microscope pour pointer des deux extrémités successivement, et on marque les points correspondants sur le papier, qu'on joint ensuite par une ligne au crayon.

### VIII. Cartographie et superposition

L'exploration des feuilles d'émulsion s'est faite en marquant d'abord à l'encre de Chine des rectangles  $12 \times 24$  mm. environ, placés sur chacune pour délimiter aussi exactement que possible les régions qui étaient superposées au cours de l'irradiation.\* La plaque est alors installée sur la platine, une feuille

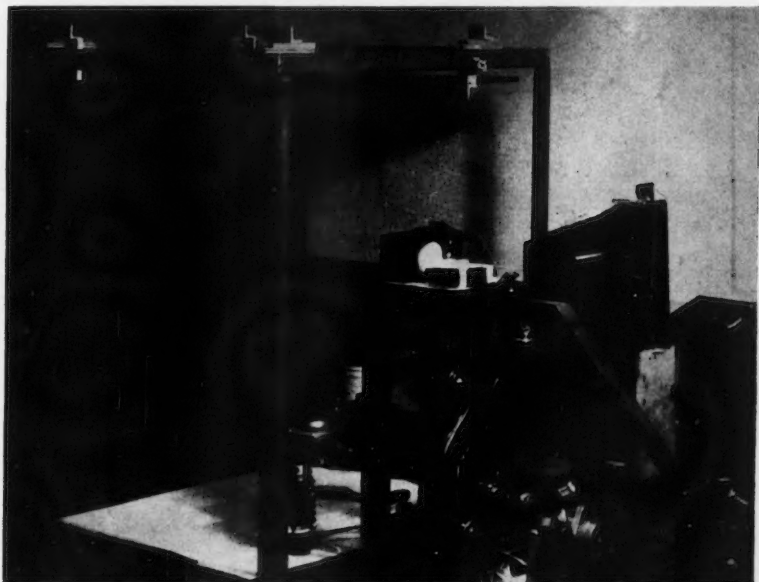


FIG. 2. Pantographe optique et appareil de photomicrographie continue installés sur le microscope 5LXK. De droite à gauche: lanterne éclairant le microscope; support avec la boîte noire renfermant le film, qui est mû par un moteur synchrone caché par la boîte. L'arbre entraînant le film dépasse en avant et entraîne un compte-tours. Au premier plan, moteur synchrone attaquant le mouvement  $x$  de la platine. Platine tournante  $\Theta'$  et seconde platine  $x' y'$ . La lampe servant pour la photométrie est représentée allumée. On voit le miroir à  $45^\circ$  surmontant l'oculaire et la lentille divergente sur son support, qui est poussée au dessus de ce miroir pour l'observation. Entre les quatre pattes du bâti du pantographe à gauche, on voit la lentille au bout de son bras solidaire du porte-objet du microscope et la lampe qui éclaire la mire placée sous cette lentille. La bâti porte un miroir posé à plat, la table porte un papier quadrillé qui reçoit l'image de la mire formée par la lentille après une réflexion sur le miroir.

\*L'encre de Chine sèche s'enlève facilement avec un petit tampon imbibé d'ammoniaque à 5-10%.

de papier quadrillée au millimètres de  $450 \times 600$  mm. est installée sur la table entre les pattes du pantographe, et ajustée en position et en orientation. On pointe les coins du rectangle sous l'objectif et on les marque sur le papier. On explore ensuite la région rectangulaire par bandes horizontales d'ordonnée  $y$  constante, en partant d'un bord du rectangle et en arrêtant quand on aperçoit dans l'oculaire l'autre bord. On change l'ordonnée d'une quantité à peu près égale au diamètre du champ et on recommence suivant ainsi une ligne brisée analogue à une grecque. Grâce à l'aide du pantographe il est facile de marquer les régions déjà examinées, d'exécuter les déplacements  $y$  et  $x$  requis, et si on s'écarte d'une valeur de  $y$  pour examiner d'un côté ou de l'autre, de revenir ensuite au même point pour reprendre l'exploration systématique. On dessine les trajectoires, les étoiles et les repères à mesure qu'on les rencontre.

Une exploration complète d'un tel rectangle de  $2.88 \text{ cm.}^2$  peut se faire en une journée de travail si on s'y applique exclusivement, soit en cinq ou six heures, avec l'objectif à immersion  $\times 90$ . L'objectif sec  $\times 47.5$  d'ouverture 0.95 réduit ce temps par un facteur 3 ou 4. Il semble qu'il révèle toutes les étoiles rencontrées, mais seulement une proportion d'environ 60% des trajectoires isolées tandis que l'objectif à immersion révèle environ 90% de ces mêmes trajectoires.

Si deux feuilles sont superposées pour l'examen sur la même plaque l'exploration de la surface du rectangle est presque deux fois plus lente, parce qu'il faut explorer le champ en profondeur et que la profondeur est double. La superposition ne fait pas gagner beaucoup de temps au cours de l'exploration. Elle est surtout avantageuse en ce qu'elle permet de chercher immédiatement dans une feuille la continuation d'une trajectoire aperçue dans l'autre, et qui s'y dirige. Quand la superposition a été bien restituée, les deux portions de la même trajectoire peuvent se trouver à une distance de 50 ou 100  $\mu$ . On peut alors se rendre compte de la distorsion relative des deux feuilles, mesurée par la variation entre la distance précédente pour des trajectoires traversant les deux feuilles en diverses régions du rectangle tracé sur celles-ci. La distorsion peut atteindre  $\pm 300 \mu$  dans de mauvaises conditions, par exemple quand il a fallu beaucoup manipuler les feuilles pour les fixer à la plaque. Au contraire elle est de  $\pm 100 \mu$  dans de bonnes conditions. Quand on trace sur le même papier quadrillé les cartes de deux feuilles superposées, il est avantageux d'employer des crayons durs de couleurs différentes, par exemple bleu pour la feuille du bas et rouge pour celle du haut.

Expérience faite la superposition de plus de deux feuilles ne paraît pas très attrayante: la durée de l'exploration par unité de volume ne dépend pas beaucoup de l'épaisseur, et les trajectoires situées dans le bas deviennent moins nettes par suite du voile interposé.

### IX. Efficacité de la méthode

Si on compare les cartes de plusieurs feuilles successives, on retrouve sur chacune au moins quelques portions de trajectoires se faisant suite. Si on

cherche à l'endroit d'une feuille là où doit passer une portion de trajectoire qui a échappé à une première exploration, il arrive souvent qu'on la trouve à ce moment. Une exploration même attentive avec l'immersion n'est donc pas parfaitement efficace. On peut estimer par de telles observations que son efficacité est voisine de 90%.

A l'heure actuelle, 13 feuilles, depuis celle du sommet No. 1 jusqu'au No. 13 ont été examinées au moins en partie. 31 centres d'étoiles ont été observés et notés, et environ 300 portions de trajectoires.

L'efficacité de la méthode serait de 100% s'il était possible de trouver le début, la fin et toutes les parties intermédiaires d'une trajectoire quelconque dont on aperçoit une partie. L'efficacité en réalité n'est pas 100%. Quand il est impossible de trouver dans une feuille la suite d'une trajectoire qui s'y dirige, il y a généralement trois causes évidentes: 1°) la trajectoire est trop

TABLEAU I

ÉTOILES À 15 BRANCHES CENTRE DANS LA FEUILLE 5. (FIGS. 3 ET 4.)  
(On n'a pas cherché la suite des trajectoires 4, 7, 10 et 15 dans la feuille 8.)

Branche				Feuille No.			
No.	Nature	Complète	Incomplète	4	5	6	7
1	$\alpha$	✓			Début	Fin	
2	$\beta$	✓			Début et fin courte		
3	$\beta$	✓			Idem		
4	$p$		✓		Début	Suite	Suite
5	$\alpha$	✓			Début	Fin	
6	$p$	✓		Fin	Début		
7	$p$		✓		Début	Suite	Suite
8	Recul	✓			Début et fin		
9	$\alpha$ ou $T$	✓		Fin	Début		
10	$p$		✓		Début	Suite	Suite
11	$p$	✓			Début	Suite	Fin
12	$p$	✓			Début	Fin	
13	$\alpha$		✓	Suite invisible sans doute arrête entre les deux surfaces sensibles			
14	$p$		✓		Début	Suite invisible trop faible	
15	$p$		✓		Début	Suite	Suite
Total 15		9	6				



TABLEAU II  
ÉTOILES LIÉES CENTRES DANS LES FEUILLES 2 ET 4 (FIGS. 5, 6, 7a ET 13)

Branche				Feuilles No.					
No.	Nature	Com- plète	Incom- plète	1	2	3	4	5	6
1	$\beta$	✓					Début et fin		
2	$p$		✓	Suite continue dans l'air	Suite	Suite			
3	$\alpha$	✓					Début	Suite	Fin
4	$\alpha$	✓					Début	Fin	
5	$p$		✓				Début	Suite invisible trop faible	
6	$p$	✓					Début	Fin	
7	Recul	✓					Début et fin		
8	$\beta$	✓					Début et fin		
9	$\beta$	✓					Début et fin		
10	$p$	✓					Début	Fin	
11	$p$	✓			Début probablement	Suite	Fin probablement		
12	$p$		✓		Début	Suite invisible trop faible			
13	$p$		✓		Début	Idem			
14	$\alpha$	✓			Début et fin				
15	$\alpha$	✓			Début	Suite	Fin		
16	$p$		✓	Suite continue dans l'air					
Total 16		11	5						

faible, c'est-à-dire composée de grains très fins et trop espacés. On ne la discerne pas du voile continu environnant. Si un point d'une trajectoire très faible est donné, par exemple son début dans une étoile ou sa fin, il est plus facile de reconnaître l'alignement des grains successifs et de la suivre. 2°) Le voile superficiel, des défauts présents dans la surface ou dans la masse, et le



voile continu dans l'épaisseur de la feuille peuvent masquer une trajectoire faible. 3°) La trajectoire peut être si courte qu'elle se confond avec le voile superficiel, ou encore, elle peut s'être arrêtée dans la couche d'air interposé.

L'efficacité de la méthode peut être évaluée avec précision dans le cas de deux phénomènes spécialement étudiés à ce point de vue: une étoile à 15 branches et une étoile double renfermant 16 branches en tout. (Tableaux I et II, Figs. 3 et 5.)

Sur les 31 branches que présentent ces étoiles, il a été possible d'en suivre 20 d'un bout à l'autre; en l'absence du procédé de superposition seulement 9 des trajectoires seraient visibles en entier, de sorte que l'efficacité passe de 9/31 à 20/31, ou de 29 à 64.5%. Pour évaluer correctement la signification de ce résultat il faut préciser que sur les 11 trajectoires incomplètes, 2 se continuaient dans l'air au dessus de l'empilement, dans 4 cas le début même était si faible qu'on ne pouvait le reconnaître qu'avec peine, pour quatre autres on n'a pas cherché la suite, et dans le cas d'un rayon  $\alpha$ , il paraît clair qu'il s'est arrêté entre les surfaces sensibles.

Si on définit l'efficacité de la méthode comme étant la proportion des trajectoires commençant dans une étoile, et vues complètement on peut l'appeler *efficacité globale*, et elle vaut 64,5% dans les exemples actuels. Si on la définit comme étant la probabilité de trouver la suite d'une trajectoire dans la feuille voisine vers laquelle elle se dirige, il est clair qu'elle pourra être plus élevée que selon la définition précédente, puisque pour suivre une trajectoire jusqu'à la fin, il faut au moins dans certains cas observer plus qu'une fois son passage d'une feuille à l'autre.

TABLEAU III  
EFFICACITÉ LOCALE DE LA MÉTHODE

Dans la feuille No.	Nombre de portions de trajectoires	Se dirigeant vers la feuille No.	La continuation est observée dans cette dernière feuille pour le nombre suivant de trajectoires
1	2	2	2
2	2 5	1 3	2 3
3	3 3	2 4	3 3
4	3 7	3 5	3 6
5	6 11	4 6	6 9
6	9 5	5 7	9 5
7	5 4	6 8	5 0 pas cherché
Cas possibles:	65	Cas observés:	56

Cette *efficacité* qu'on peut appeler *locale*, pour la distinguer de la précédente, peut se calculer pour le même exemple de ces trois étoiles, et vaut alors 56/65 ou 86% (Tableau III).

## X. Résultats

### (1°) QUELQUES GRANDES ÉTOILES

En l'absence de données statistiques nombreuses, nous nous bornerons à discuter quelques étoiles plus intéressantes, à titre d'exemple, et leurs bilans d'énergie approximatifs.

Dans l'établissement de ces bilans, on n'a pas cherché à mesurer les parcours avec une grande précision. De telles mesures feraient intervenir la dilatation de l'émulsion dans le plan horizontal  $x, y$  et la contraction verticale suivant  $z$ . Une fois la feuille fixée sur une lame de verre, les déformations  $x$  et  $y$  ne changent plus, tandis que selon la teneur en glycérine et selon l'humidité, l'épaisseur peut changer. Il faudrait aussi tenir compte de l'épaisseur d'air interposé entre les feuilles, calculée pour un cas particulier dans la section XII. Enfin il faudrait tenir compte des distorsions non-linéaires qui se produisent par endroits.

#### *Étoile à 15 branches (Figs. 3 et 4, Tableau I)*

Elle comprend un noyau de recul, 3 rayons  $\alpha$ , 1 rayon  $\alpha$  ou un triton, 7 protons et  $2\beta$  positifs ou négatifs. En supposant que toutes ces particules sont émises, la masse de ces particules visibles, augmentées de 9 neutrons hypothétiques, est (31 ou 32 + recul), et leur charge est (15 ou  $14 \pm 2$  + recul), ce qui indique clairement la désintégration d'un noyau Ag ou Br. Le noyau de recul doit être très lourd et très chargé puisque son ionisation décroît rapidement à mesure qu'il s'éloigne du centre de l'étoile.

L'énergie visible dans les trajectoires se totalise à 150 MV; cet estimé approximatif est basé sur une évaluation du parcours et de l'énergie des trajectoires complètes, et des trajectoires incomplètes, en particulier celle no. 14 qui ionise très peu et doit posséder une énergie de 50-60 MV. Il faut ajouter l'énergie de neuf neutrons environ, mettons 90MV, et l'énergie de liaison de 13 particules visibles plus lourdes qu'un  $\alpha$  et de 9 neutrons, mettons  $8 \times 22$  ou 176 MV, pour obtenir l'énergie fournie par la particule incidente, soit au total 400 MV environ.

#### *Étoiles liées (Figs. 5, 6, 7a, 13, Tableau II)*

Sur 31 étoiles trouvées 4 forment deux paires d'étoiles liées. Dans un cas la trajectoire intermédiaire est courte et relie deux étoiles visibles dans la même feuille, ayant par ailleurs 2 et 4 branches respectivement. Le second cas est discuté ici en détail: les étoiles liées ont leurs centres dans des feuilles distinctes nos. 2 et 4, séparées par une feuille intermédiaire. La trajectoire

*N.B. Les photographies des trajectoires ne sont pas retouchées.*

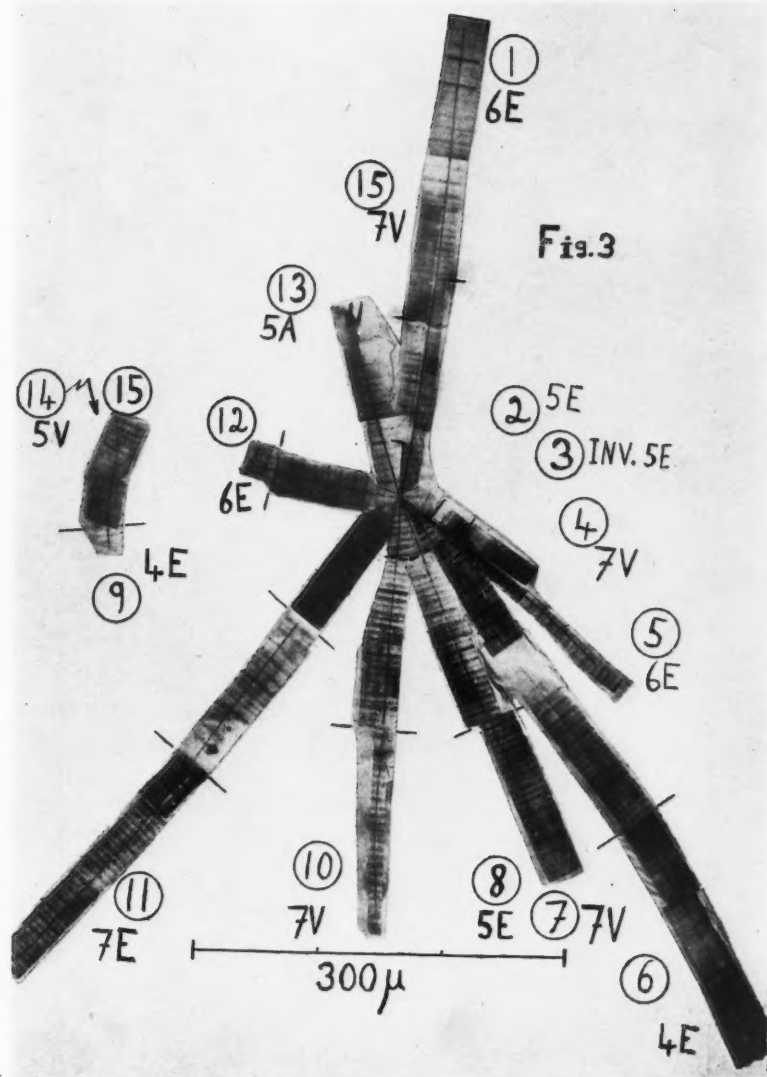


FIG. 3. Etoile à 15 branches centrée dans la feuille 5. Photo obtenue à partir de 26 négatifs pris dans les feuilles 4, 5, 6 et 7, qui totalisent une épaisseur de 600 μ environ. Le No. des trajectoires est placé dans un cercle. Les autres Nos. sont ceux des feuilles. E = fin d'une trajectoire dans l'épaisseur de l'émulsion; A = trajectoire interrompue à la surface supérieure (air) d'une feuille; V, à la surface inférieure (verre) d'une feuille. Inv = non reproduite sur la figure. Des traits transversaux marquent le passage d'une feuille à l'autre. Les trajectoires 9 et 14 sont figurées à part à cause de l'encombrement au centre de l'étoile.

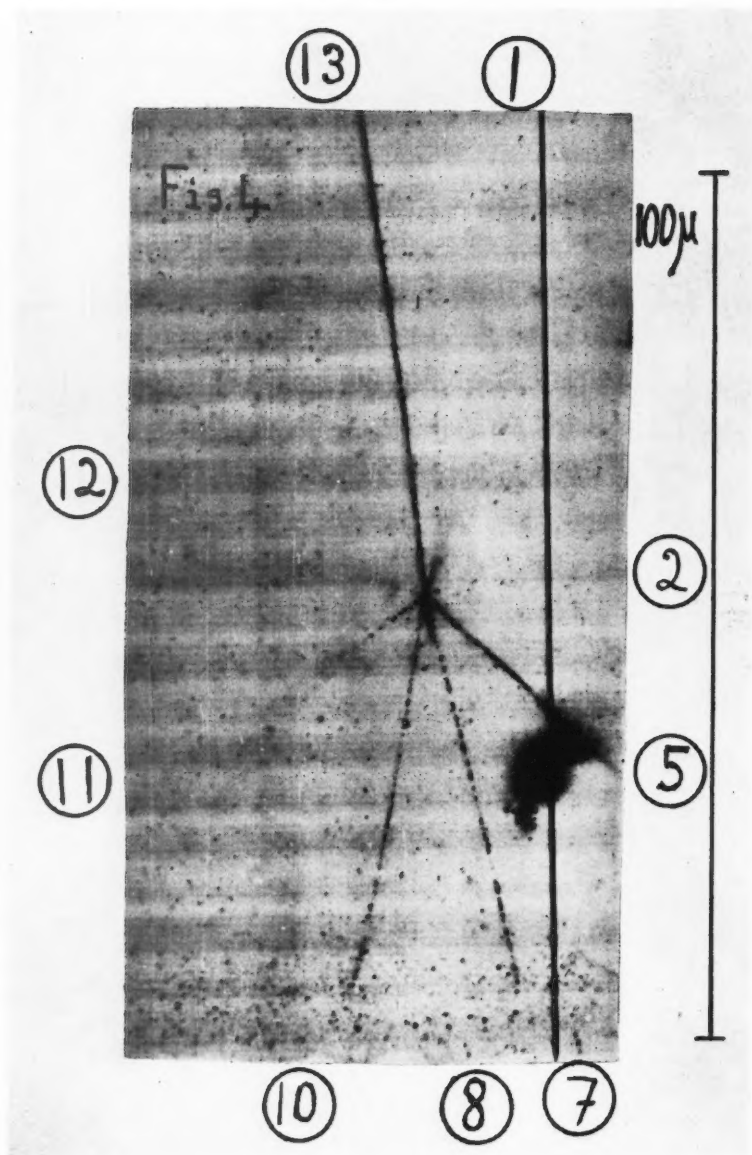


FIG. 4. Vue partielle du centre de l'étoile précédente tirée d'un seul négatif illustrant la possibilité de photographier deux trajectoires comme 7 et 10, voisines et également inclinées.

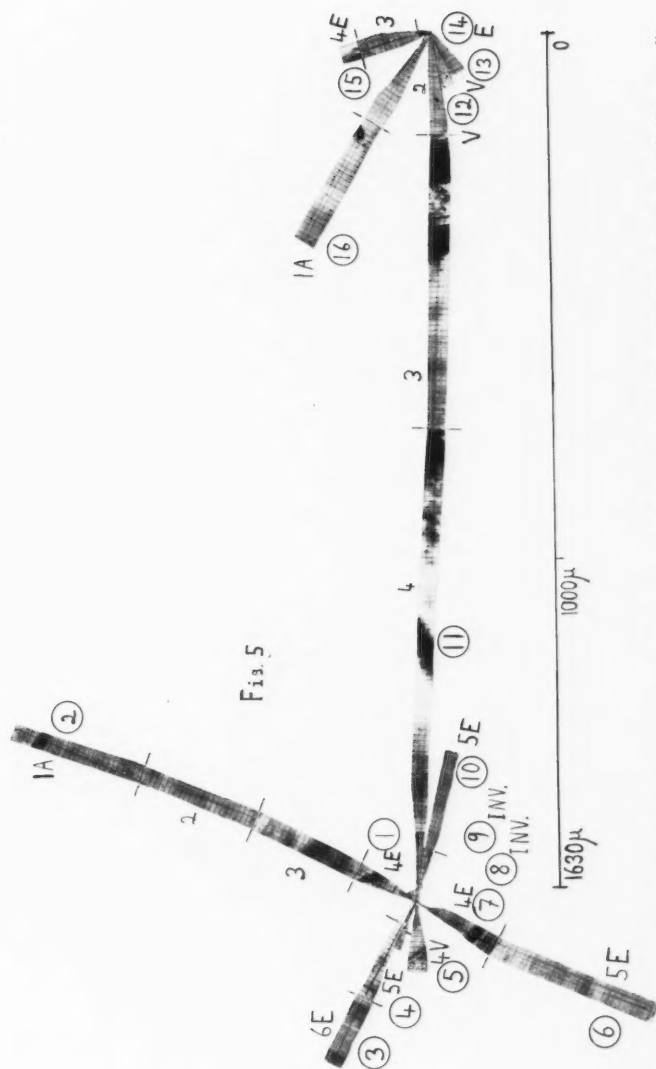


Fig. 5. Deux étoiles couplées centres dans les feuilles 2 et 4. Le faible grossissement nécessaire pour la reproduction complète du phénomène fait qu'il est difficile d'apercevoir les grains des trajectoires surtout celle No 11. Notation comme pour la Fig. 3. Le voile à la surface supérieure des feuilles forme des marques noires visibles surtout le long de la trajectoire No 11. L'ensemble du phénomène occupe les feuilles 1 à 6 soit une épaisseur totale d'environ 700 μ. Il est reproduit à partir de 21 négatifs.

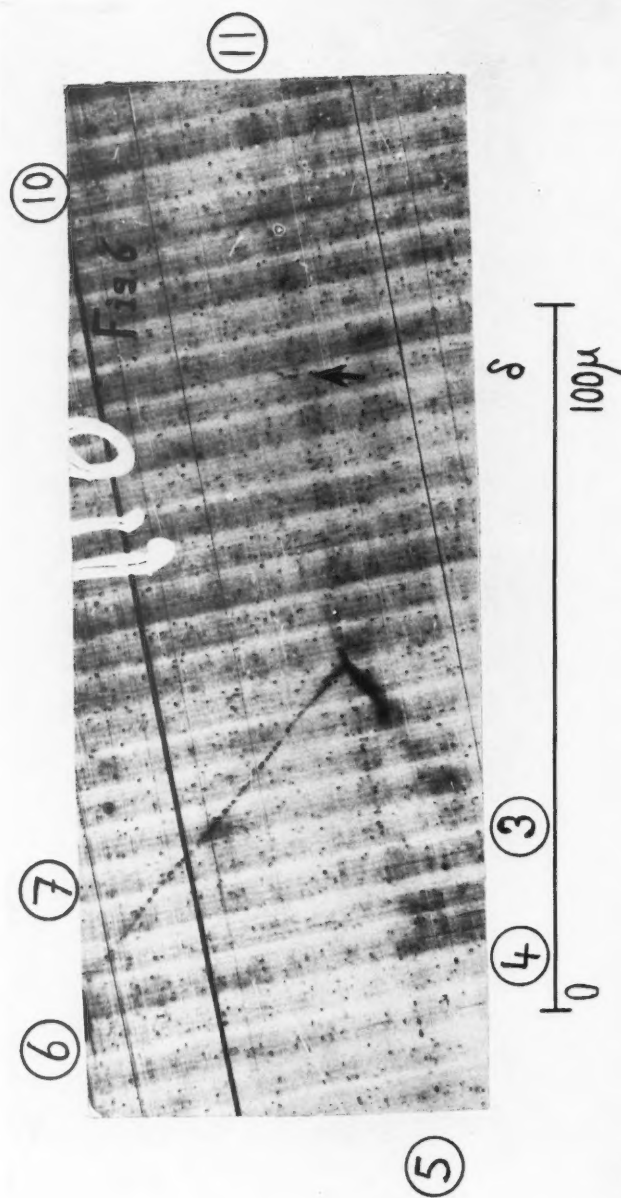


FIG. 6. Vue partielle du centre d'une étoile de la Fig. 5 dans la feuille 4, tirée d'un seul négatif, illustrant le proton No 11 d'énergie  $y = 200$  MV et le No. 5 d'énergie 50 MV environ, et le début d'un rayon  $\delta$  le long du No 11.

intermédiaire presque horizontale mesurait  $1480 \mu$  dans l'émulsion avant développement ou environ 296 cm. d'air équivalent, avec un pouvoir d'arrêt de 2000. On a tenu compte d'un allongement de 10% des dimensions horizontales de l'émulsion au cours du développement. Ainsi 2 sur 29 ou  $7 \pm 6\%$  des événements trouvés sont des paires d'étoiles. Ces phénomènes doivent être assez fréquents et la méthode de superposition aidera évidemment à les trouver et à étudier leur fréquence et les réactions qu'elles représentent.

Sur la trajectoire intermédiaire que nous admettons être un proton, la densité paraît augmenter légèrement quand on se rapproche de l'étoile dans la feuille 2; l'étoile dans la feuille 4 aurait donc précédé l'autre. Cependant il peut y avoir des différences entre le développement, l'épaisseur et les propriétés exactes des émulsions aux deux extrémités de cette trajectoire, qui se trouvent dans des feuilles différentes, la feuille 2 étant plus mince, de sorte que cette comparaison n'est pas très sûre. D'autre part si la particule intermédiaire était responsable de la désintégration dans la feuille 2, on s'attendrait à observer dans l'étoile qui s'y trouve au moins quelques branches se dirigeant dans le même sens, ce qui n'est pas le cas.

Il semble donc que la première désintégration est celle de la feuille 2. On voit 4 protons et  $2\alpha$  émis ce qui s'accorde avec l'hypothèse d'une particule incidente neutre agissant sur un noyau d'oxygène. L'étude de l'autre étoile permet d'évaluer l'énergie  $\gamma$  du proton émis dans cette première désintégration, qui va causer la seconde désintégration.

La seconde étoile reçoit ce proton, émet 4 protons, et  $2\alpha$ , un recul et  $3\beta$ . La masse apparue est donc  $(11 + \text{recul})$ , la charge apparue est  $(7 + \text{recul} \pm 3)$ . Il ne nous est donc pas encore possible d'évaluer avec précision la masse et la charge du noyau de recul à l'aide du pouvoir discriminateur excellent de l'émulsion employée, cependant ce noyau paraît être ici assez lourd pour exclure la désintégration d'un noyau léger, et l'attribuer à un noyau lourd Ag ou Br.

Une évaluation approximative de l'énergie visible dans cette seconde étoile donne le bilan suivant:  $2\alpha$  30MV,  $3p$  25MV, un recul 10MV, un proton  $x$  MV. Il faut probablement ajouter l'énergie de 5 neutrons émis ou 30MV environ, et l'énergie de liaison de 11 particules émises, en excluant le proton entrant et 1 proton sortant soit  $11 \times 8 = 88MV$ , pour trouver l'énergie  $\gamma$  de la particule incidente soit:  $\gamma = 65 + x + 30 + 88 = 183 + x$  MV. Le proton d'énergie  $x$  est le No 5, il ionise si peu qu'on ne peut trouver sa suite dans la feuille voisine, et son ionisation paraît comparable sinon inférieure à celle de la particule incidente. Il faut donc que  $x$  et  $\gamma$  soient des énergies très grandes pour lesquelles le pouvoir ionisant est comparable. Si on pose  $x = 50MV$ ,  $\gamma$  vaut 230 MV environ. Un proton d'une telle énergie sur un parcours de  $1500 \mu$  ne perd que 3 ou 4 MV.

Il est intéressant de noter que par conséquent notre émulsion est sensible à un proton de 200MV ou un pouvoir ionisant de 4 kv./cm. d'air équivalent;



elle doit par conséquent permettre l'enregistrement de deutérons de 400MV, de mésons de 30MV, d'électrons de 100 kv., et de rayons  $\alpha$  de plus de 2000 MV; ces limites sont établies à l'aide de l'article de Webb (42).

Nous pouvons maintenant calculer le bilan d'énergie dans l'étoile de la feuille 2: il y a émission du proton d'énergie  $y$  et de 2 protons d'énergie  $x'$  et  $x''$  qui semblent ioniser encore moins que le proton  $y$ , et dont il est impossible de trouver la suite dans la feuille suivante tandis qu'on y a trouvé la suite de la trajectoire  $y$ . Il est vrai que ces trajectoires sont plus obliques que  $y$ , ce qui a pu nuire à la recherche de leur prolongement, mais il ne paraît pas exagéré d'assigner à  $x'$  et à  $x''$  une valeur de 200MV, et le bilan pour les particules visibles est  $y + x' + x'' + 1$  proton 20MV,  $1 \alpha$  0.5MV,  $1 \alpha$  15MV = 635.5MV; il faut ajouter l'énergie de 4 neutrons, si on suppose qu'elle est égale à l'énergie des protons émis, elle vaut 620MV; et aussi l'énergie de la réaction  $O16 \rightarrow 2 \alpha + 4p + 4n$ , qui requiert 70.2 MV; la particule incidente a donc dû fournir une énergie dépassant 1315MV. Il est remarquable que sur une si grande énergie il ne se trouve que 15.5MV disponibles pour les rayons  $\alpha$ . Si on suppose que l'ordre des désintégrations est inversé, on obtiendrait une énergie du même ordre de grandeur pour la particule incidente.

Il n'est pas impossible qu'un certain nombre des particules que nous avons admis être des protons soient en réalité des deutérons. En tenant compte de cette incertitude, l'erreur maximum sur le bilan énergétique de 1315MV est de l'ordre de  $\pm$  600MV. Si la particule intermédiaire est un deutéron au lieu d'un proton, son énergie reste 200MV environ, mais les limites supérieures des énergies des diverses particules laissant encore une trace visible, qu'on peut tirer deviennent à peu près la moitié de celles calculées plus haut soit au moins  $\beta$  50KV, méson 10MV,  $p$  100MV,  $\alpha > 1000$  MV.

## 2° DÉSINTÉGRATION $C12 \rightarrow 3\alpha$ (FIG. 7B)

Une étoile sensiblement symétrique possède trois branches attribuables à des rayons  $\alpha$  de 1 à 4 MV. Les parcours sont incompatibles avec l'hypothèse d'une étoile radioactive, et le phénomène s'interprète naturellement comme la désintégration cosmique d'un noyau de carbone; les trois branches sont presque coplanaires et montrent une légère composante du moment total vers le bas, ce qui s'accorde avec l'hypothèse d'une particule incidente dirigée vers le bas et ayant une énergie de l'ordre de 20 MV avec un moment cinétique relativement peu considérable.

## 3° ÉTOILES SIMPLES A UNE SEULE BRANCHE DÉVELOPPÉE

Nous avons observé quelques trajectoires de protons entièrement isolées commençant dans l'émulsion. Nous avons de plus observé quatre étoiles très simples ne comprenant qu'une branche développée seule visible à première vue, et un noyau de recul très court n'apparaissant qu'à une observation attentive, qui est discernable grâce au grain très fin de nos émulsions et à leur pouvoir discriminatoire. On ne pourrait probablement pas voir le recul dans les

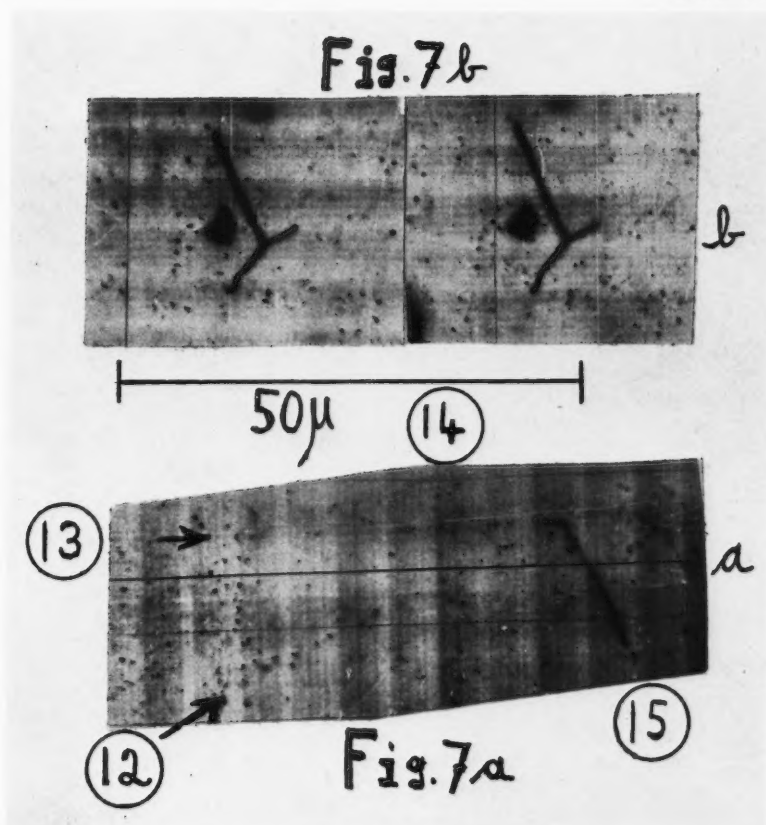


FIG. 7. (a) Vue partielle d'une étoile de la Fig. 5 dans la feuille 2, illustrant deux protons de grande énergie Nos. 12 et 13, et deux rayons  $\alpha$  Nos. 14 et 15. (b) Étoile à trois branches, désintégration symétrique  $C12 \rightarrow 3\alpha$ . Un phénomène, deux négatifs différents.

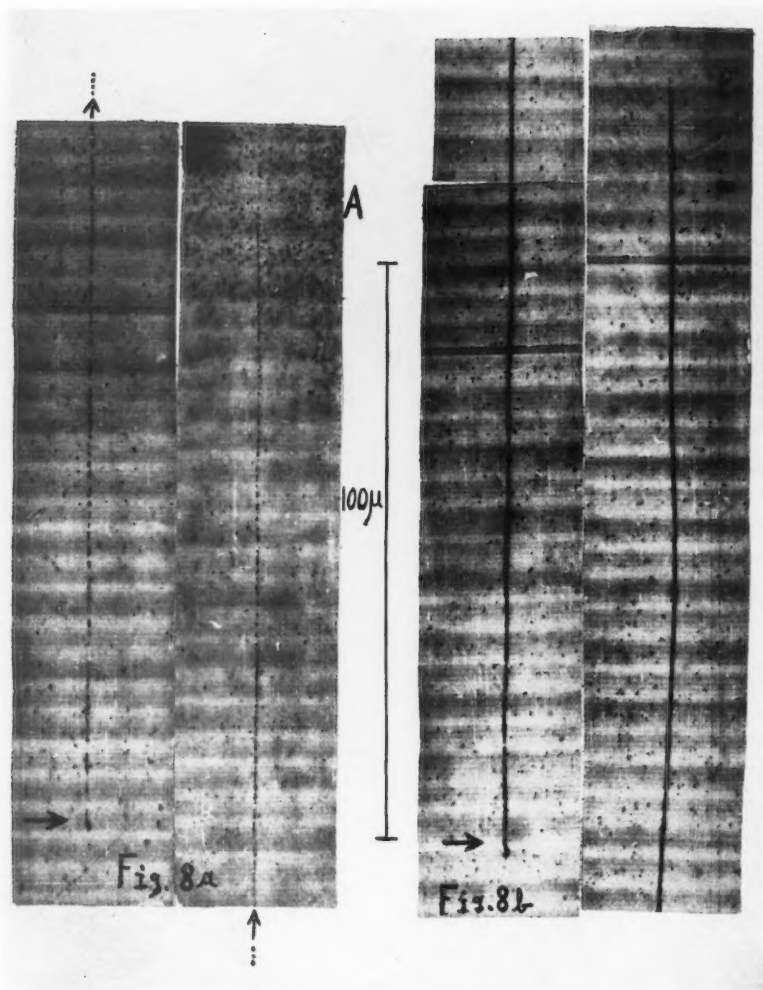


FIG. 8. Etoiles simples. (a) (R-p) début à gauche, fin à droite de la partie visible dans une feuille d'émulsion, longueur totale visible 660  $\mu$ . (b) (R- $\alpha$ ) reproduction complète.

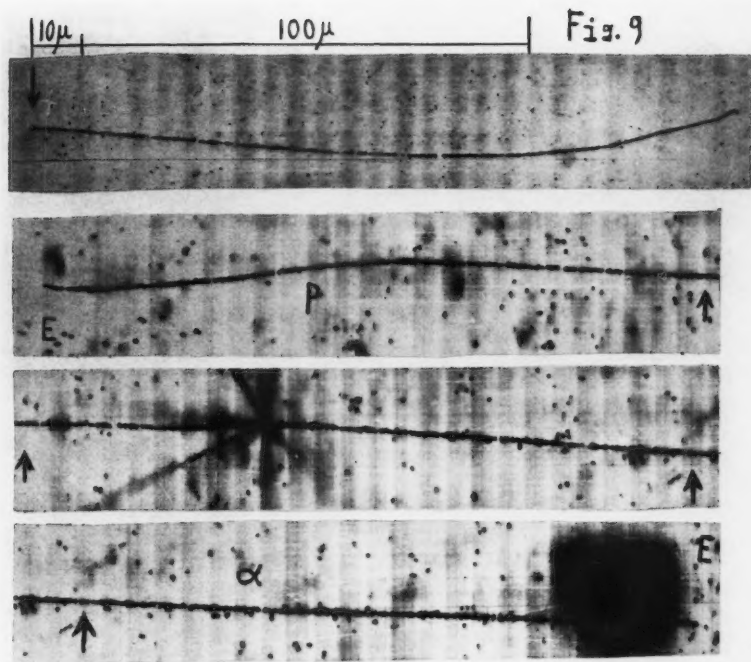
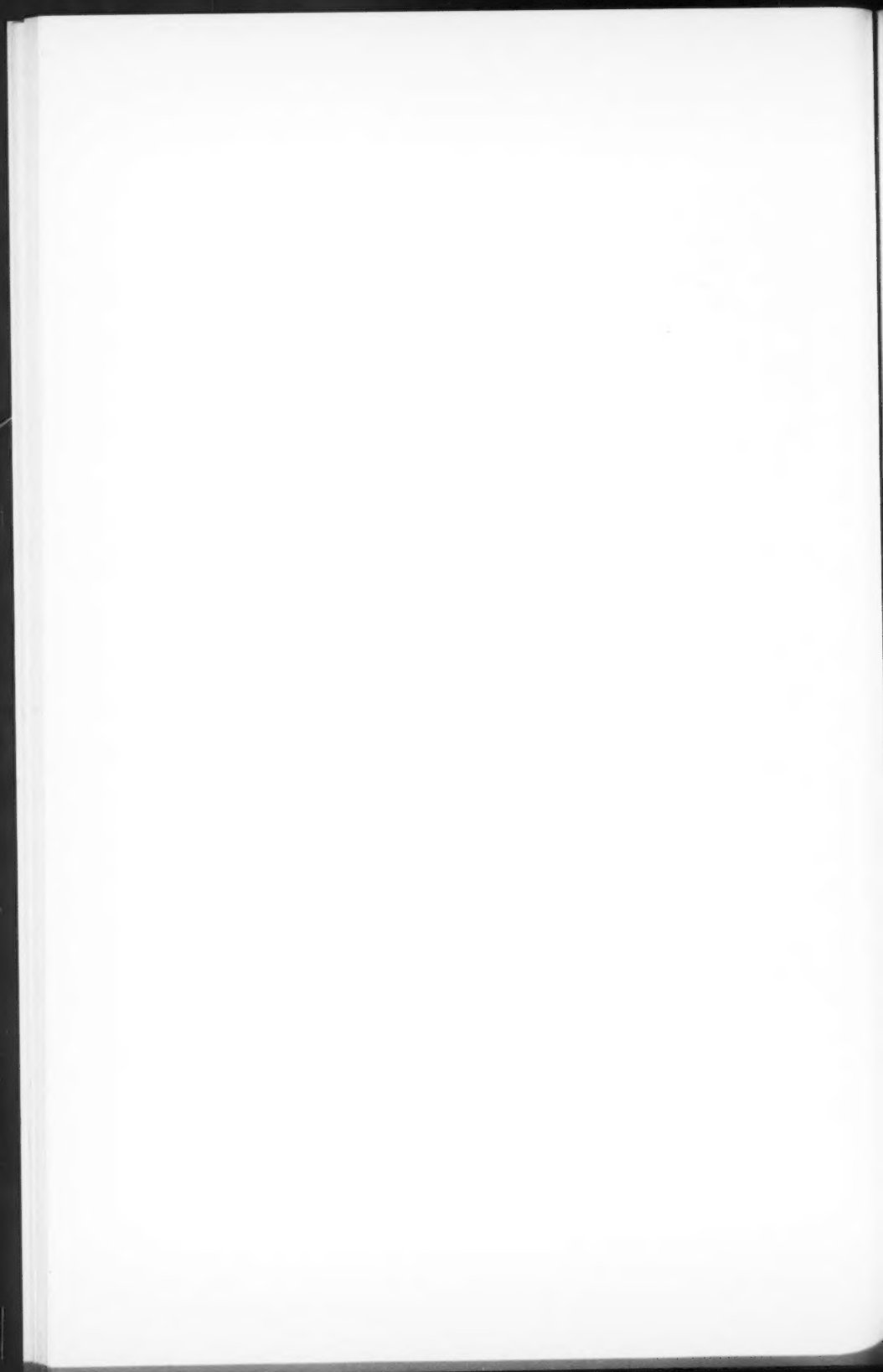


FIG. 9. Etoile simple (R - T) reproduction complète. Dans l'émulsion NTB3 étoile reproduite en partie,  $p$  et  $\alpha$  probablement, montrant la différence de taille des grains qui sont deux ou trois fois plus petits dans notre émulsion.



émulsions courantes du commerce parce que leur grain est trop gros. Ces étoiles simples semblent assez fréquentes puisqu'on en a observé 4 sur 31 ou  $13 \pm 7\%$ . Dans chaque cas la trajectoire longue est sensiblement horizontale et le recul approximativement; les trajectoires sont toutes complètes dans la même feuille d'émulsion, sauf dans un cas, où un proton quitte l'émulsion vers le haut (Tableau IV).

TABLEAU IV  
ÉTOILES SIMPLES

N°	Fig. n°	Particule légère			Recul
		Nature	Parcours dans l'émulsion avant développement	Energie	Parcours dans l'émulsion avant développement
1	16 et 17	Méson	160 $\mu$	2 MV	0.19 $\mu$
2	8a	Proton	600 $\mu$ incomplet	> 15 MV	0.13 $\mu$
3	9	Triton	135 $\mu$	6 MV	0.05 $\mu$
4	8b	Alpha	220 $\mu$	22 MV	0.16 $\mu$

Il est naturel de supposer que ces étoiles simples forment une classe ayant une explication commune. Le fait qu'elles sont sensiblement comprises dans un plan horizontal suggère deux hypothèses alternatives sur le rayonnement incident, rendues nécessaires par des considérations de symétrie: 1° il est incident verticalement et produit l'éjection des particules à angle droit; 2° il est horizontal et produit l'éjection de la particule légère dans sa direction même.

La faible énergie des particules visibles et la simplicité du phénomène suggèrent l'action d'une particule de *faible énergie* sur un noyau léger. Dans ce cas il y aurait peu ou pas de particules neutres ou faiblement ionisantes émises en plus de celles qui laissent des trajectoires visibles, de sorte que la direction de ces dernières, à cause de la conservation de la quantité de mouvement, indiquerait celle de la particule incidente: une particule incidente de faible énergie viendrait donc horizontalement.

Si la radiation incidente possède une *grande énergie*, on s'attendrait à trouver une énergie plus grande que quelques MV dans les produits de la désintégration. Cependant on peut supposer qu'elle est incidente verticalement, qu'elle produit à angle droit l'émission des particules visibles, et vers le bas, d'un certain nombre de particules ionisant trop peu pour laisser ici leur trace, qui assurent la conservation de la quantité de mouvement.

Baldwin et Klaiber (1) ont observé des étoiles simples dans la chambre de Wilson, dues à la désintégration d'atomes légers C, N, O, par les rayons  $\gamma$  du bétatron de 100 MV. Ils les ont appelées "flag tracks". Comme la disposition qu'ils leur ont trouvée était isotrope par rapport aux rayons incidents,

il paraît raisonnable d'attribuer les étoiles simples que nous avons observées à d'autres réactions, pouvant être celles de noyaux lourds et de rayonnements plus énergiques.

Une autre raison favorise également l'hypothèse d'un rayonnement de grande énergie incident verticalement. C'est qu'un rayonnement de faible énergie serait plus probablement secondaire et aurait moins de chances d'être dirigé de façon prépondérante soit verticalement, soit dans le plan horizontal. On est ainsi conduit à attribuer les étoiles simples observées de préférence à un rayonnement primaire de grande énergie incident verticalement, causant l'émission d'une seule particule légère d'énergie peu élevée et d'un noyau de recul, à angle droit, et d'autres particules faiblement ionisantes vers le bas.

Cette hypothèse, qui repose sur l'observation de quatre phénomènes seulement, ne peut être considérée comme établie définitivement. Il paraît clair de toute façon que la radiation cosmique observable à haute altitude renferme une proportion non négligeable de ces étoiles simples, tandis que la plupart des auteurs jusqu'ici ont étudié surtout les étoiles ayant au moins deux branches développées.

Baldwin et Klaiber (1), Cameron et Millar (10) et Tracy et Powell (41) ont observé avec des sources de laboratoire des étoiles simples dues à la désintégration d'éléments légers. Morrison (34, 35) a observé des étoiles à une seule branche visible, sous l'effet d'un méson lent de la radiation cosmique, dans les plaques Ilford C2.

#### 4° AUTRES PHÉNOMÈNES

Entre autres phénomènes aperçus, mentionnons un méson commençant au haut d'une feuille d'émulsion et se terminant dans l'émulsion, long de 1380  $\mu$  dans l'émulsion développée, ou de 1250  $\mu$  avant développement, environ 7 MV, reproduit Fig. 12, et une étoile comprenant 2  $\alpha$  et un recul complet, et un proton incomplet, Fig. 11.

### XI. Reproduction des trajectoires, appareil continu de photomicrographie (Fig. 2)

La reproduction photographique des trajectoires pose un problème difficile. Les fabricants offrent d'excellents appareils qui s'installent sur les microscopes; comme le présent auteur l'a fait pour ses publications précédentes, on peut ajuster le microscope puis remplacer l'œil par l'objectif *f.* 2.9 grand ouvert et réglé pour l'infini d'un appareil photographique sur film 35 mm. Powell et ses collaborateurs ont projeté l'image sur un écran, où ils ont placé ensuite un papier sensible pour l'enregistrer. Morrison et Morton (36) placent un film sensible sur une table et y projettent l'image de la trajectoire. Ils découvrent le film par portions successives après avoir réglé chaque fois la mise au point de l'image pour la portion du film qu'ils impressionnent. Divers auteurs britanniques (12) dessinent souvent la trajectoire à la chambre claire sans la photographier et Lord et Schein (30) projettent l'image sur une feuille de



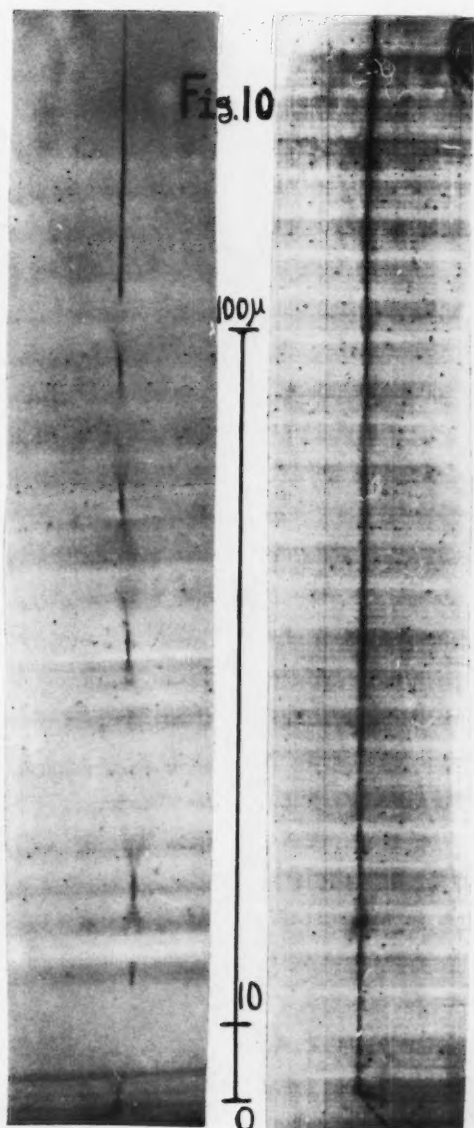


FIG. 10. A gauche, mises au point stationnaires, à droite, mise au point continue à l'aide de l'appareil décrit sur le même rayon  $\alpha$ . Avec une mise au point fixe, l'obliquité empêche de photographier à la fois plus de 3  $\mu$  de longueur de la trajectoire. Quelques rayons  $\delta$  au début du rayon  $\alpha$  à droite.

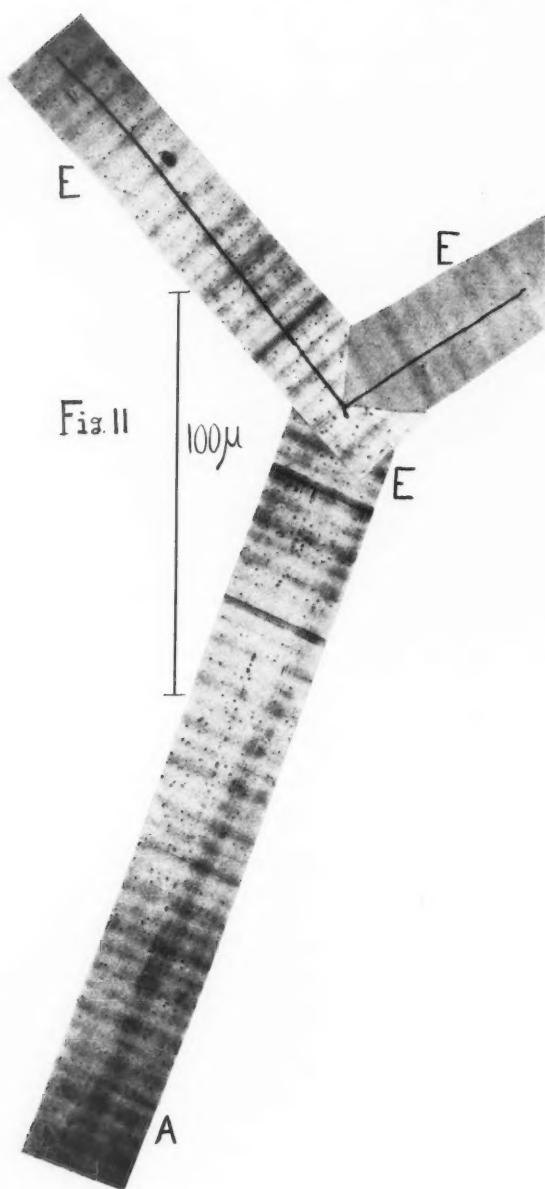


FIG. 11. Etoile  $2\alpha + R$  complets +  $1p$  se terminant en A. Le recul est épaissi et fourchu à la fin ce qui indique une charge élevée.

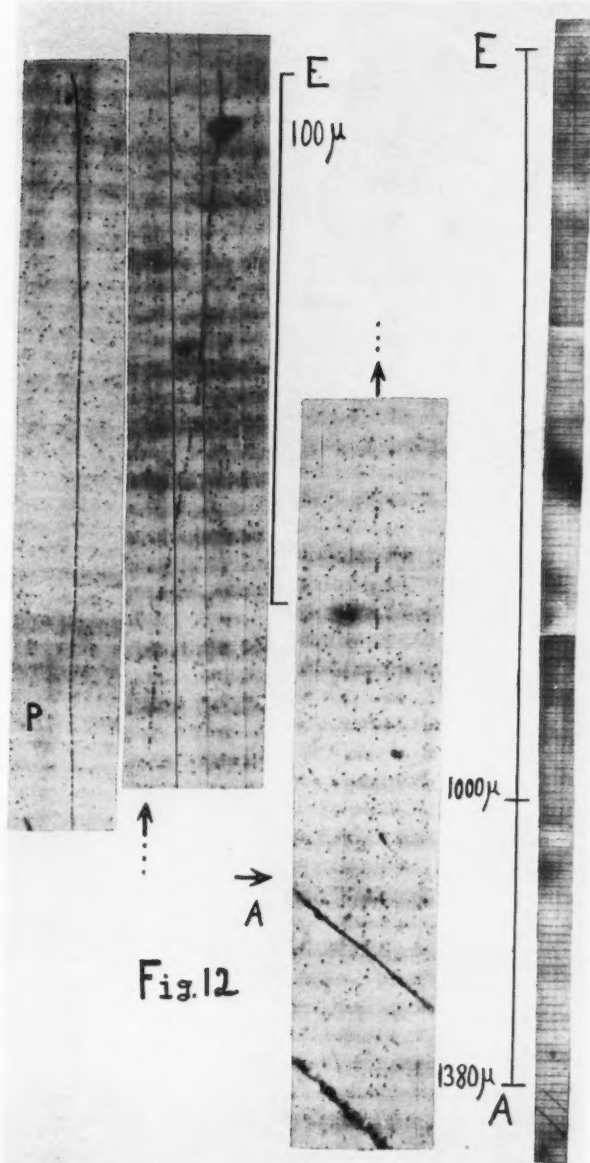


FIG. 12. Trajectoire de méson commençant à l'air et se terminant dans l'émulsion longue de 1375  $\mu$ , environ 6 MV. Un seul négatif continu. A gauche, fin d'un proton.

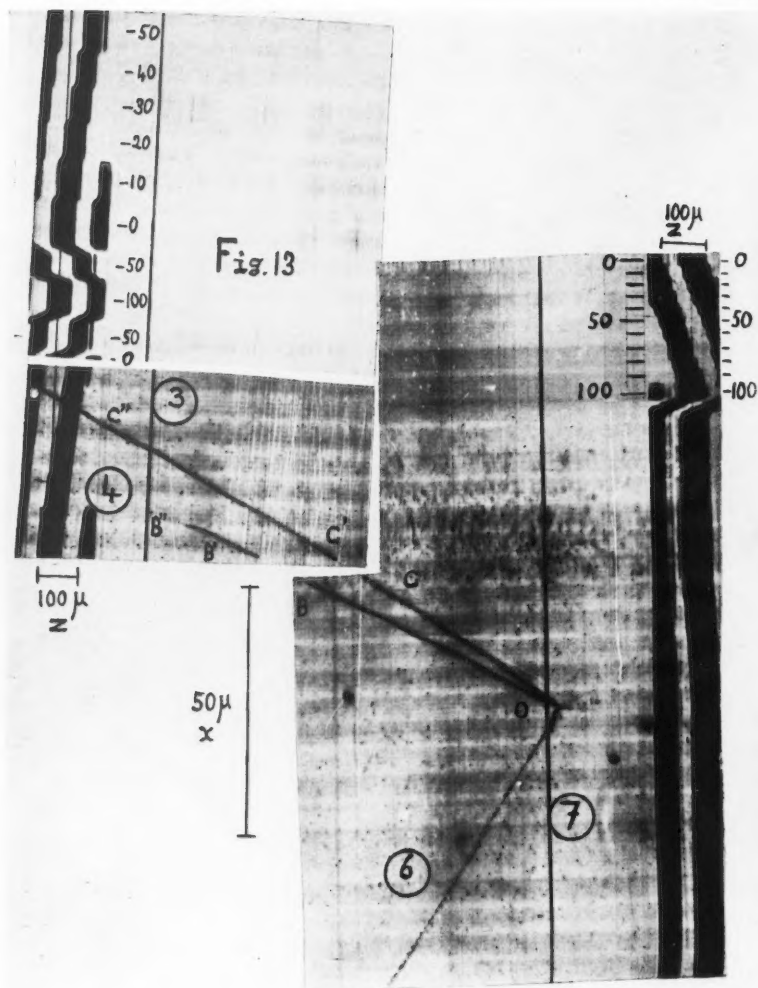


FIG. 13. Parties de l'étoile Fig. 6 photographiées dans les feuilles 4 (centre), et 5, avec inscription de la cote  $Z$  par la projection sur la fente de l'ombre du fil d'une vis tournant avec le réglage fin. L'échelle des  $Z$  est inscrite. On peut apprécier  $Z$  à  $1 \mu$  près. Les deux épreuves sont placées pour aligner les portions de deux trajectoires  $\alpha$ . La portion des trajectoires manquante projetée sur l'axe  $x$  du mouvement du film mesure  $4,8 \mu$ . On en tire que l'épaisseur d'air interposée était  $11,3 \mu$ .

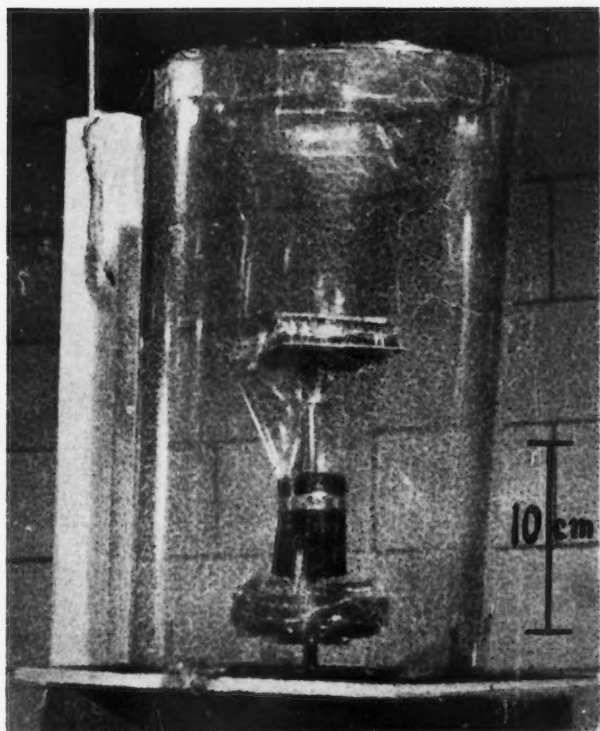
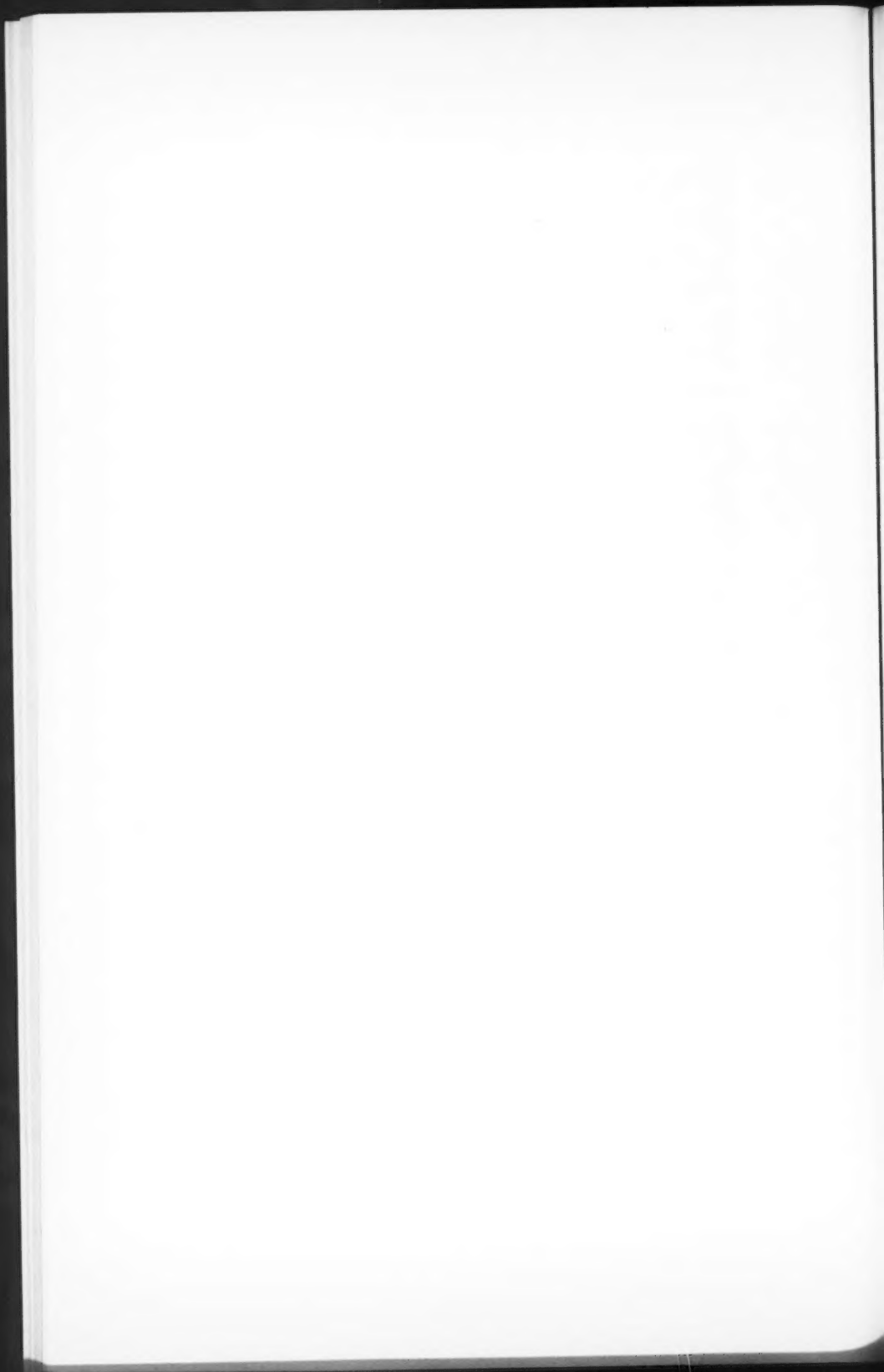


FIG. 14. Boussole pour l'étude de l'anisotropie. On distingue la cloche d'acétate de cellulose, le paquet d'émulsions porté sur le tube de centrifuge à fond conique, les aimants attachés au bas de ce tube, et la tige de laiton qui sert de pivot.



papier et y dessinent chaque grain. Yagoda (47) utilise un procédé intermédiaire entre la photographie et le dessin. De nombreux auteurs reculent sans doute devant la difficulté et ne montrent pas dans leurs publications les trajectoires qu'ils ont étudiées.

La reproduction correcte des trajectoires exige les meilleures conditions de réglage optique du microscope, surtout dans le cas de nos grains qui sont extrêmement fins. A cause de leur obliquité, la plupart des trajectoires ne peuvent être mises au point en une fois sur toute la longueur qu'on en voit à la fois dans un champ. Il faut donc prendre toute une série de négatifs pour un champ donné, avec des mises au point légèrement différentes chaque fois, puis tirer autant d'épreuves positives et assembler après les avoir taillé convenablement, les morceaux des épreuves tirées, pour reconstituer une image nette de toute la trajectoire visible dans le champ. Cet inconvénient est corrigé en partie par une platine inclinable à volonté réalisée par Barbour (3, 4). Enfin les trajectoires longues ne peuvent apparaître toutes entières dans un même champ, de sorte qu'il faut répéter les opérations précédentes pour plusieurs champs contigus. Le champ dans les conditions optiques requises, mesure 100 à 180  $\mu$  de diamètre. Par ailleurs une reproduction photographique d'une trajectoire est souvent nécessaire à l'illustration d'un article scientifique, et nous avons essayé plusieurs dispositifs dans l'espoir de reproduire commodément divers phénomènes et surtout les grandes étoiles.

Le premier dispositif essayé fut celui de Morrison et Morton, qui se montra excellent pour les trajectoires les plus nettes. Cependant il fut impossible de reproduire les trajectoires les plus faibles, parce qu'on ne pouvait les apercevoir sur l'écran pour en faire la mise au point à cause de la finesse des grains, peut-être de l'insuffisance de l'éclairage, et des défauts du miroir argenté de front qu'il faut employer.

Un montage inspiré du précédent fut réalisé mais non essayé, formé d'une fente se déplaçant devant le film sensible. L'image de la trajectoire se formerait sur le film, non pas toute à la fois, mais successivement, à mesure que la fente le découvre. On mettrait au point le microscope manuellement, de façon que l'image de la portion de la trajectoire qui tombe à travers la fente sur le film soit constamment au point. Un système réflex avec une seconde fente semblable à la première dont elle est solidaire dans son déplacement, servirait à observer une image aérienne de la trajectoire. Ce montage permettrait de photographier en une seule opération continue toute la surface du champ visible dans l'oculaire. Il faudrait cependant encore un grand nombre d'opérations et de négatifs distincts pour les trajectoires les plus longues.

Le dispositif finalement réalisé et employé est assez semblable à celui du spectrohélographe qu'on verra décrit dans les traités d'astronomie. Un film de 35 mm. se déroule à une vitesse  $v_2$  derrière une fente qui est fixe, de même que tout le système optique. La plaque sous l'objectif du microscope se déplace à une vitesse uniforme  $v_1$ , son image apparaît projetée sur un écran blanc entourant la fente, elle est agrandie exactement  $n$  fois à la distance où



se trouve le film, de sorte que dans le champ éclairé immobile elle paraît se déplacer à la vitesse  $n v_1$ . L'aspect est assez semblable à celui d'un écran de cinéma sur lequel on montrerait l'image animée d'une rivière prise verticalement à partir d'un avion qui la survolerait. Ici on voit défiler successivement toutes les portions de la trajectoire, si on met au point convenablement.

Si la vitesse du film  $v_2 = n v_1$ , l'image et le film sensible se déplacent ensemble à la même vitesse. Par un système réflex on observe la trajectoire et on ajuste manuellement le microscope pour que la portion de son image qui atteint le film à travers la fente forme constamment une image nette et s'impressionne sur lui. On peut reproduire par ce procédé de façon continue en une seule opération, et sur un même négatif, une trajectoire de longueur quelconque, pourvu qu'elle soit suffisamment rectiligne et bien alignée.

Le mouvement  $v_1$  est obtenu par un moteur synchrone de 2 watts marque Hayden de 1/120 tour par minute, attaquant l'arbre de commande du mouvement des  $x$  sur la platine du microscope Spencer 5 LXX employé. L'excellente qualité des mouvements sur ce microscope assure un déplacement tout à fait régulier et sans à coup. Un tour de cet arbre vaut 6.35 mm. ou sensiblement  $\frac{1}{4}$ " de sorte que l'objet avance à la vitesse  $v_1$  6.35/120 ou 0.0529 mm./min., 52.9  $\mu$ /min. ou 0.881  $\mu$ /sec. Le film est entraîné par un autre moteur synchrone semblable de 1/6 tour par minute, par l'intermédiaire d'une bobine à 16 dents normale, faisant avancer le film de 76.3 mm. par tour. On tire  $v_2 = 12.71$  mm./min., 211.8  $\mu$ /sec. Le grandissement  $n$  doit donc être  $211.8/0.881 = 240$  à la distance où le film se déroule derrière la fente. La fente est réglable en hauteur  $h$ , ce qui permet de régler la durée de pose  $t = h/v_2 = 4.72 h$  si  $h$  est en millimètres et  $t$  en secondes. On a employé  $h = 0.1$  à  $h = 1$  mm. soit des temps de pose variant de  $\frac{1}{2}$  à 5 secondes environ, le film étant à grain très fin et à fort contraste "Microfile" d'Eastman. Il est développé trois minutes dans le révélateur Eastman D 19 dilué 1:1. D'ordinaire on a agrandi le négatif 7.3 fois sur un papier Kodabromide no. 3.

Voici les conditions optiques: lanterne de recherche Bausch et Lomb avec lampe à filament large en ruban de 6 amp. 18 v. alimentée d'ordinaire au minimum du transformateur sur alternatif. Cuve à  $\text{CuSO}_4$ , densité optique environ 0.5. Filtres bleus et neutres ajoutés au besoin pour ajuster l'intensité. Eclairage en lumière parallèle type Köhler, le diaphragme de la lanterne étant grand ouvert pour assurer un éclairage uniforme. Objectif  $\times 90$  d'ouverture 1.3 apochromat, immersion d'huile de part et d'autre de la plaque et oculaire  $\times 12.5$  compensé, tous deux antireflet B & L. La couche antireflet sur l'objectif améliore sensiblement le contraste; sur l'objectif comme sur l'oculaire, elle améliore l'intensité transmise.

Le dispositif réflex a été obtenu en collant une glace polie, à  $45^\circ$  sur le tour de l'oculaire. Avant d'être posée, elle a été dorée sur la face avant par pulvérisation cathodique, elle réfléchit environ 80% et transmet 20% de la lumière. Grâce à la distance frontale considérable de cet oculaire, il est possible d'ob-

server tout le champ à la fois en approchant l'œil, à travers cette glace. L'image est projetée par réflexion sur le film et sur l'écran entourant la fente.

Il est nécessaire de placer un réticule dans le champ de vision pour définir pour l'observateur l'emplacement de la fente, ce réticule projetant son image non à travers la fente mais alentour. Le réticule (Fig. 15) est formé de fils de verre tirés d'un paquet de laine de verre, où ils sont très réguliers et très droits. Ils sont collés à l'aide de ciment à l'acétate de cellulose Duco—C.I.L. sur un anneau collé à son tour dans le tube de l'oculaire. Ce réticule est placé dans le plan conjugué du film, de sorte que si on voit nettement à la fois une portion de trajectoire et le réticule qui l'entoure cette portion de trajectoire forme une image nette sur le film à travers la fente. Pour cela le réticule est monté presque au bas du tube de l'oculaire, à une distance de la lentille supérieure à la distance focale, puisqu'il doit se projeter sur le film qui est loin d'être à l'infini. En plaçant l'œil près de l'oculaire on ne voit donc pas l'image du réticule, qui est virtuelle et se forme à 5-10 cm. au dessus de l'oculaire. L'œil peut observer cette image rejetée à l'infini par une lentille divergente interposée, de distance focale environ—6 cm. Même avec la glace semi-réfléchissante et la lentille négative interposées, la grande distance frontale permet d'observer presque tout le champ tout en portant des lunettes.

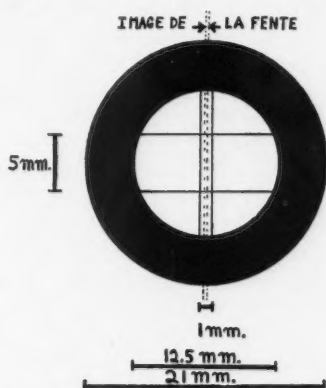


FIG. 15. Réticule formé de fils de verre collés sur un anneau de fer. On l'a fixé dans l'oculaire pour permettre la mise au point dans la photomicrographie continue. La portion du champ définie par les lignes pointillées se projette à travers la fente sur le film. On cherche à n'employer que la région centrale du champ, comprise entre les deux fils distants de 5 mm.

Pour photographier une trajectoire, il faut d'abord l'aligner de façon que son image reste dans la largeur du champ photographique pendant tout son déplacement, et le plus près possible du centre du champ, où l'image est meilleure. Pour pouvoir trouver et déplacer la trajectoire et la plaque qui la porte commodément, on a fait porter par les mouvements normaux  $x$  et  $y$  du microscope, une platine supplémentaire permettant une rotation  $\theta'$ , et portant elle-même deux mouvements rectangulaires tournant avec elle  $x'$  et  $y'$ . La platine

complète réalisée ainsi présente donc, à partir du bas, une rotation  $\theta$  et deux mouvements rectangulaires appartenant au microscope même, puis une rotation  $\theta'$  et deux mouvements rectangulaires  $x'$  et  $y'$  ajoutés. La rotation  $\theta$  ne sert pas. Pour des valeurs particulières de  $x$  et de  $y$ , la rotation  $\theta'$  est centrée sur l'objectif de sorte qu'on peut tourner la plaque sans changer la région visible dans le champ; le ballotement au cours de la rotation ne dépasse pas 10 ou 20  $\mu$ , grâce à la précision de la platine tournante, réalisée dans l'atelier de l'Institut de Physique. En agissant sur les mouvements  $x'$  et  $y'$  qui sont ceux d'une platine dite "Chimique" de Spencer, on peut amener n'importe quel point de la plaque sous l'objectif. On amène le centre de l'étoile à photographier dans le champ, puis on oriente la plaque de manière à aligner successivement chaque trajectoire pour la photographier. Il est parfois possible d'utiliser un seul alignement et une seule pose continue pour reproduire deux trajectoires, si leurs projections horizontales sont sensiblement dans le prolongement l'une de l'autre. Il est de plus parfois possible de former simultanément à travers la fente l'image nette de deux trajectoires à la fois, d'un bout à l'autre de leur longueur. Ce cas se présente si elles ne sont pas trop longues, si elles sont suffisamment voisines, et si elles forment avec la verticale à peu près le même angle l'une et l'autre. (Figs. 4, 6, 7, et 13.)

On ajuste la largeur de la fente pour obtenir la durée de pose convenable, soit entre  $\frac{1}{2}$  sec. et 5 sec. habituellement, selon l'opacité de l'émulsion. On met en marche le film puis le mouvement  $x$  de la plaque, et on observe le champ à travers l'oculaire, en gardant constamment au point la portion de trajectoire au milieu du réticule. La plus longue trajectoire photographiée en une opération jusqu'ici mesurait 1380  $\mu$ , il a fallu  $1380/52.9 = 24.2$  min. pour aller d'un bout à l'autre. On peut interrompre l'opération si on veut en coupant tous les courants, et la reprendre en les rétablissant tous à la fois, sans dommage au négatif résultant: les moteurs et l'éclairage arrêtent et repartent en même temps. On a pu d'autre part photographier en une seule opération et sur un seul négatif très court des trajectoires courtes mais très inclinées, par exemple un proton mesurant 30  $\mu$  de projection horizontale, et 40  $\mu$  de projection verticale, dont la reproduction correcte étant donné la faible profondeur de champ requiert environ 60 à 80 mises au point, quelque soit le procédé employé. Le réglage fin de la mise au point est d'excellente qualité sur le microscope employé, ce qui a beaucoup aidé à la qualité des images obtenues. Il paraît préférable, si on doit choisir, de mettre au point par valeurs croissantes de la hauteur, i.e., de photographier une trajectoire en montant plutôt qu'en descendant.

Voici quelques avantages de cette méthode de photographie continue: une seule opération et un seul négatif pour une trajectoire de longueur et de pente quelconque, pourvu qu'elle soit suffisamment rectiligne; mise au point parfaite de toutes les parties dans des conditions optiques excellentes puisqu'on utilise constamment la région centrale du champ; un alignement exact de tous les grains, qui se trouve obtenu sans raccordement d'épreuves provenant de négatifs distincts; longueur exactement restituée à cause du rapport exact des espaces parcourus aux vitesses  $v_1$  et  $v_2$  (Fig. 17); de petits défauts de synchro-

nisme entre les vitesses du film et de l'image ou un agrandissement légèrement inexact dans la projection, jusqu'à 10 ou même 20%, paraissent agir assez peu sur la qualité de l'image obtenue, grâce à la faible hauteur de la fente; enfin, on n'a pas besoin d'une obscurité complète dans la chambre.

Voici par contre quelques désavantages; les jeux dans la démultiplication du moteur synchrone font qu'il y a un retard pouvant atteindre trois ou quatre minutes au démarrage de la plaque: la trajectoire n'avance pas et le film se dépense sans l'enregistrer. Le temps perdu du mouvement des  $x$  sur la platine est rattrapé facilement et n'est pas responsable de ce retard.—L'entraînement du film n'est pas parfaitement uniforme à cause de la présence de dents sur le rouleau qui frottent sur les encoches du film au moment de se dégager, de sorte qu'on observe des stries transversales résultant de poses alternativement allongées et écourtées. Ces irrégularités ne paraissent pas altérer notablement l'image des grains. Elles affectent cependant l'alignement des grains dans les trajectoires placées très obliquement par rapport au mouvement (Fig. 13). On observe aussi des stries transversales, d'origine analogue, sur les spectro-héliogrammes.\*—Enfin la durée de pose est difficile à régler, quand on passe d'une plaque à une autre plus ou moins opaque. On a essayé un photomètre à extinction formé d'un coin optique, qui a permis de connaître l'intensité du champ à un facteur 2 près, et de régler en conséquence la largeur de la fente nécessaire; mais cette précision est insuffisante. Le film à grain fin et à fort contraste "Microfile" ne possède pas une grande latitude de pose, et on obtient souvent, si on ne développe pas d'abord une bande d'essai, un négatif noir trop long à imprimer sur l'agrandisseur, ou trop pâle et donnant une épreuve faible et sans détail même avec un papier à fort contraste. On a remédié à cet inconvénient par un photomètre à comparaison: une source de lumière formée d'une petite lampe de microscope de 15 watts sert d'étalon, on se sert de la face supérieure du miroir à 45° surmontant l'oculaire pour comparer la source étalon vue par réflexion et le champ du microscope vu par transparence.

Une exigence de la méthode sinon un désavantage est la nécessité de suivre sans arrêt pendant toute l'opération le déplacement de la trajectoire et d'ajuster la mise au point constamment. On pourrait songer à construire un appareil photoélectrique qui assurerait automatiquement la mise au point, mais cette entreprise paraît peu intéressante; pour les trajectoires les plus faibles, elle serait probablement inutile.

Pour les trajectoires courtes l'opération se fait rapidement et n'exige pas un grand effort, et tout autre procédé équivalent serait plus compliqué. Pour une trajectoire très longue, la durée de l'opération pourrait être réduite par l'emploi de vitesses  $v_1$  et  $v_2$  plus grandes, avec une fente un peu plus large pour assurer un temps de pose suffisant puisque l'intensité lumineuse est limitée. Une fente étroite est nécessaire pour une trajectoire très oblique qui n'est jamais au point sur une grande longueur à la fois, d'où la nécessité des faibles vitesses adoptées. Mais une trajectoire longue est habituellement sensible-

\*De petites irrégularités des déplacements du film et de l'objet se manifestent quand on compare de près deux négatifs de la même trajectoire (Figs. 7b et 17).

ment horizontale, de sorte qu'on pourrait employer par exemple une fente six fois plus haute et des vitesses six fois plus grandes, permettant par exemple la photographie d'une trajectoire de  $1200\ \mu$  en 3.77 au lieu de 22.62 min. A de telles vitesses le champ de  $180\ \mu$  environ est traversé en 0.565 au lieu de 3.40 min., de sorte que l'observateur doit exécuter plus rapidement les réglages nécessaires, s'il est vrai que l'opération est moins longue.

Il subsiste un inconvénient inhérent non à la méthode employée, mais aux reproductions photographiques mêmes. Les trajectoires très longues, surtout celles observées dans nos émulsions où le grain est très fin, sont difficiles à reproduire à l'échelle de façon satisfaisante par les procédés courants de l'imprimerie, sur la surface des pages normales des revues scientifiques. Le problème est le même que celui de la reproduction à l'échelle sur la carte géographique du Canada ou même seulement de la province de Québec, d'une route avec sa largeur vraie (Fig. 5).

De toute façon le procédé a permis d'obtenir des photographies de trajectoires et d'étoiles d'excellente qualité, avec une facilité grandement accrue par rapport aux anciens procédés. Quelques unes de ces trajectoires et de ces étoiles sont reproduites dans le présent article (Figs. 10, 15, 16 et 17, etc.).

Nous avons pu inscrire la cote des points successifs sur la trajectoire à mesure qu'ils sont photographiés, par le dispositif suivant. Un selsyn tourne avec le réglage fin grâce à un embrayage formé d'un disque de caoutchouc mousse épais de 5 mm. évitant de transmettre les vibrations. Un second selsyn répète les mouvements du précédent et fait tourner dans l'air une vis sans fin de pas 48 au pouce ou environ 1.6 mm. La lumière venue du microscope projette sur la fente l'ombre légèrement agrandie du fil de la vis qui avance d'un pas soit environ 2 mm. pour un tour du réglage fin soit  $100\ \mu$  de hauteur. On trace ainsi continûment sur le film grâce à cette ombre, la courbe de la hauteur en fonction de la position sur la trajectoire. Cette ombre se projette sur le bord du film pour laisser libre la région centrale où apparaît l'image des trajectoires.

L'étalonnage de ce système se fait en ajustant le tambour du réglage fin des  $z$  à des valeurs successives convenables de la cote, v.g., 0, 10, 20, . . .  $100\ \mu$ , pendant que le film se déroule. La vis tourne et prend des positions successives qui dessinent sur le film une ombre en gradins valant chacun, v.g.,  $10\ \mu$ . Les mêmes ombres se répètent à tous les tours du réglage fin soit à tous les  $100\ \mu$ . Ce procédé est illustré par la Fig. 13 et son emploi a permis d'obtenir les résultats du paragraphe suivant.

## XII. Calcul de l'épaisseur d'air interposé

Ce calcul est possible dans le cas particulier de deux rayons  $\alpha$  Nos. 3 et 4 ayant une origine commune 0 dans la feuille No. 4, interrompus au bas de cette feuille et retrouvés dans la feuille No. 5. Ils sont reproduits en partie dans la Fig. 13. Les épreuves agrandies à la même échelle sont placées pour que les portions de chaque trajectoire soient dans le prolongement l'une de l'autre. En l'absence de causes de déformation et d'erreur, cette disposition est unique-

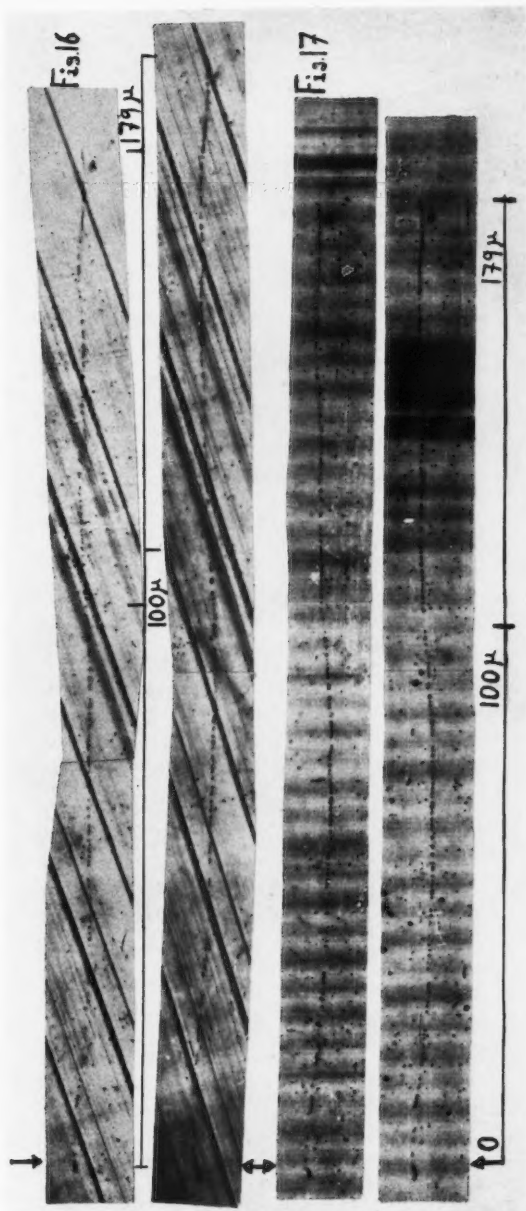
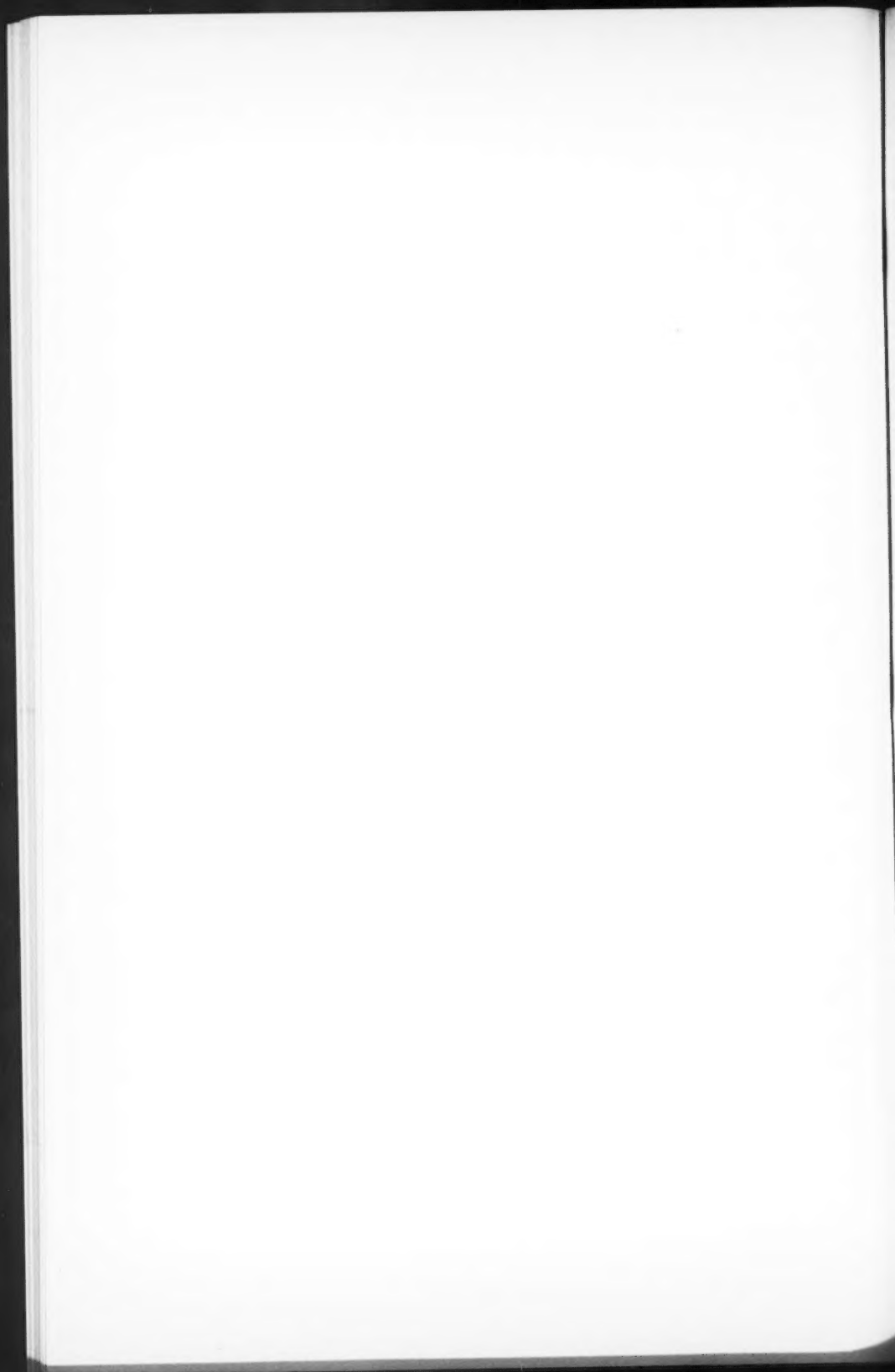


Fig. 16. Étoile simple (R - mésion) enregistrée complètement dans l'émulsion. La désintégration a eu lieu au point désigné par une flèche. Les stries sont dues aux projections sur la fente des traits transversaux et des défauts d'un réticule à mailles carrées gravées sur verre qui a servi dans le premier montage de photomicrographie continue réalisé, au lieu du réticule à fils employé finalement (Fig. 15). Ce montage n'utilisait qu'un moteur synchrone qui actionnait directement le film et indirectement le mouvement des  $\pi$  grâce à une transmission et à une démultiplication 1/20. Il ne comportait pas la platine tournante  $\Phi$ , d'où l'inclinaison sur l'axe du mouvement  $\pi$  marqué par les stries, de la trajectoire qu'on n'a pu orienter avant de la photographier. Les négatifs des Figs. 16 et 17 sont également agrandis.

Fig. 17. Même étoile simple (R - mésion) que Fig. 16. Un phénomène, deux négatifs obtenus par le procédé décrit dans le texte. La reproduction est plus régulière qu'avec le montage de la Fig. 16. Ce phénomène représente probablement la création d'un mésion, la particule incidente devait donc avoir une énergie cinétique de l'ordre d'au moins 100 MeV.





ment déterminée, et la distance dans le plan de la figure, entre les extrémités des portions de trajectoires se faisant face, représente la projection du parcours dans l'air interposé. Appelons OB, OC les segments de trajectoires assimilés à des droites, dans la feuille 4, et B'B'', C'C'', leur suite dans la feuille 5. Les distances franchies dans l'intervalle d'air sont BB', CC'. La projection de ces distances selon la direction du mouvement du film a une valeur commune soit  $\Delta x$ .

Les points OBC, B'B'' C'C'' définissent des plans possédant des pentes calculables sur la figure d'après l'échelle de la reproduction pour  $x$ , et d'après l'ombre du fil de la vis pour  $z$ . La pente ainsi mesurée vaut  $19 \mu / 26 \mu = 0.73$  pour la feuille 4, et  $38 \mu / 32 \mu = 1.19$  pour la feuille 5, en moyenne pente observée = 0.96. Pour  $\Delta x = 4.8 \mu$  on tirerait  $\Delta z = 4.6 \mu$  épaisseur d'air interposé. En réalité, il faut tenir compte de la déformation des feuilles, qui allonge de 10% les dimensions  $x$ , et contracte à 41.3% les dimensions  $z$ , c'est-à-dire  $\Delta x_o = \Delta x \text{ obs.} / 1.1$ ;  $\Delta z_o = \Delta z \text{ obs.} \cdot 1.21 / 0.5$ . D'où on tire: Pente orig. = Pente obs.  $\times 2.66$ ;  $\Delta x$  observé ici devient  $4.4 \mu$ ; Pente orig. =  $2.66 \times 0.96 = 2.56$ ,  $\Delta z_o = 4.4 \mu \cdot 2.56 = 11.3 \mu$ .

L'épaisseur d'air interposé au moment de l'irradiation était  $11.3 \mu$  avec une précision estimée de  $5 \mu$ . Parmi les causes d'erreur, mentionnons la distorsion de l'émulsion, la courbure du champ et les irrégularités d'entraînement du film et de la plaque.

### XIII. Étude en cours sur l'anisotropie des rayons cosmiques

Winckler, Dwight, Sabin et Stix (23, 40, 44) ont entrepris récemment une étude approfondie de l'anisotropie des rayons cosmiques à l'aide de télescopes à compteurs G.M. portés par des ballons sondes, l'azimut du télescope étant transmis par radio-sonde, grâce à une boussole portée par la nacelle.

Il paraît attrayant de tenter une étude de ce genre à l'aide d'un empilement de feuilles d'émulsions orienté pendant l'ascension grâce à une boussole. On connaîtrait ainsi la direction dans l'espace au moment de son enregistrement, de chaque trajectoire visible dans l'émulsion. Le montage expérimental a été réalisé et a flotté à haute altitude le 30 août 1949. Malheureusement la nacelle n'a pas été retrouvée mais on se propose de reprendre l'expérience prochainement.

Depuis ces essais l'auteur a appris que Morand, Beets et Winand à Liège, ont déjà réalisé (6, 31, 32, 33) une expérience analogue, avec des plaques sensibles aux électrons placées dans le plan vertical est-ouest sur des montagnes du Congo belge, près de l'équateur géomagnétique. Dans ces conditions ils ont trouvé une différence marquée, le rayonnement astérogène venant surtout de l'ouest. Il faut s'attendre à des effets en azimut encore plus marqués à grande altitude, qui devraient être encore perceptibles même à la latitude relativement élevée de Montréal. L'effet azimutal devrait naturellement disparaître au pôle. Notre montage permet en principe une étude plus approfondie que celui des auteurs belges.

Le montage que nous avons employé est le suivant. Un tube de centrifuge de 200 cm<sup>3</sup>. en verre à fond conique est enfilé à l'envers sur une tige en laiton verticale appointie au sommet. Autour de l'ouverture du tube, sont collés environ 200 g. d'aimants Alnico II, dont on oriente parallèlement tous les dipôles magnétiques. Le système forme une boussole qui peut balloter d'environ 6° autour de la verticale et qui oscille autour du méridien magnétique avec une période de quelques secondes, le couple de restitution étant relativement grand. Par dessus le fond du tube renversé on installe le paquet de feuilles d'émulsion empilées, serré entre deux lames minces de duralumin, à l'aide d'un tube d'aluminium qui coiffe le tube de verre, de ciment C.I.L.-Duco et de ruban Durex. Le centre de gravité est très au dessous du pivot, et le tout est équilibré avec soin. L'appareil est porté par une nacelle et entouré d'une boîte transparente en acétate de cellulose et de cellophane qui évitent le vent et qui gardent la chaleur solaire absorbée à l'intérieur, il est représenté sans le cellophane dans la Fig. 14.

La nacelle porte un balancier horizontal en bois léger long de 4 m., pourvu à chaque extrémité d'une queue en papier couvert d'aluminium et enduit d'un vernis rouge pour attirer l'attention et faciliter la récupération. L'ensemble de la nacelle est soigneusement équilibré avant le départ. Le balancier stabilise la nacelle comme on a pu le constater en observant à la lunette le ballon-sonde, qui est resté visible pendant deux heures et demie.

Dans les prochaines ascensions, on compte employer un aimant alnico en forme d'anneau aimanté selon un diamètre, de façon à avoir le plus fort couple magnétique possible compatible avec un moment d'inertie déterminé et un pivot d'acier sur agate pour supporter la boussole.

Un appareil différent destiné au même usage vient d'être décrit par Ney, Linsley et Freier (37).<sup>\*</sup> Ils utilisent une boussole légère qui par un mécanisme photoélectrique agit sur un servo-moteur pour garder les plaques alignées par rapport au méridien magnétique. Un dispositif analogue avec servo-moteur est en cours de réalisation au laboratoire de Brookhaven (39). Ces appareils permettent peut-être d'orienter une charge plus élevée de plaques sensibles, mais le nôtre a l'avantage de ne pas exiger de circuits électriques délicats; de plus il évite toute masse matérielle importante à proximité des émulsions sensibles, ce qui simplifie l'interprétation des résultats obtenus.

### Remerciements

L'auteur remercie M. Mario Iona Jr., M. E. H. Krause, M. Adair Morrison et la Cie BOAC grâce à qui les premières irradiations à haute altitude ont pu être faites; M. Roger Mathieu qui a fait les plans de la platine tournante, et M. Edmond Gosselin, technicien à l'Institut de Physique de l'Université de Montréal, qui les a exécutés; plusieurs personnes trop nombreuses pour qu'il soit possible de toutes les mentionner, qui ont apporté leur concours au moment des lancements de ballons; et enfin le Conseil National des Recherches, pour un octroi qui a contribué à rendre ce travail possible.

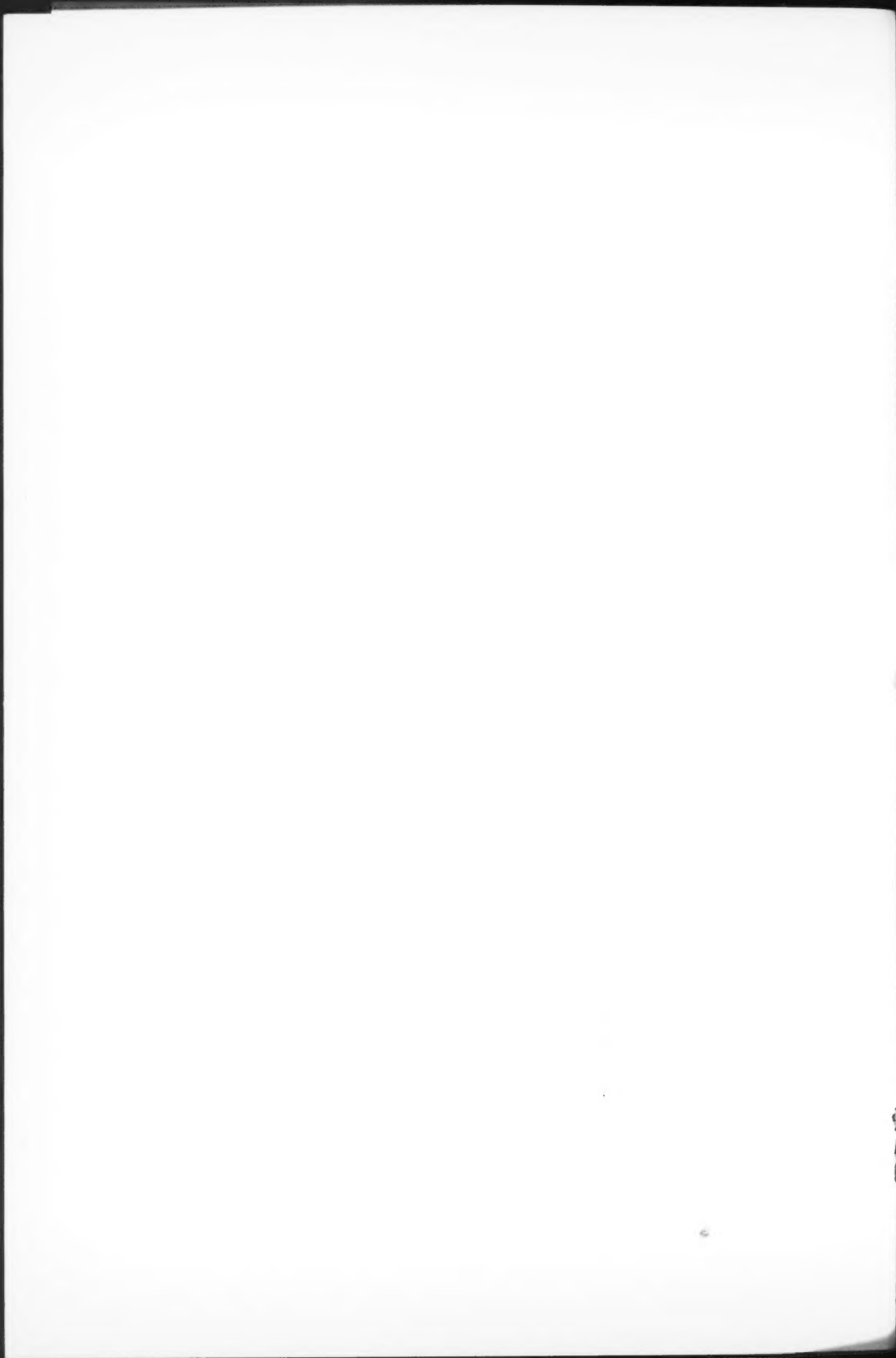
<sup>\*</sup>Notes aussi Freier, P. S., Ney, E. P., Naugle, J., et Anderson, G. *Phys. Rev.* 79:206. 1950.

## Références

1. BALDWIN, G. C. ET KLAIBER, G. S. Phys. Rev. 70: 259. 1946.
2. BARBOUR, I. Phys. Rev. 74: 507. 1948.
3. BARBOUR, I. Phys. Rev. 76: 320. 1949.
4. BARBOUR, I. Rev. Sci. Instruments, 20: 530. 1949.
5. BARBOUR, I. Communication privée.
6. BEETS, C., MORAND, M., ET WINAND, L. Bull. soc. roy. sci. Liège, Sér. no. 12: 481. 1949.
7. BLAU, M. ET WAMBACHER, H. Sitzber. Akad. Wien, Abt. IIa, 146: 259. 1937.
8. BLAU, M. ET WAMBACHER, H. Sitzber. Akad. Wien, Abt. IIa, 146: 469. 1937.
9. BLAU, M. ET WAMBACHER, H. Sitzber. Akad. Wien, Abt. IIa, 146: 623. 1937.
10. CAMERON, A. G. W. ET MILLAR, C. H. Phys. Rev. 78: 337. 1950.
11. CHAMPION, F. C. ET POWELL, C. F. Proc. Roy. Soc. London, A, 183: 64. 1944.
12. COATES, A. C. ET HERZ, R. H. Phil. Mag. 40: 1088. 1949.
13. DEMERS, P. Phys. Rev. 70: 86. 1946.
14. DEMERS, P. Phys. Rev. 70: 974. 1946.
15. DEMERS, P. Can. J. Research, A, 25: 223. 1947.
16. DEMERS, P. Phys. Rev. 71: 483. 1947.
17. DEMERS, P. Ann. Acfas, 14: 63. 1948.
18. DEMERS, P. Ann. Acfas, 15: 48. 1949.
19. DEMERS, P. Phys. Rev. 78: 320. 1950.
20. DEMERS, P. Science, 110: 380. 1949.
21. DEMERS, P. Ann. Acfas, 16: 74. 1950.
22. DEMERS, P. ET FICHAUD, R. Ann. Acfas, 15: 53. 1949.
23. DWIGHT, K., SABIN, R., STIX, T., ET WINCKLER, J. Phys. Rev. 78: 324. 1950.
24. FICHAUD, R. Thèse de maîtrise. Univ. de Montréal. 1949.
25. FOWLER, P. H. Phil. Mag. 42: 169. 1950.
26. FRANZINETTI, C. Phil. Mag. 41: 86. 1950.
27. FREIER, P., LOFGREN, E. J., NEY, O. P., OPPENHEIMER, F., BRADT, H. L., ET PETERS, B. Phys. Rev. 74: 213. 1948.
28. LAPALME, J. Thèse de maîtrise, Univ. de Montréal. 1948.
29. LAPALME, J. ET DEMERS, P. Phys. Rev. 72: 535. 1947.
30. LORD, J. J. ET SCHEIN, M. Phys. Rev. 77: 19. 1950.
31. MORAND, M. Compt. rend. 228: 1488. 1949.
32. MORAND, M. Compt. rend. 229: 40. 1950.
33. MORAND, M., WINAND, L., ET BEETS, C. Bull. soc. roy. sci. Liège, Sér. no. 4 et 5: 134. 1949.
34. MORRISON, A. Communication privée.
35. MORRISON, A. Thèse de doctorat, McGill University. 1948.
36. MORRISON, A. ET MORTON, F. Rev. Sci. Instruments. 20: 341. 1949.
37. NEY, E. P., LINSLEY, J., ET FREIER, P. S. Phys. Rev. 79: 206. 1950.
38. POWELL, C. F. ET OCCHIALINI, G. P. S. Phys. Soc. Cambridge Conf. Repts. 150. 1947. Cambridge: The University Press.
39. SALANT, E. O. ET HORNBOSTEL, J. Communication privée.
40. STIX, T., DWIGHT, K., SABIN, R., ET WINCKLER, J. Phys. Rev. 78: 324. 1950.
41. TRACY, J. ET POWELL, W. M. Phys. Rev. 77: 594. 1950.
42. WEBB, J. H. Phys. Rev. 74: 511. 1948.
43. WILKINS, T. R. Natl. Geog. Soc. Stratosphere Series, 2: 37. 1936.
44. WINCKLER, J., DWIGHT, K., SABIN, R., ET STIX, T. Phys. Rev. 78: 324. 1950.
45. YAGODA, H. Nucleonics, 2(5): 2. 1948.
46. YAGODA, H. Radioactive measurements with nuclear emulsions. John Wiley & Sons, Inc., New York. 1949.
47. YAGODA, H. Communication privée.
48. YAGODA, H. Phys. Rev. 79: 207. 1950.







## CANADIAN JOURNAL OF RESEARCH

### Notes on the Preparation of Copy

**GENERAL:**—Manuscripts should be typewritten, double spaced, and the **original and one extra copy** submitted. Style, arrangement, spelling, and abbreviations should conform to the usage of this Journal. Names of all simple compounds, rather than their formulae, should be used in the text. Greek letters or unusual signs should be written plainly or explained by marginal notes. Superscripts and subscripts must be legible and carefully placed. Manuscripts should be carefully checked before being submitted, to reduce the need for changes after the type has been set. If authors require changes to be made after the type is set, they will be charged for changes that are considered to be excessive. **All pages, whether text, figures, or tables, should be numbered.**

**ABSTRACT:**—An abstract of not more than about 200 words, indicating the scope of the work and the principal findings, is required.

#### ILLUSTRATIONS:

(i) **Line Drawings:**—All lines should be of sufficient thickness to reproduce well. Drawings should be carefully made with India ink on white drawing paper, blue tracing linen, or co-ordinate paper **ruled in blue only**; any co-ordinate lines that are to appear in the reproduction should be ruled in black ink. Paper ruled in **green, yellow, or red should not be used** unless it is desired to have all the co-ordinate lines show. Lettering and numerals should be neatly done in India ink preferably with a stencil (**do not use typewriting**) and be of such size that they will be legible and not less than one millimeter in height when reproduced in a cut three inches wide. All experimental points should be carefully drawn with instruments. Illustrations need not be more than two or three times the size of the desired reproduction, but the ratio of height to width should conform with that of the type page. **The original drawings and one set of small but clear photographic copies are to be submitted.**

(ii) **Photographs:**—Prints should be made on glossy paper, with strong contrasts; they should be trimmed to remove all extraneous material so that essential features only are shown. Photographs should be submitted **in duplicate**; if they are to be reproduced in groups, one set should be so arranged and mounted on cardboard with rubber cement; the duplicate set should be unmounted.

(iii) **General:**—**The author's name, title of paper, and figure number should be written in the lower left hand corner (outside the illustration proper) of the sheets on which the illustrations appear.** Captions should not be written on the illustrations, but typed on a separate page of the manuscript. All figures (including each figure of the plates) should be numbered consecutively from 1 up (arabic numerals). **Each figure should be referred to in the text.** If authors desire to alter a cut, they will be charged for the new cut.

**TABLES:**—Titles should be given for all tables, which should be numbered in Roman numerals. Column heads should be brief and textual matter in tables confined to a minimum. **Each table should be referred to in the text.**

**REFERENCES:**—**These should be listed alphabetically by authors' names, numbered in that order, and placed at the end of the paper.** The form of literature citation should be that used in the respective sections of this Journal. **Titles of papers should not be given in references listed in Sections A, B, E, and F, but must be given in references listed in Sections C and D.** The first page only of the references cited in papers appearing in Sections A, B, and E should be given. **All citations should be checked with the original articles.** Each citation should be referred to in the text by means of the key number; in Sections C and D the author's name and the date of publication may be included with the key number if desired.

### Reprints

Fifty reprints of each paper without covers are supplied free. Additional reprints, if required, will be supplied according to a prescribed schedule of charges. On request, covers can be furnished at cost.





